Sensory convergence and inhibitory divergence: deep dorsal horn inhibitory interneurons modulate the timing and magnitude of limb coordination during locomotion.

Authors

Nofar Ozeri-Engelhard*[1,2,3,6], Mark A Gradwell*[1,2,6], Olivier D Laflamme[4,5], Aman Upadhyay[1,2,3], Adin Aoki[1,2], Tara Shrier[1,2], Melissa Gandhi[1,2], Melissa Gonzalez[2], Jaclyn T Eisdorfer[1,2], Gloria Abbas- Zadeh[1,2], Nusrath Yusuf[1,2,3], Zarghona Imtiaz[1,2], Simona A Alomary[1,22], Jordan Katz[1,2], Michael Haas[1,2], Yurdiana Hernandez[2], Turgay Akay[5], Victoria Abraira[1,2,7]

* These authors have contributed equally

[1]Cell Biology and Neuroscience Department, Rutgers University, The State University of New Jersey, New Brunswick, United States of America
[2]W.M. Keck Center for Collaborative Neuroscience, Rutgers University, The State University of New Jersey, New Brunswick, United States of America
[3]Neuroscience PhD program at Rutgers Robert Wood Johnson Medical School, Piscataway, New Jersey, United States of America
[4]Dalhousie PhD Program
[5]Dalhousie University, Dept. of Medical Neuroscience, Atlantic Mobility Action Project, Brain Repair Center, Halifax, NS, Canada
[6]equal contribution
[7]lead contact
Link to authors, affiliations and potential reviewers

Correspondence

victoria.abraira@rutgers.edu (V.E.A)

Highlights

- Inhibitory interneurons in the medial deep dorsal horn (mDDH), functionally represented by a large glycinergic PV expressing subpopulation (dPVs), receive convergent input from cutaneous receptors and proprioceptors and are preferentially recruited during locomotion.

- While dPVs diffusely target motor networks, the temporal dynamics of their activity is regulated by incoming inputs, suggesting a role in modulation of motor output timing.

- Ablation of dPVs alters stance-to-swing transition and step frequency during high-speed locomotion, likely to result from loss of sensory mediated muscle inhibition.

- Ablation of dPVs alters joint kinematics at the transition from stance-to-swing, likely to result from loss of sensory mediated muscle amplitude attenuation.

SUMMARY (~1000 characters) @1400

To achieve smooth motor performance in a rich and changing sensory environment, motor outputs must be constantly updated in response to sensory feedback. Although proprioception and cutaneous information are known to modulate motor output, it is unclear whether they work together in the spinal cord to shape complex

motor actions such as locomotion. Here we identify the medial deep dorsal horn as a “hot zone” of convergent proprioceptive and cutaneous input for locomotion. Due to increased responsiveness to sensory input, inhibitory interneurons in the medial deep dorsal horn area are preferentially recruited in locomotion. To study inhibitory interneurons in this area, we utilize an intersectional genetic strategy to isolate and ablate a population of parvalbumin-expressing glycinergic interneurons in the medial deep dorsal horn (dPVs). Using histological and electrophysiological methods we find that dPVs integrate convergent proprioceptive and cutaneous input while targeting diffuse ventral horn motor networks. dPV ablation paired with behavioral testing and EMG recordings reveals a role for dPVs in the timing and magnitude of muscle recruitment, controlling step-cycle transition, kinematics, and limb coordination in a state and phase-dependent manner. Together, our results suggest that convergent sensory inputs work in concert to coordinate the activity of dPVs, and in-turn regulate motor output in a contextually relevant manner.

INTRODUCTION (~4000 characters) @ 5090

The ability to locomote is fundamental to almost every living creature, making it one of the most robust motor behaviors across the animal kingdom. Whether by searching for food, escaping a predator, or migrating due to climate change, animals use locomotion for survival. It is thus not surprising that the study of locomotion can be dated back to Aristotle, among other philosophers and Greek physicians during the 3rd century (*Aristotle’s De Motu Animalium* 1986). However, it was the experiments performed by Charles Sherrington and Graham Brown during the 20th century that shaped our current views about the circuits involved in locomotion. Sherrington proposed that locomotion is organized as a “chain” of reflexes, requiring the participation of sensory feedback (Charles Scott Sherrington 1906). However, Brown’s pioneering experiments, recording fictive locomotion in decerebrated and deafferented cats, demonstrated that locomotion persists in the absence of sensory feedback (T. G. Brown and Sherrington 1911). These studies led to the dogma most accepted today of “Central Pattern Generator” (CPGs), intrinsic spinal networks generating the rhythmic and alternating activity controlling locomotion. Although not required for its generation, sensory input plays an important role in locomotion. In humans, permanent loss of large sensory fibers leads to a complete inability to walk, which is only regained following long training and visual guidance (Lajoie et al. 1996; Tuthill and Azim 2018).

Two main sensory inputs “disturb” the rhythmic pattern of locomotion. The first is proprioception, the sense of one’s own body position detected by receptors embedded in muscles, joints, and tendons. The second is cutaneous input, relaying information about skin distortion and detected by low threshold mechanoreceptors (LTMRs). Studies show that both proprioceptive and cutaneous afferents can initiate, arrest, reset, and enhance locomotion (C. Sherrington 1910; Grillner and Rossignol 1978; J and Kg 1980). Further, corrective reflexes, such as the stumbling reflex, rely upon cutaneous and proprioceptive input to appropriately adjust motor output (Forssberg 1979; William Paganini Mayer and Akay 2018). Similar experiments in conjunction with modeling studies conclude that the main role of proprioceptive and cutaneous input is in tuning locomotion to kinematic requirements and environmental changes (Schillings, Van Wezel, and Duysens 1996; Forssberg, Grillner, and Rossignol 1975; Prochazka and Yakovenko 2007).

For efficient modulation of locomotion, information from both proprioceptors and cutaneous receptors must be integrated and processed by motor networks. Previous work highlights the medial part of the deep dorsal horn in processing convergent proprioceptive and cutaneous inputs (Moschovakis, Solodkin, and Burke 1992; A. G. Brown et al. 1981; Edgley and Jankowska 1987a; Ishizuka et al. 1979) and in harboring a large population of premotor interneurons (Levine et al. 2014). Together, these studies suggest that INs located in this area perform multimodal sensorimotor integration for modulation of motor actions, such as locomotion.

Over the last decade, striking progress in the development of mouse genetic tools enabled precise access to spinal cord interneuron populations defined by their common gene expression (Abraira et al. 2017; Gatto et al. 2021; Hilde et al. 2016, 2; Koch et al. 2017; Koch 2019). Using these tools, both excitatory and inhibitory deep dorsal horn interneurons were found to perform multimodal sensorimotor processing. For example, the excitatory dl3 pre-motor interneurons integrate proprioceptive and LTMR input to control grasping (Bui et al. 2013). Inhibitory interneurons expressing the satb2 transcription factor integrate proprioceptive and nociceptive input to regulate the nociceptive withdrawal reflex (Hilde et al. 2016). Inhibitory interneurons that transiently express RorB mainly integrate proprioceptive input and modulate locomotion in a phase-dependent manner by exerting presynaptic inhibition on proprioceptive afferents (Koch et al. 2017).

While studies showed a role for individual deep dorsal horn interneurons, a more holistic understanding of the role of this region in sensorimotor control is still lacking. Here we corroborate that the highest convergence of proprioceptive and cutaneous input in the mouse is localized to the medial portion of lamina IV-V of the spinal cord (i.e., deep dorsal horn). We find that, due to their increased responsiveness to sensory input, inhibitory interneurons are preferentially recruited during locomotion. We next identify a new and uncharacterized inhibitory interneuron population localized to the medial deep dorsal horn that expresses the calcium binding protein parvalbumin (dPVs). We show that dPVs integrate cutaneous and proprioceptive sensory input and relay it to spinal cord motor networks via a diffuse inhibitory network to form a sensorimotor circuit. Utilizing intersectional genetics we show that dPVs modulate the amplitude and timing of muscle activity, to adjust limb coordination in a state and phase dependent manner. In sum, our study reveals a new model by which sensory convergence produces a surprisingly divergent influence on motor networks, thereby increasing the diversity of mechanisms by which sensory input can shape movement.

RESULTS

The medial deep dorsal horn is defined by convergent proprioceptive and cutaneous input

While many studies have examined the contribution of touch and proprioception to normal locomotion, it remains unknown whether this information is integrated within a common pathway or transmitted through distinct circuits to modulate motor output. To begin to answer this question, we aimed to locate the region of the spinal cord most likely to receive convergent proprioceptive and cutaneous input.

Integration of proprioceptive and cutaneous information is essential to normal locomotion and motor adaptation. To identify spinal regions that process convergent proprioceptive and cutaneous inputs, we first visualized the terminal endings of these populations using *PV*^{2aCreER};*Advillin*^{FlpO};*R26*$^{LSL\text{-}FSF\text{-}TdTomato\ (Ai65)}$; *R26*$^{FSF\text{-}SynGFP}$ mice (**Figure 1A**). We found that cutaneous inputs (green) are concentrated in the superficial and deep dorsal horn (Lamina I-IV), while proprioceptive inputs (yellow) span the deep dorsal and ventral horns (Lamina V-X). Of particular interest, convergent sensory input (green + yellow) was largely restricted to the medial deep dorsal horn (LIVmedial- LVmedial) (**Figure 1B-C**). The medial position of this region suggested integration of inputs from the distal limb (ref), which are essential to adjust normal locomotion (Duysens 1977; Schomburg et al. 1998a). To address this, we injected the anterograde tracer CTb into the ventral paw and found that paw innervating primary sensory afferents concentrated in the medial portion of the dorsal horn (**Figure 1D**). Together, these findings suggest that the medial deep dorsal horn (mDDH) plays an important role in integrating convergent proprioceptive and cutaneous sensory inputs from the paw to modulate normal locomotion. Multimodal sensory information from the paw is essential to normal locomotion and motor adaptation (Duysens 1977; Schomburg et al. 1998a). Therefore, we first injected the paw with the retrograde tracer CTB and found paw innervating primary sensory afferents concentrated to the medial portion of the dorsal horn (**Figure 1A**). To determine whether this region receives convergent proprioceptive and cutaneous

inputs, we visualized the terminal endings of these populations using *PV*^{2aCreER};*Advillin*^{FlpO};*R26*$^{LSL\text{-}FSF\text{-}TdTomato\ (Ai65)}$; *R26*$^{FSF\text{-}SynGFP}$ mice (**Figure 1B-C**). We found that cutaneous inputs (green) are concentrated in the superficial and deep dorsal horn (Lamina I-IV), while proprioceptive inputs (yellow) span the deep dorsal and ventral horns (Lamina V-X). Of particular interest, convergent sensory input (green + yellow) was largely restricted to the medial deep dorsal horn (Lamina V) (**Figure 1C-D**). This finding suggests that the medial deep dorsal horn plays an important role in integrating convergent proprioceptive and cutaneous sensory inputs.

We next sought to determine the spinal regions activated by tasks requiring proprioceptive and cutaneous sensory input. To address this, we examined the expression of the early immediate gene c-fos, used as a correlate of neuronal activity (Hunt, Pini, and Evan 1987; Morgan and Curran 1986), during rest, swim (integrating predominantly proprioceptive input), and walk (integrating proprioceptive and cutaneous inputs) (Muir and Steeves 1995; Gruner and Altman 1980). During walking, recruiting both proprioceptive and cutaneous sensory inputs (Muir and Steeves 1995; Gruner and Altman 1980), we observed an increase in c-fos positive neurons throughout the deep and ventral laminas, particularly within the medial region of Lamina IV-V (**Figure 1E**). Together, these data highlight the medial deep dorsal horn as a unique region activated by convergent sensory input from proprioceptive and cutaneous primary afferents.

Dorsal horn inhibitory neurons are preferentially recruited during locomotion

We next asked whether the increase in activity during locomotion was restricted to either excitatory or inhibitory interneurons of the deep dorsal horn. To do this we use *vGAT*^{Cre};*Tau*$^{LSL\text{-}LacZ}$ mice and quantified c-fos in inhibitory (c-fos^{+}/LacZ^{+}) and excitatory (c-fos^{+}/LacZ^{-}) neurons. Our results showed that increased c-fos expression following walk is attributed to enhanced activity primarily in inhibitory, but not excitatory neurons (**Figure 2A**). In line with enhanced inhibitory neuron recruitment during sensorimotor behavior, we found that optogenetic activation of sensory afferents is more likely to evoke action potentials (APs) in inhibitory neurons than excitatory neurons (**Figure 2B**), despite receiving similar amplitude inputs (**Figure 2C**). Increased AP discharge in response to sensory input, without any difference in input amplitude, suggests that inhibitory neurons exhibit more excitable intrinsic properties than their excitatory counterparts.

To determine the functional properties of these two deep dorsal horn populations, we performed an electrophysiological characterization of randomly sampled excitatory and inhibitory neurons using the *vGluT2*^{Cre};*R26*$^{LSL\text{-}TdTomato\ (Ai14)}$ and *vGAT*^{Cre};*R26*$^{LSL\text{-}TdTomato\ (Ai14)}$ lines, respectively. Cell-attached recordings showed that more inhibitory neurons exhibit spontaneous action potential (sAP) discharge than excitatory neurons (**Figure 2D-E**). Of the spontaneously active neurons, inhibitory neurons showed higher sAP frequency with a lower coefficient of variation (**Figure 2F-G**). Again, these findings suggest inhibitory neurons are more active than their excitatory counterparts, and are a likely source of tonic inhibition. To further explore the intrinsic excitability of these two populations, we next examined their responsiveness to depolarizing current injection. Using previously established AP discharge phenotypes (Browne et al. 2020), we found the majority of excitatory and inhibitory neurons within the deep dorsal horn exhibit tonic firing (TF) AP discharge patterns (**Figure 2H**). TF INs could be further classified into two subcategories: TF-non-accommodating (TF_{Na}) and TF accommodating (TF_{Ac}). Comparing the two populations, TF_{Na} was more frequently observed in inhibitory neurons whereas TF_{Ac} and delayed firing (DF) were more frequently observed in excitatory neurons (**Figure S1A-B**). These discharge patterns are consistent with increased AP threshold adaptation in excitatory neurons (**Figure S1C**). Inhibitory neurons showed a lower latency to the first AP (**Figure 2I**), an increased number of APs (**Figure 2J**), and increased instantaneous AP frequency (**Figure 1K**). When examining AP properties, we also found significant differences in AP threshold and AP kinetics that promote increased excitability in inhibitory neurons (**Figure 2L-P, Figure S1D-F**). Lastly, inhibitory neurons displayed a more depolarized

resting membrane potential (RMP) than excitatory neurons (**Figure S1G**), with no differences in other passive membrane properties (**Figure S1H-I**).

Together, these data demonstrate that inhibitory and excitatory neurons within the deep dorsal horn process sensory information differently. Inhibitory neurons show more excitable intrinsic properties, underlying their increased responsiveness to sensory input, which allows for their preferential recruitment during locomotor activity. Further, their intrinsic properties suggest a role in faithful encoding of stimulus intensity and duration. We therefore used genetic strategies to target inhibitory interneurons within the medial deep dorsal horn and study their role in motor performance.

Parvalbumin-expressing inhibitory interneurons, confined to the medial deep dorsal horn are previously uncharacterized

The calcium binding protein parvalbumin (PV) is a known marker of inhibitory INs in the brain and spinal cord (H. Kim et al. 2016; Nahar, Delacroix, and Nam 2021; Boyle et al. 2019). Using the $PV^{TdTomato}$ mouse line, we identified a population of PV^{+} interneurons confined to medial deep dorsal horn (**Figure 3A**), which we identified as the region receiving convergent sensory input (**Figure 1C-D**). We named these cells deep dorsal horn parvalbumin-expressing interneurons (dPVs), and found that they represent 18$\pm$5.45% of laminae IV-V (data not shown). dPVs also show limited co-expression with two previously characterized inhibitory deep dorsal horn interneuron populations defined by the transcription factor Satb2 and the orphan nuclear hormone receptor RORβ (**Figure S2H**). Thus, dPVs represent a substantial population of uncharacterized inhibitory INs confined to the medial deep dorsal horn.

Given that PV^{+} interneurons within lamina IIi-III of the spinal cord are a mixed excitatory/inhibitory population (Gradwell et al. 2022; Abraira et al. 2017), we investigated the neurochemical phenotype of dPVs using excitatory and inhibitory markers. We found that dPVs are largely inhibitory (**Figure 3B**), with the majority being purely glycinergic (**Figure 3C**). In line with an inhibitory neurotransmitter phenotype, the majority of dPVs exhibited sAP discharge and were classified as TF_{Na} in response to depolarizing current injection (**Figure 3D, E**). These electrophysiological characteristics were similar to those of inhibitory interneurons within the same region (**Figure S2A-G**), however dPVs exhibited higher sAP frequency and lower sAP coefficient of variation (**Figure S2C,D**).

To further characterize dPVs, we performed detailed morphological reconstructions. Compared to inhibitory PV INs in the superficial dorsal horn, dPVs showed larger soma, smaller sholl regression coefficient and increased spine density, suggesting larger neurons that integrate more sensory input. Further, dPVs morphology in cervical, lumbar and thoracic segments suggested heterogeneity throughout the rostrocaudal axis. While cervical and lumbar dPVs have increased spine density, thoracic dPVs show smaller sholl regression coefficient, suggesting they have more complex neuronal harbors. Together, the morphology of dPVs suggests a role in integration of incoming inputs, particularly in spinal cord segments involved in limb control. Further, lumbar dPVs relative simple neuronal harbors suggest local processing.

In summary, these data suggest that dPVs are a novel population of inhibitory interneurons confined to the medial deep dorsal horn that act as a source of highly reliable tonic inhibition. In lumbar segments, essential for hindlimb control and locomotion, dPVs integrate increased amounts of sensory inputs, which they may project locally. We next sought to determine the types of sensory input that regulate dPVs' activity.

dPVs integrate convergent proprioceptive and cutaneous input from the hindlimbs.

Since dPVs are confined to deep dorsal horn, a region innervated by paw inputs and integrating convergent sensory input (**Figure 3A**), we next tested whether dPVs integrate proprioceptive and cutaneous inputs from the paw. To address this, we injected the paw with the anterograde tracer CTB and found that sensory afferents from the paw provide direct input to dPVs (**Figure S3A-B**). To assess the relative contribution of proprioceptive and cutaneous afferents to dPVs' sensory input, we utilized our genetic strategy to label both modalities (**Figure 3F**). This approach revealed that both populations provide input to dPVs, with a bias toward cutaneous input. Further, in line with their extensive dendritic arborizations (**Figure S2K**), cutaneous and proprioceptive input preferentially target dPVs dendrites (**Figure S3C**). Given the location of dPVs within the deep dorsal horn, the most likely source of cutaneous input to dPVs are low-threshold mechanoreceptors (LTMRs). Thus, we next examined inputs from different classes of LTMR to the lumbar spinal cord (Abraira and Ginty 2013; Rutlin et al. 2014; Bai et al. 2015; Luo et al. 2009). Mapping input terminations showed that Aβ-Field and Aβ-Rapidly Adapting (Aβ-RA) terminals form direct inputs onto dPVs, while C- and Aδ-LTMRs terminate superficially (**Figure 3G-H, Figure S3D**). This finding is in line with dPVs receiving more input from LTMRs that originate from the glabrous skin of the paw (Aβ-Field and Aβ-RA) then from hairy skin (C- and A -LTMRs) (Abraira et al. 2017)

To validate these findings and examine their functional implications, we next performed slice electrophysiology where dPVs activity was recorded in response to optogenetic stimulation of different sensory modalities (**Figure 3I**). Consistent with our histology results, we found that most monosynaptic input to dPVs originates from proprioceptors, Aβ-RA, and Aβ-field (**Figure 5J-K, Figure S3E-G**). The incidence and amplitude of optically-evoked EPSCs (oEPSCs) was in line with the topographical overlap between each afferent population's central terminations and the dPV population (**Figure S3D**). Additionally, we found that dPVs also receive polysynaptic input from proprioceptors, Aβ-, Aδ-, and C-LTMRs (**Figure 3L-M**). These polysynaptic inputs are likely to be mediated by interneurons within the LTMR-recipient zone (LTMR-RZ), heavily innervated by LTMRs (Abraira et al. 2017). To further investigate these circuits, we chose to target two large populations of excitatory (CCK) and inhibitory (RORβ) interneurons within the LTMR-RZ (Abraira et al. 2017). Both LTMR-RZ populations were shown to provide input to dPVs (**Figure 3N-P**). Finally, we show that dPVs receive direct cortical inputs that are capable of eliciting AP discharge (**Figure S3H-M**). Therefore, dPVs integrate information from sensory afferents (primarily proprioceptors and LTMRs innervating glabrous skin), LTMR-RZ excitatory and inhibitory interneurons, and descending cortical projections. These data provide strong evidence against modality-specific labeled lines and instead suggest a diverse ensemble of inputs converge onto common pathways to inform motor output.

dPVs activity is shaped by walking states and activation of sensory inputs.

We next sought to better understand how dPVs activity may be altered in different states. To determine whether dPVs are active during locomotion, we examined c-fos expression in dPVs following rest and walking (**Figure 4A**). In line with our previous data showing enhanced activity in inhibitory neurons of the medial deep dorsal horn, we found an approximately five fold increase in c-fos expressing dPVs following walk. Further, application of a 'cocktail' containing 5-HT, NMDA, and dopamine used in vitro to evoke rhythmic output that mimics locomotor activity (Jiang, Carlin, and Brownstone 1999), depolarized dPVs to increase sAP frequency (**Figure 4B-H**), and in some instances (3/7) evoked rhythmic bursts of AP discharge (**Figure 4D**). These data show that dPVs are active during locomotor activity and may participate in locomotor rhythmogenesis. Interestingly, blocking synaptic transmission enhances dPV sAP frequency (**Figure 4I**). This demonstrates that dPVs have the intrinsic properties to support spontaneous discharge, without a requirement of synaptic input. In contrast, an increase in sAP frequency following synaptic block suggests dPV activity is predominantly regulated by inhibitory synaptic transmission under normal conditions. Given dPVs activity is not dependent on synaptic input, we next examined the role sensory afferents play in shaping dPV output. The regularity of dPV

output (**Figure S2B, E)** promotes oscillation-like activity. We found sensory afferent stimulation could 'reset' the timing of dPVs spontaneous AP discharge to reduce variability in output timing (**Figure 4J-K**). The ability of a sensory afferent population to evoke AP discharge was in-line with their input strength (**Figure 4L, Figure 3K**). Taken together, our data shows that dPVs have the intrinsic properties to support spontaneous activity. Sensory input plays an important role in shaping this activity to ensure appropriate output timing.

dPVs recruitment during locomotion, responsiveness to a fictive locomotion cocktail, and location within the medial portion of LIV-V suggest a likely role in modulating motor output. Given the wide expression of PV throughout the brain, spinal cord, and dorsal root ganglia (DRG), we next sought to devise an experimental approach to specifically target and manipulate the activity of the dPV population.

dPV ablation alters stride frequency

To study the function of dPVs we used an intersectional genetic approach. First, we found preferential recombination within the deep dorsal horn when using the *PV*^{FlpO} mouse-line, avoiding the more dorsal PV-IN population (**Figure S4C**). To restrict expression to the spinal cord, we then examined the co-expression of dPVs with known genetic lineages. As dPVs lie in the dorsoventral interface, we chose to focus on Islet1, and Lbx1 that give rise to dorsal lineages and Sim1, the genetic origin of the ventral V3 population (Gross, Dottori, and Goulding 2002, 1; Lu, Niu, and Alaynick 2015). As we found that dPVs are almost exclusively derived from the Lbx1-lineage (**Figure S4A-B**), we generated an Lbx1^{Cre};*PV*^{FlpO} intersectional approach to target dPVs throughout the rostrocaudal axis of the spinal cord, while avoiding recombination within the more superficial dorsal horn, ventral horn, and DRG (**Figure 5A, Figure S4E**). The brain was largely devoid of neuronal expression, however, recombination was observed in the cerebellum and brainstem (**Figure S4F-H**). To specifically ablate the dPV population we utilized an intersection of *PV*^{FlpO};Lbx1^{Cre};Tau$^{LSL\text{-}FSF\text{-}DTR}$ with intrathecal (I.T.) injection of diphtheria toxin (DTx), prepared in a hyperbaric solution, shown to restrict DTx to the spinal cord (Bourane et al. 2015; Albisetti et al. 2019). We therefore generated mice with ablated dPVs (dPV^{abl}: *PV*^{FlpO};Lbx1^{Cre};Tau$^{LSL\text{-}FSF\text{-}DTR}$ injected with DTx) and non-manipulated dPVs (dPV^{norm}: *PV*^{FlpO} or Lbx1^{Cre};Tau$^{LSL\text{-}FSF\text{-}DTR}$ injected with DTx) (**Figure 5B-D, Figure S4I-M**).

After developing an approach to specifically target dPVs, dPV^{norm} and dPV^{abl} mice were run on a treadmill at different speeds. At speeds greater than 20cm/s, dPV ablation causes an increase in stride frequency and decrease in swing time without any changes to stance (**Figure 5E-H)**. To increase stride frequency, animals shorten their stance time with minimal changes to swing (Goslow Jr., Reinking, and Stuart 1973; Halbertsma 1983). Thus, we hypothesize that dPVs' primary role is to modulate step timing, with changes to swing time as a secondary effect. In line with this hypothesis we observed a change in the phase of the transition from stance to swing in dPV^{abl} mice (**Figure 5I**). To better understand how dPVs shape motor output, we performed electromyogram (EMG) recordings from hindlimb flexors and extensors in response to cutaneous nerve stimulation in dPV^{norm} and dPV^{abl} mice (**Figure 5J-N**). dPV ablation decreased muscle response latency in both flexors and extensors following ipsilateral (**Figure 5J-L, Figure S5E-F**) and contralateral (**Figure 5M-N**) cutaneous afferent stimulation. Thus, these data suggest that under normal circumstances dPVs delay the transmission of sensory information. Loss of dPV-mediated inhibition promotes earlier recruitment of motoneurons, leading to altered step timing. These findings strongly support a role for dPVs in shaping motor output timing.

Given dPVs receive direct cutaneous input (**Figure 3F-K**), we also tested their involvement in corrective motor reflexes. dPV^{abl} and dPV^{norm} mice were allowed to walk on a beam with different shapes and sizes, a horizontal ladder with changing rung patterns, and a rotarod**.** Overall, dPV^{abl} and dPV^{norm} did not show major differences in performance on all three tasks (**Figure S5A-C**)**.** However, dPV^{abl} mice showed a tendency for fewer slips

and faster walk on the beam, and were able to maintain their walk at higher rotarod speeds (**Figure S5A,C**). In line with these findings, dPV^{abl} mice were also able to reach higher speeds on the treadmill (**Figure S5D**). Taken together, these data suggest that dPVs play an important role in regulating stride frequency during high speed walk by modulating the stance to swing transition phase, but do not influence corrective motor reflexes.

dPVs ablation alters joint kinematics at the transition from stance to swing

To determine if changes to pose contribute to the altered locomotor parameters, we next examined mouse kinematics. To do so, mice were walked on the treadmill at 20 cm/s, a speed in which we did not detect a change in stride frequency, which would in-turn lead to stride compensation and alter kinematics (**Figure 5H**). Using DeepLabCut, we tracked hindlimb pose and calculated joint angles throughout the step cycle (**Figure 6A-C**). We noticed the most profound differences in joint angles were seen at the transition from stance to swing (**Figure 6C**). Therefore, we compared joint angles at the posterior extreme position (PEP), occurring at the transition of stance to swing. As a reference, we also compared joint angles at the anterior extreme position (AEP). dPV^{abl} mice showed a decrease in knee- and ankle- PEP angles, and an increase in MTP- PEP angle (**Figure 6D**), with no significant changes in joint angles during AEP (**Figure 6E**). Altered limb kinematics at lower speeds, where stride frequency was unaffected, suggests dPVs play an important role in shaping the magnitude of muscle activation. Further, changes in limb kinematics specific to PEP indicate that dPVs role in locomotion is phase dependent. This phase specificity is in contrast to the observation of altered joint angles across the hindlimb, suggesting dPVs influence is not restricted to a specific motor pool.

To test the ability of dPVs to modulate the magnitude of muscle activation we designed a paired nerve assay in which stimulation of a second cutaneous nerve evokes inhibitory pathways that suppress a motor response mediated by the first cutaneous nerve (**Figure 6F-J)**. We started by stimulating a single nerve and calculated the averaged expected response (black trace, **Figure 6G**). Next, both nerves were stimulated at varying delays (see **Figure S7A-B** and methods for further explanation) and the summed response (blue trace, **Figure 6G**) was compared to the expected response to reveal inhibition or its lack of. Using this approach we observed a loss of local (ipsilateral) inhibition to flexor and extensor muscles following dPV ablation (**Figure 6F-H, Figure S7C**). Although we also observed loss of contralateral inhibition to flexor muscles in dPV^{abl} mice (**Figure 6I-J, Figure S7D**), we found no significant difference in diagonal, hindlimb or forelimb coupling, suggesting that dPVs' role is mostly local. Consistent with this, we found only a small portion (3.05% $\pm$ 0.79) of midline crossing dPVs (**Figure S6D**). Together, these data suggest that by inhibiting the transmission of sensory information onto motor circuits, dPVs play an important role in modulating the magnitude of flexor and extensor muscle activity, and in-turn shape hindlimb kinematics.

dPVs ablation impairs interlimb coordination

Interlimb coordination depends upon the timing of swing-stance and stance-swing transitions. Given that we observed changes in the stance-to-swing transition in dPV^{abl} mice we next asked whether dPV ablation alters interlimb coordination. To do so, we calculated the phase coupling between every two sets of limbs in dPV^{abl} and dPV^{norm} mice. Phase coupling values range from 0 to 1, where 0/1 represent full limb coupling (in-phase), 0.5 represents no coupling (anti-phase) and 0.25/0.75 represent partial coupling (out-of-phase, **Figure S6A**). During high speed locomotion (40-100 cm/s), while ipsilateral coupling values of dPV^{norm} congregate around 0.5 (anti-phase), values of dPV^{abl} were more dispersed and transitioned toward out-of-phase values. On the other hand, diagonal, and left-right (forelimbs or hindlimbs) coupling remained unchanged between dPV^{abl} and dPV^{norm} (**Figure S6B**).

Gait transitions rely upon appropriate limb coordination adjustments (Danner et al. 2016). Mice were shown to transition from walk to trot to gallop and bound with increasing speed (Bellardita and Kiehn 2015). To determine whether dPV ablation alters gait transitions, we classified each step cycle as one of these four main gaits. While dPV^{norm} fully transitioned to trot at 60 cm/s and alternated between trot and gallop at 80 cm/s, dPV^{abl} retained the walking gait at higher speeds and refrained from using gallop at 80 cm/s (**Figure S6C**). Taken together, our results suggest that dPV circuits modulate the timing of muscle response to alter limb coordination and gait transitions at higher speeds.

dPVs form a diffuse inhibitory circuit with ventral horn spinal cord motor networks

Our behavioral assessments suggest that dPVs regulate the timing and magnitude of muscle activity. These findings raise the question: What are dPVs' output targets that support such a multifunctional role in motor action? To address this question, we first visualized dPVs outputs (**Figure 7A**). Our map revealed a diffuse pattern of dPVs axon terminals through the deep dorsal and ventral horn, suggesting output divergence. We next used immunohistochemistry tools to further elucidate dPVs targets (**Figure 6B**). We found dPV contacting other dPVs, pre-motor neurons such as Renshaw cells and V0cs, and motor neurons (MN).

Our behavioral experiments revealed that dPV ablation results in hyperflexion of some joints and hyperextension of others. This suggests that dPVs modulate flexor and extensor motor neurons. Lbx1-derived premotor interneurons innervating flexor and extensor MNs can be segregated based on birth order; the former born at E10.5 and the later at E12.5 (Tripodi, Stepien, and Arber 2011). EdU labeling of dPVs shows that 31.57$\pm$0.75% of dPVs are born at E10.5 while 43.57$\pm$0.04% are born at E12.5 (**Figure S8A-B)**. These findings indicate that dPVs innervate both flexors and extensors, with a bias toward extensor MNs. Consistent with this finding, labeling of dPV contacts onto flexor and extensor MNs of the hindlimb highlights a bias toward extensor MNs (**Figure 7C, Figure S8C-E)**.

Next, we performed slice electrophysiology and recorded from potential postsynaptic targets while optically stimulating dPVs. Consistent with our histological findings, we found monosynaptic inhibitory inputs onto other dPVs, V0cs, MNs within the medial motor pool, MNs within the lateral motor pool, and putative foot MNs. While dPV-mediated inhibition was most frequent and strongest onto other dPVs, the incidence and amplitude of dPV-mediated inhibition onto other populations was relatively equal (**Figure 7E-F**). In-line with a glycinergic phenotype (**Figure 3C**), dPV-mediated inhibition was predominantly glycinergic (**Figure S8F**) and the majority of dPV puncta were GlyT2-positive (**Figure S8G-H**). Together, these data highlight dPVs as a source of divergent inhibition throughout pre-motor and motor networks, with preferential direct inhibition onto extensor MNs.

DISCUSSION

Sensory information from proprioceptive and cutaneous afferents constantly informs the way we move. However, the circuits that mediate sensory modulation of locomotion remain largely unknown. Here, we identify the medial deep dorsal horn as the epicenter of sensory convergence and highlight inhibitory interneurons within this region as key players in sensorimotor processing. We find a new population of inhibitory interneurons, dPVs, that receive convergent sensory input and are a source of divergent inhibitory control over premotor and motor circuits. Ablation of dPVs altered the magnitude and timing of motor output in a phase and state-dependent manner. Our studies identify a novel inhibitory pathway linking sensory and motor circuits, providing evidence for a model of early sensory convergence and instructive divergence in sensorimotor processing to ensure contextually relevant movement.

The medial deep dorsal horn is a node for multimodal sensorimotor processing

In general terms, the spinal cord is divided into two regions: the dorsal horn, responsible for the processing of cutaneous sensory information, and the ventral horn, responsible for motor control. Despite our knowledge that cutaneous input to the dorsal horn of the spinal cord can modulate motor output, the identity of circuits underlying sensorimotor processing remain unclear. Previous studies provide strong evidence for the medial deep dorsal horn as an important site for sensorimotor control. This region is a point of intersection for cutaneous and proprioceptive afferents (Levinsson et al. 2002; Kniffki, Schomburg, and Steffens 1981; Edgley and Jankowska 1987b), corticospinal fibers (Asante and Martin 2013; Martin 1996; Bareyre et al. 2005), and rubrospinal fibers (Liang, Paxinos, and Watson 2012; L. T. Brown 1974; Antal et al. 1992). In addition, the medial deep dorsal horn has been shown to house 'reflex-encoder' sensory relay neurons (Levinsson et al. 2002; Schouenborg et al. 1995), a substantial portion of premotor neurons (Levine et al. 2014; Stepien, Tripodi, and Arber 2010; Coulon, Bras, and Vinay 2011; Hongo et al. 1989; Puskár and Antal 1997), motor synergic encoders (Levine et al. 2014), as well as neurons capable of promoting motor output and rhythmic pattern generation (Tresch and Bizzi 1999; Saltiel, Tresch, and Bizzi 1998). Together, these findings strongly implicate the medial deep dorsal horn as the first site of sensory information selection. Our genetic approaches identify the medial deep dorsal horn as a region of proprioceptive and cutaneous (Aβ-Field and Aβ-RA LTMRs) convergence. Our c-fos data further implicates the medial deep dorsal horn as a region involved in locomotion. In particular, we found preferential recruitment of inhibitory interneurons within this region during locomotor behaviors.

To explain the preferential recruitment of inhibitory interneurons during locomotion, we performed an electrophysiological characterization of inhibitory and excitatory neurons within the deep dorsal horn. In comparison to the clear heterogeneity of discharge properties displayed in the superficial dorsal horn (Browne et al. 2020; Grudt and Perl 2002; Punnakkal et al. 2014) we found these properties were more similar in inhibitory and excitatory neurons within the deep dorsal. This result is in line with single-cell RNA sequencing data showing that while superficial dorsal populations exhibit distinct gene expression patterns, neurons within the deep dorsal and ventral horn were less distinct (Russ et al. 2021; Sathyamurthy et al. 2018). In line with previous reports (Derjean et al. 2003; Le Franc and Le Masson 2010), we observed a predominance of tonic firing cells within the deep dorsal horn. Tonic firing promotes integration and highly reliable spike transfer to produce faithful signal transmission (Kempter, Gerstner, and van Hemmen 1998; Le Franc and Le Masson 2010). Previous work has shown that modulatory control allows deep dorsal horn neurons to switch between three forms of firing modes: tonic, plateau, and bursting (Derjean et al. 2003). Such 'switching' may provide task-dependent flexibility to deep dorsal horn circuits. We also found, unlike within the superficial dorsal horn, that deep dorsal horn neurons are often spontaneously active. This suggests deep dorsal horn neurons provide a constant inhibitory/excitatory tone that can be differentially tuned depending on their current inputs. Simultaneous inhibition and excitation can work as a push-pull mechanism for gain control, i.e. to induce a divisive change in the input-output relationship of neurons. This was demonstrated in the feline extensor motor neurons, where tonic inhibitory and excitatory inputs increased response gain to phasic sensory input (Johnson et al. 2012). Taken together, these findings suggest the deep dorsal horn, and inhibitory interneurons in particular, integrate sensory inputs to reliably translate stimulus intensity and duration to downstream targets.

dPVs circuit for convergence and divergence of proprioceptive and cutaneous information

To understand the role of sensory input in locomotion, early studies removed the sensory component and examined animal walk (L. J. Bouyer and Rossignol 1998; Goldberger 1977; Wetzel et al. 1976; T. G. Brown and Sherrington 1911; Akay et al. 2014; Acevedo and Díaz-Ríos 2013). These experiments demonstrated that, although not necessary for the generation and maintenance of locomotion, sensory input is crucial for adjusting

the step cycle to achieve fluency of movement, particularly in response to a changing environment. Two sensory modalities that directly shape locomotion are cutaneous and proprioceptive feedback; the first signals skin distortion (indentation, vibration, slip) through low threshold mechanoreceptors (LTMRs) innervating the skin, and the latter signals body position and movement through specialized mechanoreceptors in muscle and joints. Therefore, understanding how each modality influences locomotion has been the subject of investigation for many years. Together, these studies show cutaneous and proprioceptive afferents can regulate the magnitude of muscle activity and the timing of the step cycle, in particular the stance-to-swing transition (Hiebert and Pearson 1999; C. S. Sherrington 1910; O. Andersson and Grillner 1981; 1983; Kriellaars et al. 1994; Whelan, Hiebert, and Pearson 1995; Guertin et al. 1995; J and Kg 1980; Pearson, Ramirez, and Jiang 1992; Stecina, Quevedo, and McCrea 2005; Frigon, Sirois, and Gossard 2010; Duysens 1977; J and Kg 1980; Grillner and Rossignol 1978; Whelan, Hiebert, and Pearson 1995). Despite ample evidence for sensory control of motor output, our understanding of the underlying spinal circuits remains limited.

Proprioceptive and cutaneous inputs represent different aspects of the sensory experience. The question that arises is whether information from the two modalities work together to modulate the step cycle? Or in other words, do these inputs remain in parallel pathways or do they converge to adjust motor output? Here, we genetically identify a population of interneurons in the spinal cord deep dorsal horn that integrate convergent proprioceptive and cutaneous input from LTMRs, dPVs. To our knowledge dPVs represent the first genetically identified inhibitory neurons that integrate touch and proprioceptive inputs in the spinal cord. Previous work showing facilitation or depression of proprioceptive reflexes when coupled with cutaneous afferent stimulation (Kniffki, Schomburg, and Steffens 1981; Lundberg, Malmgren, and Schomburg 1977; Pierrot-Deseilligny et al. 1981) supports the existence of proprioceptive and cutaneous afferent convergence onto a common pathway. Studies examining convergent cutaneous and proprioceptive input within the primary somatosensory cortex demonstrated that the majority of multimodal neurons exhibit a preferred modality (S. S. Kim et al. 2015). Similarly, we show dPVs are most responsive to proprioceptive input, followed by Aβ-Field and Aβ-RA LTMRs. Interestingly, these are the same afferent populations that are most likely to be activated during locomotion as they innervate the glabrous skin of the paw. It is unclear whether the response of dPVs to one modality can be altered in the presence of another, as shown for multimodal cells within the superior colliculus (Stein and Meredith 1990). The presence of disynaptic inhibitory and excitatory pathways indicates dPVs response to one modality could be shaped by the simultaneous integration of another.

We also show that dPVs output is highly divergent, spreading throughout the deep dorsal horn, intermediate zone (IZ), and ventral horn to form synaptic contacts with premotor circuits and MNs. Therefore, we reveal a coupling between dorsal horn inhibitory interneurons, premotor and motor networks. Indeed, premotor neurons within the IZ have previously been shown to receive polysynaptic cutaneous and proprioceptive input via the dorsal horn (Jankowska, Maxwell, and Bannatyne 2007; Edgley and Jankowska 1987b). Given the existence of a direct and indirect pathway to motor output, it is tempting to speculate a central mechanism for sensory information selection. For example, following stimulation of group II afferents, activation of dorsal horn interneurons precedes the response of neurons within the IZ (Jankowska, Slawinska, and Hammar 2002), suggesting parallel pathways to motor neurons/downstream targets that can be modulated at multiple levels. Transmission between group II afferents and dorsal horn interneurons is suppressed by serotonin (Hammar et al. 2004; Jankowska et al. 2000); in which case, IZ interneurons become more dependent on direct group II inputs. In contrast, presynaptic inhibition of group II afferents (Jankowska, Bichler, and Hammar 2000) would allow cutaneous inputs to the deep dorsal horn to hold greater influence. Such an arrangement permits the activity of dPVs, and their downstream targets, to be context dependent, shaped by the complex assortment of sensory information present at any given moment.

dPVs extensive axonal projections suggest widespread inhibitory control over a variety of cell types involved in sensorimotor processing; an organization well suited for the coordination of motor output. In line with this finding, inhibitory interneurons within the deep dorsal horn that receive group II afferent input have previously been shown to have axonal projections spreading from the deep dorsal horn to ventral areas. This is in contrast to excitatory interneurons, whose axonal projections extend much less ventrally (Bannatyne et al. 2006). Despite the widespread divergence of dPVs' output, retrograde labeling suggests preferential targeting of extensor MNs. Given dPVs genetic origin and confinement to the medial deep dorsal horn, our finding supports a medio-lateral spatial segregation of Lbx1-derived extensor and flexor premotor interneurons (Tripodi, Stepien, and Arber 2011). These findings provide further evidence for a disynaptic link between proprioceptors and extensor MNs (Angel, Jankowska, and McCrea 2005; Conway, Hultborn, and Kiehn 1987; McCrea 1998; Pearson, Misiaszek, and Fouad 1998), identify a new disynaptic pathway linking cutaneous input to extensor MNs, and further points toward the modular architecture of spinal circuits (Gatto et al. 2021; Gradwell and Abraira 2021).

We propose that convergence and divergence by dPVs improve the efficiency and accuracy of locomotion modulation by sensory inputs. Comparison with other sensory systems suggests convergence as a mechanism for the emergence of complex processing that represents more aspects of the sensory experience. For example, convergence of visual inputs into the primary motor cortex is thought to underlie neurons' complex receptive fields (RFs) that are selective to movement, orientation or position (Ringach 2004; Martinez and Alonso 2003; Spillmann 2014). Similarly, neurons in the inferior colliculus (IC) of the auditory system process information on the frequency, intensity, and timing of auditory, as well as non-auditory oculomotor and somatosensory cues (Ito, Bishop, and Oliver 2016; Gruters and Groh 2012). The convergence of these inputs onto IC neurons likely underlies one's ability to attribute all aspects of sound to one entity, orient to the sound, and distinguish it from self-generated sounds (Gruters and Groh 2012). Input convergence takes place at multiple stages of sensory processing. In the visual pathway, convergence happens as early as the level of the retina, where input from photoreceptors and inhibitory neurons converge onto ganglion cells to shape their RF. Early convergence allows for processed input to diverge and reconverge, a mechanism shown in the olfactory system of drosophila to reduce network noise and improve neural speed and accuracy (Jeanne and Wilson 2015).

In the case of dPVs, convergence of proprioceptive and cutaneous inputs, which then diverges across networks, can facilitate more efficient motor output, integrating both inputs, and informing multiple motor programs. Assume a limb encounters a slippery surface. Simultaneously, cutaneous feedback signals to prolong stance whie proprioceptive feedback signals it is time to terminate stance and initiate swing. The two modalities will be processed by dPVs and diverged to appropriate motor networks to prolong the stance of the encountered limb, while appropriately adjusting the other limbs. Here, we provide evidence suggesting dPVs as a model of sensory convergence and divergence to shape motor control through an integration of tactile and proprioceptive input.

Dynamic modulation of locomotion by sensory inputs

Ablation of dPVs evoked changes in animal behavior that were both phase- and state-dependent. dPV^{abl} mice exhibited a speed-dependent increase in step frequency and could achieve higher speeds when compared to control mice. There are a number of potential explanations for this observation. First, dPVs might integrate supraspinal inputs from circuits important for speed regulation such as the cuneiform nucleus, pedunculopontine nucleus, or lateral paragigantocellular nucleus (Caggiano et al. 2018; Capelli et al. 2017; Roseberry et al. 2016). Engagement by these circuits would promote a speed-dependent role for dPVs. Second, dPVs speed dependency could result from integration of proprioceptive and cutaneous input involved

in setting the duration of step cycle phases and therefore locomotion frequency (William P. Mayer et al. 2018; O. Andersson and Grillner 1981; 1983; Akay et al. 2014; Guertin et al. 1995; J and Kg 1980; Stecina, Quevedo, and McCrea 2005; L. J. G. Bouyer and Rossignol 2003a; 2003b; Duysens 1977; Schomburg et al. 1998b; Grillner and Rossignol 1978; Hiebert et al. 1996). Third, dPVs may alter the recruitment of premotor neurons with a speed-dependent role in locomotion, such as the $V0_{D,}$ $V0_{v,}$ V1, V2a, V2b and V3 interneurons (Crone et al. 2008; Gosgnach et al. 2006; Callahan et al. 2019; H. Zhang et al. 2022; Talpalar et al. 2013). Our anatomical, electrophysiological, and EMG data supports contributions from each explanation. We find dPVs receive convergent cortical, cutaneous, and proprioceptive input. Sensory input played an important role in shaping dPV output timing and loss of dPV-mediating inhibition reduced the latency of cutaneous evoked muscle activity. This inhibition is diverse and affects both flexor and extensor motor units by acting on premotor and motor circuits. Together, these data suggest appropriate phase durations rely upon sensory-evoked inhibition to ensure the correct timing of motor unit recruitment.

With increasing speeds, mice sequentially change their gait from walk to trot, gallop and bound (Clarke and Still 1999; Herbin, Gasc, and Renous 2004; Bellardita and Kiehn 2015; Lemieux et al. 2016). Gait expression was shown to depend on different modules of neuronal ensembles (Kiehn 2016). For example, experimental and computational studies suggest that loss of interneurons that mediate low, intermediate and high speed locomotion lead to loss of walk, trot and gallop/ bound, respectively (Talpalar et al. 2013; Bellardita and Kiehn 2015; H. Zhang et al. 2022; Danner et al. 2016). Our data show that mice with ablated dPVs locomote at higher speeds and prefer to maintain a walk gait over trot. Similarly, horses with a mutation in the DMTR3 gene, expressed in Lbx1+ inhibitory interneurons involved in high speed locomotion in mice, have the ability to trot or pace at high speed without breaking into a gallop. (L. S. Andersson et al. 2012). These data suggest that dPVs are particularly important during high-speed locomotion and their ablation evokes a gait shift that promotes faster walking.

Gaits are characterized by distinct patterns of intralimb and interlimb coordination (Bellardita and Kiehn 2015; Lemieux et al. 2016). Therefore, accommodating their altered gait transitions, dPV^{abl} mice showed altered intalimb and interlimb forelimb- hindlimb but not left-right coordination. This is surprising, given we did not find evidence for propriospinal dPV neurons, those thought to be responsible for modulating hindlimb- forelimb ipsilateral coordination (H. Zhang et al. 2022; Danner et al. 2016; Kiehn 2016). This result could be a consequence of the specific ablation of dPVs in the lumbosacral region in our study. Following ablation of dPVs in the lumbo-sacral region, impaired hindlimb, but not forelimb intralimb coordination can manifest as a change in hindlimb-forelimb interlimb coordination. Future studies where dPVs in both cervical and lumbar are ablated will resolve this question.

Tracking of hindlimb pose during treadmill walk showed hyperflexed joint angles in the transition between stance and swing of mice with ablated dPVs. Further, we show that the stance-to-swing transition occurred later in the step cycle of dPV^{abl} mice. Sensory input, particularly from Aβ-LTMRs and type Ib proprioceptors, has been shown to modulate flexion, and the timing of the stance-to-swing transition. For example, previous work indicated the hip joint must extend to an angle of at least 95 degrees for swing onset (Grillner and Rossignol 1978). Another study showed that even when the hip joint was sufficiently extended, flexing the ankle or loading ankle extensors inhibited flexor bursts, a role attributed to GTO-Ib afferents (J and Kg 1980). This suggests that under normal conditions dPVs inhibit flexion to promote a smooth stance to swing transition. Therefore enhanced flexion of the hip and ankle joints following dPVs' ablation disrupts the transition from stance to swing. Other sensory input, such as from cutaneous afferents from the paw, have also been shown to guide the step cycle. Similar to Ib proprioceptive, Aβ-LTMR afferents from the ventral paw delay the initiation of flexion when stimulated during stance (Duysens 1977). Therefore, delayed flexion could also be produced by

reducing dPV-mediated inhibition. Our EMG data complements these behavioral findings. dPV^{abl} mice showed reduced response latency and reduced cutaneous evoked inhibition – likely resulting in enhanced MN activation across multiple muscle groups. These effects were observed in the flexors and extensors of the hindlimb. Though in agreement with our behavioral and electrophysiological data, this was at odds with our anatomical data highlighting an extensor bias. It is likely the deficits observed following dPV ablation are due to loss of direct inhibition, primarily onto extensor MNs, as well as indirect inhibition of premotor neurons, such as the V1 and V2b populations shown to be involved in flexor-extensor alternations (Britz et al. 2015; J. Zhang et al. 2014). Therefore, convergent cutaneous and proprioceptive input activate a divergent inhibitory network to shape the magnitude and timing of muscle activity. In-turn loss of inhibition following dPV ablation disrupts flexor/extensor balance and phase transition timing.

It is interesting that dPV^{abl} mice displayed no deficits in tasks assessing dynamic corrective reflexes. Both Proprioceptive and LTMR input have important contributions to corrective reflexes (L. J. Bouyer and Rossignol 1998; Goldberger 1977; Akay et al. 2014), and our EMG data shows dPVs integrate these inputs. Further, excitatory interneurons within the deep dorsal horn have previously been shown to modulate dynamic corrective reflexes (Gatto et al. 2021). Though not assessed here, A-nociceptors have been shown to innervate Lamina IV, where dPVs are located (Dubin and Patapoutian 2010). Therefore, it would be interesting to examine the contribution of dPVs to nociceptive withdrawal reflexes. Together, these findings suggest dPVs have a specific role in modulating the step-cycle, particularly at high-speeds, and do not contribute to dynamic corrective reflexes.

Conclusions

Here, we characterize the medial deep dorsal horn as the spinal region that integrates proprioceptive and cutaneous sensory input and identify inhibitory interneurons within this region as key players in sensorimotor processing. Our simplified model, using dPVs, demonstrates that cutaneous and proprioceptive inputs converge on inhibitory interneurons within the medial deep dorsal horn to regulate the gain and timing of motor output. We suggest that cutaneous and proprioceptive convergence is not functionally redundant. Instead, convergence is necessary for the emergence of more complex processing and its occurrence at early relays of network processing increases the diversity of mechanisms by which sensory information can influence network activity for the purpose of movement execution and refinement. Moreover, we propose two ways by which deep dorsal horn interneurons mediate dynamic sensory modulation of locomotion, i.e.,that is state and phase dependent. First, by integrating inputs from multiple sources (cutaneous, proprioceptive, cortical, and local) the output of deep dorsal horn interneurons is highly regulated, thereby incoming inputs are only relayed under certain circumstances. Second, excitatory and inhibitory deep dorsal horn interneurons might work in tandem to maintain the excitation-inhibition push-pull of spinal cord motor networks. We propose that divergent inhibitory control maintains this balance by adjusting the gain of sensorimotor pathways to ensure contextually relevant motor output.

REFERENCES

Abraira, Victoria E., and David D. Ginty. 2013. “The Sensory Neurons of Touch.” *Neuron* 79 (4): 618–39. https://doi.org/10.1016/j.neuron.2013.07.051.

Abraira, Victoria E., Emily D. Kuehn, Anda M. Chirila, Mark W. Springel, Alexis A. Toliver, Amanda L. Zimmerman, Lauren L. Orefice, et al. 2017. “The Cellular and Synaptic Architecture of the Mechanosensory Dorsal Horn.” *Cell* 168 (1–2): 295-310.e19. https://doi.org/10.1016/j.cell.2016.12.010.

Acevedo, Jean Marie, and Manuel Díaz-Ríos. 2013. “Removing Sensory Input Disrupts Spinal Locomotor Activity in the Early Postnatal Period.” *Journal of Comparative Physiology. A, Neuroethology, Sensory,*

Neural, and Behavioral Physiology 199 (12): 1105–16. https://doi.org/10.1007/s00359-013-0853-3.
Acton, David, Xiangyu Ren, Stefania Di Costanzo, Antoine Dalet, Steeve Bourane, Ilaria Bertocchi, Carola Eva, and Martyn Goulding. 2019. "Spinal Neuropeptide Y1 Receptor-Expressing Neurons Form an Essential Excitatory Pathway for Mechanical Itch." *Cell Reports* 28 (3): 625-639.e6. https://doi.org/10.1016/j.celrep.2019.06.033.
Akay, Turgay, Hernish J. Acharya, Karim Fouad, and Keir G. Pearson. 2006. "Behavioral and Electromyographic Characterization of Mice Lacking EphA4 Receptors." *Journal of Neurophysiology* 96 (2): 642–51. https://doi.org/10.1152/jn.00174.2006.
Akay, Turgay, Warren G. Tourtellotte, Silvia Arber, and Thomas M. Jessell. 2014. "Degradation of Mouse Locomotor Pattern in the Absence of Proprioceptive Sensory Feedback." *Proceedings of the National Academy of Sciences of the United States of America* 111 (47): 16877–82. https://doi.org/10.1073/pnas.1419045111.
Albisetti, Gioele W., Martina Pagani, Evgenia Platonova, Ladina Hösli, Helge C. Johannssen, Jean-Marc Fritschy, Hendrik Wildner, and Hanns Ulrich Zeilhofer. 2019. "Dorsal Horn Gastrin-Releasing Peptide Expressing Neurons Transmit Spinal Itch But Not Pain Signals." *The Journal of Neuroscience: The Official Journal of the Society for Neuroscience* 39 (12): 2238–50. https://doi.org/10.1523/JNEUROSCI.2559-18.2019.
Anderson, Tatiana M., Matthew D. Abbinanti, Jack H. Peck, Megan Gilmour, Robert M. Brownstone, and Mark A. Masino. 2012. "Low-Threshold Calcium Currents Contribute to Locomotor-like Activity in Neonatal Mice." *Journal of Neurophysiology* 107 (1): 103–13. https://doi.org/10.1152/jn.00583.2011.
Andersson, Lisa S., Martin Larhammar, Fatima Memic, Hanna Wootz, Doreen Schwochow, Carl-Johan Rubin, Kalicharan Patra, et al. 2012. "Mutations in DMRT3 Affect Locomotion in Horses and Spinal Circuit Function in Mice." *Nature* 488 (7413): 642–46. https://doi.org/10.1038/nature11399.
Andersson, O., and S. Grillner. 1981. "Peripheral Control of the Cat's Step Cycle. I. Phase Dependent Effects of Ramp-Movements of the Hip during 'Fictive Locomotion.'" *Acta Physiologica Scandinavica* 113 (1): 89–101. https://doi.org/10.1111/j.1748-1716.1981.tb06867.x.
———. 1983. "Peripheral Control of the Cat's Step Cycle. II. Entrainment of the Central Pattern Generators for Locomotion by Sinusoidal Hip Movements during 'Fictive Locomotion.'" *Acta Physiologica Scandinavica* 118 (3): 229–39. https://doi.org/10.1111/j.1748-1716.1983.tb07267.x.
Angel, M. J., E. Jankowska, and D. A. McCrea. 2005. "Candidate Interneurones Mediating Group I Disynaptic EPSPs in Extensor Motoneurones during Fictive Locomotion in the Cat." *The Journal of Physiology* 563 (Pt 2): 597–610. https://doi.org/10.1113/jphysiol.2004.076034.
Antal, M., G. N. Sholomenko, A. K. Moschovakis, J. Storm-Mathisen, C. W. Heizmann, and W. Hunziker. 1992. "The Termination Pattern and Postsynaptic Targets of Rubrospinal Fibers in the Rat Spinal Cord: A Light and Electron Microscopic Study." *The Journal of Comparative Neurology* 325 (1): 22–37. https://doi.org/10.1002/cne.903250103.
Aristotle's De Motu Animalium. 1986. https://press.princeton.edu/books/paperback/9780691020358/aristotles-de-motu-animalium.
Asante, Curtis O., and John H. Martin. 2013. "Differential Joint-Specific Corticospinal Tract Projections within the Cervical Enlargement." *PloS One* 8 (9): e74454. https://doi.org/10.1371/journal.pone.0074454.
Bai, Ling, Brendan P. Lehnert, Junwei Liu, Nicole L. Neubarth, Travis L. Dickendesher, Pann H. Nwe, Colleen Cassidy, C. Jeffery Woodbury, and David D. Ginty. 2015. "Genetic Identification of an Expansive Mechanoreceptor Sensitive to Skin Stroking." *Cell* 163 (7): 1783–95. https://doi.org/10.1016/j.cell.2015.11.060.
Bannatyne, B. Anne, Stephen A. Edgley, Ingela Hammar, Elzbieta Jankowska, and David J. Maxwell. 2006. "Differential Projections of Excitatory and Inhibitory Dorsal Horn Interneurons Relaying Information from Group II Muscle Afferents in the Cat Spinal Cord." *The Journal of Neuroscience: The Official Journal of the Society for Neuroscience* 26 (11): 2871–80. https://doi.org/10.1523/JNEUROSCI.5172-05.2006.
Bareyre, Florence M., Martin Kerschensteiner, Thomas Misgeld, and Joshua R. Sanes. 2005. "Transgenic Labeling of the Corticospinal Tract for Monitoring Axonal Responses to Spinal Cord Injury." *Nature Medicine* 11 (12): 1355–60. https://doi.org/10.1038/nm1331.
Bellardita, Carmelo, and Ole Kiehn. 2015. "Phenotypic Characterization of Speed-Associated Gait Changes in Mice Reveals Modular Organization of Locomotor Networks." *Current Biology* 25 (11): 1426–36.

https://doi.org/10.1016/j.cub.2015.04.005.
Bourane, Steeve, Katja S. Grossmann, Olivier Britz, Antoine Dalet, Marta Garcia Del Barrio, Floor J. Stam, Lidia Garcia-Campmany, Stephanie Koch, and Martyn Goulding. 2015. "Identification of a Spinal Circuit for Light Touch and Fine Motor Control." *Cell* 160 (3): 503–15. https://doi.org/10.1016/j.cell.2015.01.011.
Bouyer, L. J. G., and S. Rossignol. 2003a. "Contribution of Cutaneous Inputs from the Hindpaw to the Control of Locomotion. I. Intact Cats." *Journal of Neurophysiology* 90 (6): 3625–39. https://doi.org/10.1152/jn.00496.2003.
———. 2003b. "Contribution of Cutaneous Inputs from the Hindpaw to the Control of Locomotion. II. Spinal Cats." *Journal of Neurophysiology* 90 (6): 3640–53. https://doi.org/10.1152/jn.00497.2003.
Bouyer, L. J., and S. Rossignol. 1998. "The Contribution of Cutaneous Inputs to Locomotion in the Intact and the Spinal Cat." *Annals of the New York Academy of Sciences* 860 (November): 508–12. https://doi.org/10.1111/j.1749-6632.1998.tb09090.x.
Boyle, Kieran A., Mark A. Gradwell, Toshiharu Yasaka, Allen C. Dickie, Erika Polgár, Robert P. Ganley, Desmond P. H. Orr, et al. 2019. "Defining a Spinal Microcircuit That Gates Myelinated Afferent Input: Implications for Tactile Allodynia." *Cell Reports* 28 (2): 526-540.e6. https://doi.org/10.1016/j.celrep.2019.06.040.
Britz, Olivier, Jingming Zhang, Katja S. Grossmann, Jason Dyck, Jun C. Kim, Susan Dymecki, Simon Gosgnach, and Martyn Goulding. 2015. "A Genetically Defined Asymmetry Underlies the Inhibitory Control of Flexor-Extensor Locomotor Movements." *ELife* 4 (October). https://doi.org/10.7554/eLife.04718.
Brown, A. G., R. E. Fyffe, P. K. Rose, and P. J. Snow. 1981. "Spinal Cord Collaterals from Axons of Type II Slowly Adapting Units in the Cat." *The Journal of Physiology* 316 (July): 469–80. https://doi.org/10.1113/jphysiol.1981.sp013801.
Brown, L. T. 1974. "Rubrospinal Projections in the Rat." *The Journal of Comparative Neurology* 154 (2): 169–87. https://doi.org/10.1002/cne.901540205.
Brown, Thomas Graham, and Charles Scott Sherrington. 1911. "The Intrinsic Factors in the Act of Progression in the Mammal." *Proceedings of the Royal Society of London. Series B, Containing Papers of a Biological Character* 84 (572): 308–19. https://doi.org/10.1098/rspb.1911.0077.
Browne, Tyler J., Mark A. Gradwell, Jacqueline A. Iredale, Jessica F. Maden, Robert J. Callister, David I. Hughes, Christopher V. Dayas, and Brett A. Graham. 2020. "Transgenic Cross-Referencing of Inhibitory and Excitatory Interneuron Populations to Dissect Neuronal Heterogeneity in the Dorsal Horn." *Frontiers in Molecular Neuroscience* 13: 32. https://doi.org/10.3389/fnmol.2020.00032.
Bui, Tuan V., Turgay Akay, Osama Loubani, Thomas S. Hnasko, Thomas M. Jessell, and Robert M. Brownstone. 2013. "Circuits for Grasping: Spinal DI3 Interneurons Mediate Cutaneous Control of Motor Behavior." *Neuron* 78 (1): 191–204. https://doi.org/10.1016/j.neuron.2013.02.007.
Caggiano, V, R Leiras, H Goñi-Erro, D Masini, C Bellardita, J Bouvier, V Caldeira, G Fisone, and O Kiehn. 2018. "Midbrain Circuits That Set Locomotor Speed and Gait Selection." *Nature* 553 (7689): 455–60. https://doi.org/10.1038/nature25448.
Callahan, Rebecca A, Richard Roberts, Mohini Sengupta, Yukiko Kimura, Shin-ichi Higashijima, and Martha W Bagnall. 2019. "Spinal V2b Neurons Reveal a Role for Ipsilateral Inhibition in Speed Control." Edited by Ronald L Calabrese, Claire Wyart, Claire Wyart, and Marco Beato. *ELife* 8 (July): e47837. https://doi.org/10.7554/eLife.47837.
Capelli, Paolo, Chiara Pivetta, Maria Soledad Esposito, and Silvia Arber. 2017. "Locomotor Speed Control Circuits in the Caudal Brainstem." *Nature* 551 (7680): 373–77. https://doi.org/10.1038/nature24064.
Chehrehasa, Fatemah, Adrian C. B. Meedeniya, Patrick Dwyer, Greger Abrahamsen, and Alan Mackay-Sim. 2009. "EdU, a New Thymidine Analogue for Labelling Proliferating Cells in the Nervous System." *Journal of Neuroscience Methods* 177 (1): 122–30. https://doi.org/10.1016/j.jneumeth.2008.10.006.
Clarke, K. A., and J. Still. 1999. "Gait Analysis in the Mouse." *Physiology & Behavior* 66 (5): 723–29. https://doi.org/10.1016/s0031-9384(98)00343-6.
Conway, B. A., H. Hultborn, and O. Kiehn. 1987. "Proprioceptive Input Resets Central Locomotor Rhythm in the Spinal Cat." *Experimental Brain Research* 68 (3): 643–56. https://doi.org/10.1007/BF00249807.
Coulon, Patrice, Hélène Bras, and Laurent Vinay. 2011. "Characterization of Last-Order Premotor Interneurons by Transneuronal Tracing with Rabies Virus in the Neonatal Mouse Spinal Cord." *The Journal of*

Comparative Neurology 519 (17): 3470–87. https://doi.org/10.1002/cne.22717.
Crone, Steven A., Katharina A. Quinlan, Laskaro Zagoraiou, Steven Droho, Carlos Ernesto Restrepo, Line Lundfald, Toshiaki Endo, et al. 2008. "Genetic Ablation of V2a Ipsilateral Interneurons Disrupts Left-Right Locomotor Coordination in Mammalian Spinal Cord." *Neuron* 60 (1): 70–83. https://doi.org/10.1016/j.neuron.2008.08.009.
Danner, Simon M., Simon D. Wilshin, Natalia A. Shevtsova, and Ilya A. Rybak. 2016. "Central Control of Interlimb Coordination and Speed-Dependent Gait Expression in Quadrupeds." *The Journal of Physiology* 594 (23): 6947–67. https://doi.org/10.1113/JP272787.
Derjean, Dominique, Sandrine Bertrand, Gwendal Le Masson, Marc Landry, Valérie Morisset, and Frédéric Nagy. 2003. "Dynamic Balance of Metabotropic Inputs Causes Dorsal Horn Neurons to Switch Functional States." *Nature Neuroscience* 6 (3): 274–81. https://doi.org/10.1038/nn1016.
Dubin, Adrienne E., and Ardem Patapoutian. 2010. "Nociceptors: The Sensors of the Pain Pathway." *The Journal of Clinical Investigation* 120 (11): 3760–72. https://doi.org/10.1172/JCI42843.
Duysens, J. 1977. "Reflex Control of Locomotion as Revealed by Stimulation of Cutaneous Afferents in Spontaneously Walking Premammillary Cats." *Journal of Neurophysiology* 40 (4): 737–51. https://doi.org/10.1152/jn.1977.40.4.737.
Edgley, S. A., and E. Jankowska. 1987a. "Field Potentials Generated by Group II Muscle Afferents in the Middle Lumbar Segments of the Cat Spinal Cord." *The Journal of Physiology* 385 (April): 393–413. https://doi.org/10.1113/jphysiol.1987.sp016498.
Edgley, S A, and E Jankowska. 1987b. "An Interneuronal Relay for Group I and II Muscle Afferents in the Midlumbar Segments of the Cat Spinal Cord." *The Journal of Physiology* 389 (August): 647–74.
Forssberg, H. 1979. "Stumbling Corrective Reaction: A Phase-Dependent Compensatory Reaction during Locomotion." *Journal of Neurophysiology* 42 (4): 936–53. https://doi.org/10.1152/jn.1979.42.4.936.
Forssberg, H., S. Grillner, and S. Rossignol. 1975. "Phase Dependent Reflex Reversal during Walking in Chronic Spinal Cats." *Brain Research* 85 (1): 103–7. https://doi.org/10.1016/0006-8993(75)91013-6.
Frigon, Alain, Étienne Desrochers, Yann Thibaudier, Marie-France Hurteau, and Charline Dambreville. 2017. "Left-Right Coordination from Simple to Extreme Conditions during Split-Belt Locomotion in the Chronic Spinal Adult Cat." *The Journal of Physiology* 595 (1): 341–61. https://doi.org/10.1113/JP272740.
Frigon, Alain, Jennifer Sirois, and Jean-Pierre Gossard. 2010. "Effects of Ankle and Hip Muscle Afferent Inputs on Rhythm Generation during Fictive Locomotion." *Journal of Neurophysiology* 103 (3): 1591–1605. https://doi.org/10.1152/jn.01028.2009.
Gatto, Graziana, Steeve Bourane, Xiangyu Ren, Stefania Di Costanzo, Peter K. Fenton, Priyabrata Halder, Rebecca P. Seal, and Martyn D. Goulding. 2021. "A Functional Topographic Map for Spinal Sensorimotor Reflexes." *Neuron* 109 (1): 91-104.e5. https://doi.org/10.1016/j.neuron.2020.10.003.
Goldberger, M. E. 1977. "Locomotor Recovery after Unilateral Hindlimb Deafferentation in Cats." *Brain Research* 123 (1): 59–74. https://doi.org/10.1016/0006-8993(77)90643-6.
Gosgnach, Simon, Guillermo M. Lanuza, Simon J. B. Butt, Harald Saueressig, Ying Zhang, Tomoko Velasquez, Dieter Riethmacher, Edward M. Callaway, Ole Kiehn, and Martyn Goulding. 2006. "V1 Spinal Neurons Regulate the Speed of Vertebrate Locomotor Outputs." *Nature* 440 (7081): 215–19. https://doi.org/10.1038/nature04545.
Goslow Jr., George E., Robert M. Reinking, and Douglas G. Stuart. 1973. "The Cat Step Cycle: Hind Limb Joint Angles and Muscle Lengths during Unrestrained Locomotion." *Journal of Morphology* 141 (1): 1–41. https://doi.org/10.1002/jmor.1051410102.
Gradwell, Mark A., and Victoria E. Abraira. 2021. "Sensory Symphonies: How Excitatory Spinal Cord Modules Orchestrate Behavior." *Neuron* 109 (1): 3–5. https://doi.org/10.1016/j.neuron.2020.12.012.
Gradwell, Mark A., Kieran A. Boyle, Tyler J. Browne, Andrew M. Bell, Jacklyn Leonardo, Fernanda S. Peralta Reyes, Allen C. Dickie, et al. 2022. "Diversity of Inhibitory and Excitatory Parvalbumin Interneuron Circuits in the Dorsal Horn." *Pain* 163 (3): e432–52. https://doi.org/10.1097/j.pain.0000000000002422.
Grillner, S., and S. Rossignol. 1978. "On the Initiation of the Swing Phase of Locomotion in Chronic Spinal Cats." *Brain Research* 146 (2): 269–77. https://doi.org/10.1016/0006-8993(78)90973-3.
Gross, Michael K., Mirella Dottori, and Martyn Goulding. 2002. "Lbx1 Specifies Somatosensory Association Interneurons in the Dorsal Spinal Cord." *Neuron* 34 (4): 535–49. https://doi.org/10.1016/S0896-6273(02)00690-6.

Grudt, T J, and E R Perl. 2002. “Correlations between Neuronal Morphology and Electrophysiological Features in the Rodent Superficial Dorsal Horn.” *The Journal of Physiology* 540 (Pt 1): 189–207. https://doi.org/10.1113/jphysiol.2001.012890.

Gruner, J. A., and J. Altman. 1980. “Swimming in the Rat: Analysis of Locomotor Performance in Comparison to Stepping.” *Experimental Brain Research* 40 (4): 374–82. https://doi.org/10.1007/BF00236146.

Gruters, Kurtis G., and Jennifer M. Groh. 2012. “Sounds and beyond: Multisensory and Other Non-Auditory Signals in the Inferior Colliculus.” *Frontiers in Neural Circuits* 6 (December): 96. https://doi.org/10.3389/fncir.2012.00096.

Guertin, P, M J Angel, M C Perreault, and D A McCrea. 1995. “Ankle Extensor Group I Afferents Excite Extensors throughout the Hindlimb during Fictive Locomotion in the Cat.” *The Journal of Physiology* 487 (Pt 1): 197–209.

Halbertsma, J. M. 1983. “The Stride Cycle of the Cat: The Modelling of Locomotion by Computerized Analysis of Automatic Recordings.” *Acta Physiologica Scandinavica. Supplementum* 521: 1–75.

Hammar, Ingela, B. Anne Bannatyne, David J. Maxwell, Stephen A. Edgley, and Elzbieta Jankowska. 2004. “The Actions of Monoamines and Distribution of Noradrenergic and Serotoninergic Contacts on Different Subpopulations of Commissural Interneurons in the Cat Spinal Cord.” *The European Journal of Neuroscience* 19 (5): 1305–16. https://doi.org/10.1111/j.1460-9568.2004.03239.x.

Hampton, Thomas G., Melissa R. Stasko, Ajit Kale, Ivo Amende, and Alberto C. S. Costa. 2004. “Gait Dynamics in Trisomic Mice: Quantitative Neurological Traits of Down Syndrome.” *Physiology & Behavior* 82 (2–3): 381–89. https://doi.org/10.1016/j.physbeh.2004.04.006.

Herbin, Marc, Jean-Pierre Gasc, and Sabine Renous. 2004. “Symmetrical and Asymmetrical Gaits in the Mouse: Patterns to Increase Velocity.” *Journal of Comparative Physiology. A, Neuroethology, Sensory, Neural, and Behavioral Physiology* 190 (11): 895–906. https://doi.org/10.1007/s00359-004-0545-0.

Hiebert, G. W., and K. G. Pearson. 1999. “Contribution of Sensory Feedback to the Generation of Extensor Activity during Walking in the Decerebrate Cat.” *Journal of Neurophysiology* 81 (2): 758–70. https://doi.org/10.1152/jn.1999.81.2.758.

Hiebert, G. W., P. J. Whelan, A. Prochazka, and K. G. Pearson. 1996. “Contribution of Hind Limb Flexor Muscle Afferents to the Timing of Phase Transitions in the Cat Step Cycle.” *Journal of Neurophysiology* 75 (3): 1126–37. https://doi.org/10.1152/jn.1996.75.3.1126.

Hilde, Kathryn L., Ariel J. Levine, Christopher A. Hinckley, Marito Hayashi, Jessica M. Montgomery, Miriam Gullo, Shawn P. Driscoll, et al. 2016. “Satb2 Is Required for the Development of a Spinal Exteroceptive Microcircuit That Modulates Limb Position.” *Neuron* 91 (4): 763–76. https://doi.org/10.1016/j.neuron.2016.07.014.

Hongo, T., S. Kitazawa, Y. Ohki, and M. Xi. 1989. “Functional Identification of Last-Order Interneurones of Skin Reflex Pathways in the Cat Forelimb Segments.” *Brain Research*, December. https://www.meta.org/papers/functional-identification-of-last-order/2611673.

Hunt, Stephen P., Adrian Pini, and Gerard Evan. 1987. “Induction of C-Fos-like Protein in Spinal Cord Neurons Following Sensory Stimulation.” *Nature* 328 (6131): 632–34. https://doi.org/10.1038/328632a0.

Ishizuka, N., H. Mannen, T. Hongo, and S. Sasaki. 1979. “Trajectory of Group Ia Afferent Fibers Stained with Horseradish Peroxidase in the Lumbosacral Spinal Cord of the Cat: Three Dimensional Reconstructions from Serial Sections.” *The Journal of Comparative Neurology* 186 (2): 189–211. https://doi.org/10.1002/cne.901860206.

Ito, Tetsufumi, Deborah C. Bishop, and Douglas L. Oliver. 2016. “Functional Organization of the Local Circuit in the Inferior Colliculus.” *Anatomical Science International* 91 (1): 22–34. https://doi.org/10.1007/s12565-015-0308-8.

J, Duysens, and Pearson Kg. 1980. “Inhibition of Flexor Burst Generation by Loading Ankle Extensor Muscles in Walking Cats.” *Brain Research* 187 (2). https://doi.org/10.1016/0006-8993(80)90206-1.

Jankowska, E., E. Bichler, and I. Hammar. 2000. “Areas of Operation of Interneurons Mediating Presynaptic Inhibition in Sacral Spinal Segments.” *Experimental Brain Research* 133 (3): 402–6. https://doi.org/10.1007/s002210000429.

Jankowska, E., I. Hammar, B. Chojnicka, and C. H. Hedén. 2000. “Effects of Monoamines on Interneurons in Four Spinal Reflex Pathways from Group I and/or Group II Muscle Afferents.” *The European Journal of Neuroscience* 12 (2): 701–14. https://doi.org/10.1046/j.1460-9568.2000.00955.x.

Jankowska, E., D. J. Maxwell, and B. A. Bannatyne. 2007. “On Coupling and Decoupling of Spinal Interneuronal Networks.” *Archives Italiennes De Biologie* 145 (3–4): 235–50.
Jankowska, E., U. Slawinska, and I. Hammar. 2002. “On Organization of a Neuronal Network in Pathways from Group II Muscle Afferents in Feline Lumbar Spinal Segments.” *The Journal of Physiology* 542 (Pt 1): 301–14. https://doi.org/10.1113/jphysiol.2001.014076.
Jeanne, James M., and Rachel I. Wilson. 2015. “Convergence, Divergence, and Reconvergence in a Feedforward Network Improves Neural Speed and Accuracy.” *Neuron* 88 (5): 1014–26. https://doi.org/10.1016/j.neuron.2015.10.018.
Jiang, Z., K. P. Carlin, and R. M. Brownstone. 1999. “An in Vitro Functionally Mature Mouse Spinal Cord Preparation for the Study of Spinal Motor Networks.” *Brain Research* 816 (2): 493–99. https://doi.org/10.1016/s0006-8993(98)01199-8.
Johnson, Michael D., Allison S. Hyngstrom, Marin Manuel, and C. J. Heckman. 2012. “Push-Pull Control of Motor Output.” *The Journal of Neuroscience: The Official Journal of the Society for Neuroscience* 32 (13): 4592–99. https://doi.org/10.1523/JNEUROSCI.4709-11.2012.
Kempter, R., W. Gerstner, and J. L. van Hemmen. 1998. “How the Threshold of a Neuron Determines Its Capacity for Coincidence Detection.” *Bio Systems* 48 (1–3): 105–12. https://doi.org/10.1016/s0303-2647(98)00055-0.
Kiehn, Ole. 2016. “Decoding the Organization of Spinal Circuits That Control Locomotion.” *Nature Reviews Neuroscience* 17 (4): 224–38. https://doi.org/10.1038/nrn.2016.9.
Kim, Hoseok, Sofie Ährlund-Richter, Xinming Wang, Karl Deisseroth, and Marie Carlén. 2016. “Prefrontal Parvalbumin Neurons in Control of Attention.” *Cell* 164 (1–2): 208–18. https://doi.org/10.1016/j.cell.2015.11.038.
Kim, Sung Soo, Manuel Gomez-Ramirez, Pramodsingh H. Thakur, and Steven S. Hsiao. 2015. “Multimodal Interactions between Proprioceptive and Cutaneous Signals in Primary Somatosensory Cortex.” *Neuron* 86 (2): 555–66. https://doi.org/10.1016/j.neuron.2015.03.020.
Kniffki, K. D., E. D. Schomburg, and H. Steffens. 1981. “Convergence in Segmental Reflex Pathways from Fine Muscle Afferents and Cutaneous or Group II Muscle Afferents to Alpha-Motoneurones.” *Brain Research* 218 (1–2): 342–46. https://doi.org/10.1016/0006-8993(81)91312-3.
Koch, Stephanie C. 2019. “Motor Task-Selective Spinal Sensorimotor Interneurons in Mammalian Circuits.” *Current Opinion in Physiology*, Motor Control Systems, 8 (April): 129–35. https://doi.org/10.1016/j.cophys.2019.01.014.
Koch, Stephanie C., Marta Garcia Del Barrio, Antoine Dalet, Graziana Gatto, Thomas Günther, Jingming Zhang, Barbara Seidler, Dieter Saur, Roland Schüle, and Martyn Goulding. 2017. “RORβ Spinal Interneurons Gate Sensory Transmission during Locomotion to Secure a Fluid Walking Gait.” *Neuron* 96 (6): 1419-1431.e5. https://doi.org/10.1016/j.neuron.2017.11.011.
Kriellaars, D. J., R. M. Brownstone, B. R. Noga, and L. M. Jordan. 1994. “Mechanical Entrainment of Fictive Locomotion in the Decerebrate Cat.” *Journal of Neurophysiology* 71 (6): 2074–86. https://doi.org/10.1152/jn.1994.71.6.2074.
Laflamme, Olivier D., and Turgay Akay. 2018. “Excitatory and Inhibitory Crossed Reflex Pathways in Mice.” *Journal of Neurophysiology* 120 (6): 2897–2907. https://doi.org/10.1152/jn.00450.2018.
Laflamme, Olivier D., Marwan Ibrahim, and Turgay Akay. 2022. “Crossed Reflex Responses to Flexor Nerve Stimulation in Mice.” *Journal of Neurophysiology* 127 (2): 493–503. https://doi.org/10.1152/jn.00385.2021.
Lajoie, Y., N. Teasdale, J. D. Cole, M. Burnett, C. Bard, M. Fleury, R. Forget, J. Paillard, and Y. Lamarre. 1996. “Gait of a Deafferented Subject without Large Myelinated Sensory Fibers below the Neck.” *Neurology* 47 (1): 109–15. https://doi.org/10.1212/wnl.47.1.109.
Le Franc, Yann, and Gwendal Le Masson. 2010. “Multiple Firing Patterns in Deep Dorsal Horn Neurons of the Spinal Cord: Computational Analysis of Mechanisms and Functional Implications.” *Journal of Neurophysiology* 104 (4): 1978–96. https://doi.org/10.1152/jn.00919.2009.
Lehnert, Brendan P., Celine Santiago, Erica L. Huey, Alan J. Emanuel, Sophia Renauld, Nusrat Africawala, Ilayda Alkislar, et al. 2021. “Mechanoreceptor Synapses in the Brainstem Shape the Central Representation of Touch.” *Cell* 184 (22): 5608-5621.e18. https://doi.org/10.1016/j.cell.2021.09.023.
Lemieux, Maxime, Nicolas Josset, Marie Roussel, Sébastien Couraud, and Frédéric Bretzner. 2016.

"Speed-Dependent Modulation of the Locomotor Behavior in Adult Mice Reveals Attractor and Transitional Gaits." *Frontiers in Neuroscience* 10: 42. https://doi.org/10.3389/fnins.2016.00042.

Levine, Ariel J., Christopher A. Hinckley, Kathryn L. Hilde, Shawn P. Driscoll, Tiffany H. Poon, Jessica M. Montgomery, and Samuel L. Pfaff. 2014. "Identification of a Cellular Node for Motor Control Pathways." *Nature Neuroscience* 17 (4): 586–93. https://doi.org/10.1038/nn.3675.

Levinsson, Anders, Hans Holmberg, Jonas Broman, Mengliang Zhang, and Jens Schouenborg. 2002. "Spinal Sensorimotor Transformation: Relation between Cutaneous Somatotopy and a Reflex Network." *The Journal of Neuroscience: The Official Journal of the Society for Neuroscience* 22 (18): 8170–82.

Li, Dongxiao, Yundu Li, Yunyun Tian, Zuoshang Xu, and Yansu Guo. 2019. "Direct Intrathecal Injection of Recombinant Adeno-Associated Viruses in Adult Mice." *JoVE (Journal of Visualized Experiments)*, no. 144 (February): e58565. https://doi.org/10.3791/58565.

Liang, Huazheng, George Paxinos, and Charles Watson. 2012. "The Red Nucleus and the Rubrospinal Projection in the Mouse." *Brain Structure & Function* 217 (2): 221–32. https://doi.org/10.1007/s00429-011-0348-3.

Lu, Daniel C., Tianyi Niu, and William A. Alaynick. 2015. "Molecular and Cellular Development of Spinal Cord Locomotor Circuitry." *Frontiers in Molecular Neuroscience* 8 (June): 25. https://doi.org/10.3389/fnmol.2015.00025.

Lundberg, A., K. Malmgren, and E. D. Schomburg. 1977. "Cutaneous Facilitation of Transmission in Reflex Pathways from Ib Afferents to Motoneurones." *The Journal of Physiology* 265 (3): 763–80. https://doi.org/10.1113/jphysiol.1977.sp011742.

Luo, Wenqin, Hideki Enomoto, Frank L. Rice, Jeffrey Milbrandt, and David D. Ginty. 2009. "Molecular Identification of Rapidly Adapting Mechanoreceptors and Their Developmental Dependence on Ret Signaling." *Neuron* 64 (6): 841–56. https://doi.org/10.1016/j.neuron.2009.11.003.

Martin, J. H. 1996. "Differential Spinal Projections from the Forelimb Areas of the Rostral and Caudal Subregions of Primary Motor Cortex in the Cat." *Experimental Brain Research* 108 (2): 191–205. https://doi.org/10.1007/BF00228094.

Martinez, Luis M., and Jose-Manuel Alonso. 2003. "Complex Receptive Fields in Primary Visual Cortex." *The Neuroscientist: A Review Journal Bringing Neurobiology, Neurology and Psychiatry* 9 (5): 317–31. https://doi.org/10.1177/1073858403252732.

Mathis, Alexander, Pranav Mamidanna, Kevin M. Cury, Taiga Abe, Venkatesh N. Murthy, Mackenzie Weygandt Mathis, and Matthias Bethge. 2018. "DeepLabCut: Markerless Pose Estimation of User-Defined Body Parts with Deep Learning." *Nature Neuroscience* 21 (9): 1281–89. https://doi.org/10.1038/s41593-018-0209-y.

Mayer, William P., Andrew J. Murray, Susan Brenner-Morton, Thomas M. Jessell, Warren G. Tourtellotte, and Turgay Akay. 2018. "Role of Muscle Spindle Feedback in Regulating Muscle Activity Strength during Walking at Different Speed in Mice." *Journal of Neurophysiology* 120 (5): 2484–97. https://doi.org/10.1152/jn.00250.2018.

Mayer, William Paganini, and Turgay Akay. 2018. "Stumbling Corrective Reaction Elicited by Mechanical and Electrical Stimulation of the Saphenous Nerve in Walking Mice." *The Journal of Experimental Biology* 221 (Pt 13): jeb178095. https://doi.org/10.1242/jeb.178095.

McCrea, D. A. 1998. "Neuronal Basis of Afferent-Evoked Enhancement of Locomotor Activity." *Annals of the New York Academy of Sciences* 860 (November): 216–25. https://doi.org/10.1111/j.1749-6632.1998.tb09051.x.

Miranda, Camila Oliveira, Krisztina Hegedüs, Hendrik Wildner, Hanns Ulrich Zeilhofer, and Miklós Antal. 2022. "Morphological and Neurochemical Characterization of Glycinergic Neurons in Laminae I-IV of the Mouse Spinal Dorsal Horn." *The Journal of Comparative Neurology* 530 (3): 607–26. https://doi.org/10.1002/cne.25232.

Morgan, James I., and Tom Curran. 1986. "Role of Ion Flux in the Control of C-Fos Expression." *Nature* 322 (6079): 552–55. https://doi.org/10.1038/322552a0.

Moschovakis, A. K., M. Solodkin, and R. E. Burke. 1992. "Anatomical and Physiological Study of Interneurons in an Oligosynaptic Cutaneous Reflex Pathway in the Cat Hindlimb." *Brain Research* 586 (2): 311–18. https://doi.org/10.1016/0006-8993(92)91641-q.

Muir, G. D., and J. D. Steeves. 1995. "Phasic Cutaneous Input Facilitates Locomotor Recovery after

Incomplete Spinal Injury in the Chick." *Journal of Neurophysiology* 74 (1): 358–68. https://doi.org/10.1152/jn.1995.74.1.358.

Nahar, Lailun, Blake M. Delacroix, and Hyung W. Nam. 2021. "The Role of Parvalbumin Interneurons in Neurotransmitter Balance and Neurological Disease." *Frontiers in Psychiatry* 12. https://www.frontiersin.org/article/10.3389/fpsyt.2021.679960.

Orlovsky, Grigori, T. G. Deliagina, and Sten Grillner. 1999. *Neuronal Control of Locomotion: From Mollusc to Man*. https://doi.org/10.1093/acprof:oso/9780198524052.001.0001.

Pearson, K. G., H. Acharya, and K. Fouad. 2005. "A New Electrode Configuration for Recording Electromyographic Activity in Behaving Mice." *Journal of Neuroscience Methods* 148 (1): 36–42. https://doi.org/10.1016/j.jneumeth.2005.04.006.

Pearson, K. G., J. E. Misiaszek, and K. Fouad. 1998. "Enhancement and Resetting of Locomotor Activity by Muscle Afferents." *Annals of the New York Academy of Sciences* 860 (November): 203–15. https://doi.org/10.1111/j.1749-6632.1998.tb09050.x.

Pearson, K. G., J. M. Ramirez, and W. Jiang. 1992. "Entrainment of the Locomotor Rhythm by Group Ib Afferents from Ankle Extensor Muscles in Spinal Cats." *Experimental Brain Research* 90 (3): 557–66. https://doi.org/10.1007/BF00230939.

Pierrot-Deseilligny, E., C. Bergego, R. Katz, and C. Morin. 1981. "Cutaneous Depression of Ib Reflex Pathways to Motoneurones in Man." *Experimental Brain Research* 42 (3–4): 351–61. https://doi.org/10.1007/BF00237500.

Prescott, Steven A., and Yves De Koninck. 2002. "Four Cell Types with Distinctive Membrane Properties and Morphologies in Lamina I of the Spinal Dorsal Horn of the Adult Rat." *The Journal of Physiology* 539 (Pt 3): 817. https://doi.org/10.1113/jphysiol.2001.013437.

Prochazka, Arthur, and Sergiy Yakovenko. 2007. "The Neuromechanical Tuning Hypothesis." *Progress in Brain Research* 165: 255–65. https://doi.org/10.1016/S0079-6123(06)65016-4.

Punnakkal, Pradeep, Carolin von Schoultz, Karen Haenraets, Hendrik Wildner, and Hanns Ulrich Zeilhofer. 2014. "Morphological, Biophysical and Synaptic Properties of Glutamatergic Neurons of the Mouse Spinal Dorsal Horn." *The Journal of Physiology* 592 (4): 759–76. https://doi.org/10.1113/jphysiol.2013.264937.

Puskár, Z., and M. Antal. 1997. "Localization of Last-Order Premotor Interneurons in the Lumbar Spinal Cord of Rats." *The Journal of Comparative Neurology* 389 (3): 377–89. https://doi.org/10.1002/(sici)1096-9861(19971222)389:3<377::aid-cne2>3.0.co;2-y.

Ringach, Dario L. 2004. "Mapping Receptive Fields in Primary Visual Cortex." *The Journal of Physiology* 558 (Pt 3): 717–28. https://doi.org/10.1113/jphysiol.2004.065771.

Roseberry, Thomas K., A. Moses Lee, Arnaud L. Lalive, Linda Wilbrecht, Antonello Bonci, and Anatol C. Kreitzer. 2016. "Cell-Type-Specific Control of Brainstem Locomotor Circuits by Basal Ganglia." *Cell* 164 (3): 526–37. https://doi.org/10.1016/j.cell.2015.12.037.

Russ, Daniel E., Ryan B. Patterson Cross, Li Li, Stephanie C. Koch, Kaya J. E. Matson, Archana Yadav, Mor R. Alkaslasi, et al. 2021. "A Harmonized Atlas of Mouse Spinal Cord Cell Types and Their Spatial Organization." *Nature Communications* 12 (1): 5722. https://doi.org/10.1038/s41467-021-25125-1.

Rutlin, Michael, Cheng-Ying Ho, Victoria E. Abraira, Colleen Cassidy, Ling Bai, C. Jeffery Woodbury, and David D. Ginty. 2014. "The Cellular and Molecular Basis of Direction Selectivity of Aδ-LTMRs." *Cell* 159 (7): 1640–51. https://doi.org/10.1016/j.cell.2014.11.038.

Rybak, Ilya A., Natalia A. Shevtsova, Myriam Lafreniere-Roula, and David A. McCrea. 2006. "Modelling Spinal Circuitry Involved in Locomotor Pattern Generation: Insights from Deletions during Fictive Locomotion." *The Journal of Physiology* 577 (Pt 2): 617–39. https://doi.org/10.1113/jphysiol.2006.118703.

Saltiel, P., M. C. Tresch, and E. Bizzi. 1998. "Spinal Cord Modular Organization and Rhythm Generation: An NMDA Iontophoretic Study in the Frog." *Journal of Neurophysiology* 80 (5): 2323–39. https://doi.org/10.1152/jn.1998.80.5.2323.

Sathyamurthy, Anupama, Kory R. Johnson, Kaya J. E. Matson, Courtney I. Dobrott, Li Li, Anna R. Ryba, Tzipporah B. Bergman, Michael C. Kelly, Matthew W. Kelley, and Ariel J. Levine. 2018. "Massively Parallel Single Nucleus Transcriptional Profiling Defines Spinal Cord Neurons and Their Activity during Behavior." *Cell Reports* 22 (8): 2216–25. https://doi.org/10.1016/j.celrep.2018.02.003.

Schillings, A. M., B. M. Van Wezel, and J. Duysens. 1996. "Mechanically Induced Stumbling during Human

Treadmill Walking." *Journal of Neuroscience Methods* 67 (1): 11–17. https://doi.org/10.1016/0165-0270(95)00149-2.
Schomburg, E. D., N. Petersen, I. Barajon, and H. Hultborn. 1998a. "Flexor Reflex Afferents Reset the Step Cycle during Fictive Locomotion in the Cat." *Experimental Brain Research* 122 (3): 339–50. https://doi.org/10.1007/s002210050522.
———. 1998b. "Flexor Reflex Afferents Reset the Step Cycle during Fictive Locomotion in the Cat." *Experimental Brain Research* 122 (3): 339–50. https://doi.org/10.1007/s002210050522.
Schouenborg, J., H. R. Weng, J. Kalliomäki, and H. Holmberg. 1995. "A Survey of Spinal Dorsal Horn Neurones Encoding the Spatial Organization of Withdrawal Reflexes in the Rat." *Experimental Brain Research* 106 (1): 19–27. https://doi.org/10.1007/BF00241353.
Sherrington, C. S. 1910. "Flexion-Reflex of the Limb, Crossed Extension-Reflex, and Reflex Stepping and Standing." *The Journal of Physiology* 40 (1–2): 28–121. https://doi.org/10.1113/jphysiol.1910.sp001362.
Sherrington, Charles Scott. 1906. *The Integrative Action of the Nervous System*.
Sherrington, CS. 1910. "Remarks on the Reflex Mechanism of the Step" Brain 33: 1–25.
Sholl, D. A. 1953. "Dendritic Organization in the Neurons of the Visual and Motor Cortices of the Cat." *Journal of Anatomy* 87 (Pt 4): 387-406.1.
Sieber, Martin A., Robert Storm, Margaret Martinez-de-la-Torre, Thomas Müller, Hagen Wende, Katja Reuter, Elena Vasyutina, and Carmen Birchmeier. 2007. "Lbx1 Acts as a Selector Gene in the Fate Determination of Somatosensory and Viscerosensory Relay Neurons in the Hindbrain." *Journal of Neuroscience* 27 (18): 4902–9. https://doi.org/10.1523/JNEUROSCI.0717-07.2007.
Spillmann, Lothar. 2014. "Receptive Fields of Visual Neurons: The Early Years." *Perception* 43 (11): 1145–76. https://doi.org/10.1068/p7721.
Stecina, Katinka, Jorge Quevedo, and David A. McCrea. 2005. "Parallel Reflex Pathways from Flexor Muscle Afferents Evoking Resetting and Flexion Enhancement during Fictive Locomotion and Scratch in the Cat." *The Journal of Physiology* 569 (Pt 1): 275–90. https://doi.org/10.1113/jphysiol.2005.095505.
Stein, B. E., and M. A. Meredith. 1990. "Multisensory Integration. Neural and Behavioral Solutions for Dealing with Stimuli from Different Sensory Modalities." *Annals of the New York Academy of Sciences* 608: 51–65; discussion 65-70. https://doi.org/10.1111/j.1749-6632.1990.tb48891.x.
Stepien, Anna E., Marco Tripodi, and Silvia Arber. 2010. "Monosynaptic Rabies Virus Reveals Premotor Network Organization and Synaptic Specificity of Cholinergic Partition Cells." *Neuron* 68 (3): 456–72. https://doi.org/10.1016/j.neuron.2010.10.019.
Talpalar, Adolfo E., Julien Bouvier, Lotta Borgius, Gilles Fortin, Alessandra Pierani, and Ole Kiehn. 2013. "Dual-Mode Operation of Neuronal Networks Involved in Left-Right Alternation." *Nature* 500 (7460): 85–88. https://doi.org/10.1038/nature12286.
Tamamaki, Nobuaki, Yuchio Yanagawa, Ryohei Tomioka, Jun-Ichi Miyazaki, Kunihiko Obata, and Takeshi Kaneko. 2003. "Green Fluorescent Protein Expression and Colocalization with Calretinin, Parvalbumin, and Somatostatin in the GAD67-GFP Knock-in Mouse." *The Journal of Comparative Neurology* 467 (1): 60–79. https://doi.org/10.1002/cne.10905.
Tresch, M. C., and E. Bizzi. 1999. "Responses to Spinal Microstimulation in the Chronically Spinalized Rat and Their Relationship to Spinal Systems Activated by Low Threshold Cutaneous Stimulation." *Experimental Brain Research* 129 (3): 401–16. https://doi.org/10.1007/s002210050908.
Tripodi, Marco, Anna E. Stepien, and Silvia Arber. 2011. "Motor Antagonism Exposed by Spatial Segregation and Timing of Neurogenesis." *Nature* 479 (7371): 61–66. https://doi.org/10.1038/nature10538.
Tuthill, John C., and Eiman Azim. 2018. "Proprioception." *Current Biology* 28 (5): R194–203. https://doi.org/10.1016/j.cub.2018.01.064.
Wetzel, M. C., A. E. Atwater, J. V. Wait, and D. G. Stuart. 1976. "Kinematics of Locomotion by Cats with a Single Hindlimb Deafferented." *Journal of Neurophysiology* 39 (4): 667–78. https://doi.org/10.1152/jn.1976.39.4.667.
Whelan, P. J., G. W. Hiebert, and K. G. Pearson. 1995. "Stimulation of the Group I Extensor Afferents Prolongs the Stance Phase in Walking Cats." *Experimental Brain Research* 103 (1): 20–30. https://doi.org/10.1007/BF00241961.
Wilson, Jennifer M., Robert Hartley, David J. Maxwell, Andrew J. Todd, Ivo Lieberam, Julia A. Kaltschmidt, Yutaka Yoshida, Thomas M. Jessell, and Robert M. Brownstone. 2005. "Conditional Rhythmicity of

Ventral Spinal Interneurons Defined by Expression of the Hb9 Homeodomain Protein." *Journal of Neuroscience* 25 (24): 5710–19. https://doi.org/10.1523/JNEUROSCI.0274-05.2005.
Zhang, Han, Natalia A. Shevtsova, Dylan Deska-Gauthier, Colin Mackay, Kimberly J. Dougherty, Simon M. Danner, Ying Zhang, and Ilya A. Rybak. 2022. "The Role of V3 Neurons in Speed-Dependent Interlimb Coordination during Locomotion in Mice." *ELife* 11 (April): e73424. https://doi.org/10.7554/eLife.73424.
Zhang, Jingming, Guillermo M. Lanuza, Olivier Britz, Zhi Wang, Valerie C. Siembab, Ying Zhang, Tomoko Velasquez, Francisco J. Alvarez, Eric Frank, and Martyn Goulding. 2014. "V1 and V2b Interneurons Secure the Alternating Flexor-Extensor Motor Activity Mice Require for Limbed Locomotion." *Neuron* 82 (1): 138–50. https://doi.org/10.1016/j.neuron.2014.02.013.
Zheng, Yang, Pin Liu, Ling Bai, James S. Trimmer, Bruce P. Bean, and David D. Ginty. 2019. "Deep Sequencing of Somatosensory Neurons Reveals Molecular Determinants of Intrinsic Physiological Properties." *Neuron* 103 (4): 598-616.e7. https://doi.org/10.1016/j.neuron.2019.05.039.

ACKNOWLEDGEMENTS

We are grateful to …... Financial support was provided by ……..

AUTHOR CONTRIBUTIONS

N.E. performed….., M.G. performed…….. N.E. and M.G. prepared the figures with the contribution of all the authors. V.E.A conceived and supervised the study. V.E.A. wrote the paper with N.E. and M.G..…... All the authors contributed to its editing.

DECLARATION OF INTERESTS

The authors declare no competing interest.

DECLARATION of INCLUSION AND DIVERSITY

DECLARATION of STUDY DESIGN

STAR+METHODS

Key Resource table

Virus strains

Chemicals and peptides

Experimental mouse lines

Software and algorithms

LEAD CONTACT AND MATERIALS AVAILABILITY

Further information and requests for resources should be directed to and will be fulfilled by the Lead Contact, Victoria E. Abraira (victoria.abraira@rutgers.edu).

EXPERIMENTAL MODEL AND SUBJECT DETAILS

Mouse lines used to target DRG neuron populations include *TH*^{2aCreER} (Jax#025614), *vGlut3*^{iresCre} (Jax#028534), *TrkB*^{CreER} (Jax#027214), PTGFR^{CreER} (Zheng et al. 2019; Lehnert et al. 2021), *Ret*^{CreER} (Luo et al. 2009), Split^{Cre} (Rutlin et al. 2014), *Advillin*^{Cre} (Jax#032536), *Advillin*^{CreER} (Jax#032027) and *PV*^{2aCreER} (Jax#028580). Mouse

lines used to target spinal cord interneurons include *vGAT*^{irescre} (Jax#028862), *GAD2*^{Cherry} (Jax#023140), *GAD67*^{GFP} (Tamamaki et al. 2003), GlyT2^{GFP} (Miranda et al. 2022) , RoRβ^{FlpO} (Jax#029590), *RoRβ*^{CreER}*,Satb2*^{CreER} (Hilde et al. 2016), *vGlut2*^{iresCre}(Jax#016963), *islet1*^{iresCre} (Jax#024242), Sim1^{iresCre} (Jax#006395), *CCK*^{iresCre} (Jax#012706), vGluT2^{YFP} (Jax#017978), and *Lbx1*^{Cre} (Sieber et al. 2007). To target Parvalbumin interneurons we used PV^{Tdtomato} (Jax#027395) and PV^{FlpO} (Jax#022730) mouse-lines. For visualization, and manipulation of target populations the following mouse lines were used: *R26*$^{LSL\text{-}FSF\text{-}tdTomato}$ (Ai65, Jax#021875), *R26*$^{LSL\text{-}FSF\text{-}synaptophysin\text{-}GFP}$ (*RC::FPSit,* Jax#030206), R26$^{FSF\text{-}SynGFP}$ (derived from RC::FPSit), *R26*^{LSL}-synaptophysin-tdTomato (Ai34, Jax#012570), *R26*^{LSL}-tdTomato (Ai9, Jax#007909), *R26*^{LSL}-tdTomato (Ai14, Jax#007914),Tau$^{LSL\text{-}LacZ\text{-}FSF\text{-}DTR}$ (Bourane et al. 2015), *R26*$^{LSL\text{-}ChR2\text{-}YFP}$(Ai32, Jax#024109);*R26*$^{LSL\text{-}FSF\text{-}ChR2\text{-}YFP}$(Ai80, Jax#025109). ChAT^{eGFP} (Jax#007902) was used to target cholinergic interneurons and motor neurons , *Emx1*^{Cre} (Jax#005628) was used to target cortical neurons, and *Lbx1*^{Cre} (Acton et al. 2019) was used to identify dPVs genetic lineage and restrict PV expression to the deep dorsal horn. Transgenic mouse strains were used and maintained on a mixed genetic background (129/C57BL/6). Experimental animals used were of both sexes. With the exception of EMG recordings, housing, surgery, behavioral experiments and euthanasia were performed in compliance with Rutgers University Institutional Animal Care and Use Committee (IACUC; protocol #: 201702589). All mice used in experiments were housed in a regular light cycle room (lights on from 08:00 to 20:00) with food and water available ad libitum.
EMG recordings were performed at the lab of Dr. Turgay Akay (Dalhousie, Canada) according to the Canadian Council on Animal Care (CCAC) guidelines and approved by the local council on animal care of Dalhousie University. All mice used in experiments were housed in a regular light cycle room (lights on from 07:00 to 19:00) with food and water available ad libitum.

METHOD DETAILS

Genetic crosses and statistical methods related to individual figures:

Genetic crosses related to Figure 1: (B) Cutaneous and proprioceptive inputs labeled with *PV*^{2aCreER}*;Advillin*^{FlpO}*;Rosa*$^{LSL\text{-}FSF\text{-}Tomato}$*/Rosa*$^{FSF\text{-}SynGFP}$ (2 mg tamoxifen treatment at P21-P23). **(C)** Quantification of cutaneous and proprioceptive inputs across laminae was performed using 3 images from a *PV*^{2aCreER}*;Advillin*^{FlpO}*;Rosa*$^{LSL\text{-}FSF\text{-}Tomato}$*/Rosa*$^{FSF\text{-}SynGFP}$ (2 mg tamoxifen treatment at P21-P23) animal. **(E-F)** Density contour plots were generated using 9 images of 3 *vGAT*^{iresCre}*;Rosa*$^{LSL\text{-}Tomato}$ mice of each condition (rest, swim and walk). Density values for rest were subtracted from walk and swim. Plots of cfos (% of rest) were generated using 17-21 images of 4-5 *vGAT*^{iresCre}*;Rosa*$^{LSL\text{-}Tomato}$ mice for each condition. Cfos (% of rest) is increased in walk vs rest, Kruskal Wallis test with Dunn's correction for multiple comparisons, LIV-V_{medial} in walk vs rest, ***p = 0.0005; LIV-$V_{lateral}$ in walk vs rest, *p = 0.0177 ; and LVI-X in walk vs rest , *p = 0.0386.

Genetic crosses and statistical methods related to Figure 2: (A) Plot of cfos in excitatory and inhibitory interneurons as percentage of total c-fos in the medial deep dorsal horn was generated using 17-21 images of 4-5 *vGAT*^{iresCre}*;Rosa*$^{LSL\text{-}Tomato}$ mice for each condition. Cfos is increased in dPVs in walk vs rest, Mann-Whitney test, ** p = 0.0079. **(B)** oAP incidence calculated from 31 GAD67GFP+ and 34 GAD67GFP- neurons recorded from 4 *Advillin*^{CreER};*Rosa26*$^{LSL\text{-}ChR2(Ai32)}$;*GAD67*^{GFP} mice. **(C)** oEPSC amplitude calculated from 17 GAD67GFP+ and 14 GAD67GFP- neurons from 4 *Advillin*^{CreER};*Rosa26*$^{LSL\text{-}ChR2(Ai32)}$;*GAD67*^{GFP} mice, Mann-Whitney test, p = 0.6811. **(D-G)** For characterization of deep dorsal horn inhibitory and excitatory neurons spontaneous action potential (sAP) discharge we used 57 cells from 5 *vGAT*^{iresCre};*R26*$^{LSL\text{-}TdTomato}$ mice, and 32 cells from 5 *vGluT2*^{iresCre};*R26*$^{LSL\text{-}TdTomato}$ mice. **(E)** Inhibitory neurons show increased sAP incidence vs excitatory neurons, **(J)** increased sAP frequency, Mann-Whitney test, ****p < 0.0001, **(K)** and lower sAP coefficient of variation (CV), Mann-Whitney test, ***p = 0.0003. **(H-P)** For characterization of deep dorsal horn inhibitory and excitatory

neurons response to depolarizing current injection we used 86 cells from 5 *vGAT*^{iresCre};*R26*$^{LSL\text{-}TdTomato}$ mice, and 65 cells from 5 *vGluT*^{iresCre};*R26*$^{LSL\text{-}TdTomato}$ mice. **(I)** Inhibitory neurons show lower latency to 1st action potential, Mann-Whitney test, ***p = 0.0003, **(J)** and increased AP discharge in response to current injections, 2-way ANOVA, ****p < 0.0001, **(K)** and increased AP instantaneous frequency in response to current injections, 2-way ANOVA, ****p < 0.0001, (**L)** Representative threshold AP elicited by depolarizing current injection, inset: plot of the first derivatives as a function of time, and right: phase plot from inhibitory (pink) and excitatory (black) neurons. **(M-P)** Threshold AP analysis; **(M)** AP threshold, Mann-Whitney test, **p = 0.0024, **(N)** AP 10-90% Rise time, Mann-Whitney test, ****p < 0.0001, **(O)** AP 90-10% Decay time, Mann-Whitney test, **p = 0.0062, and **(P)** AP half width, Mann-Whitney test, **p = 0.0050.

Genetic crosses and statistical methods related to Figure 3: (A) PV^{TdTomato} BAC transgenic was used to identify PV expression in the medial deep dorsal horn. **(B)** For colocalization analysis of inhibitory and excitatory markers with dPVs we used 6 images from 2 *vGAT*^{iresCre};*Tau*$^{LSL\text{-}LacZ}$;PV^{TdTomato} , and 6 images from 3 *vGluT2*^{YFP};*PV*^{TdTomato} mice, respectively. **(C)** Quantification of percent dPVs expressing GAD65, GAD67, or GlyT2 was performed using 12 images from 4 *PV*^{FlpO};*R26*$^{FSF\text{-}GFP}$;*GAD2*^{mcherry} mice, 7 images from 3 GAD67^{GFP};PV^{TdTomato} mice; and 11 images from 3 GlyT2^{GFP} mice (staing with GP-PV). **(D)** sAP discharge was recorded in 316 dPVs from 40 PV^{TdTomato} mice; 260/316 (82%) showed sAP discharge. **(E)** Firing properties in response to current injections were examined in 51 dPVs from 9 PV^{TdTomato} mice. 49/51 (96%) exhibited non-adapting tonic firing properties (TF Na). **(F)** Left- sensory and proprioceptive inputs labeled with *PV*^{FlpO};*Advillin*^{Cre};*R26*$^{LSL\text{-}FSF\text{-}SynGFP}$/*R26*$^{LSL\text{-}Tomato}$. Right- for quantification of cutaneous and proprioceptive input onto dPVs, we used 21 neurons from 2 *PV*^{2aCreER};*Advillin*^{FlpO};*R26*$^{LSL\text{-}FSF\text{-}Tomato}$/*R26*$^{FSF\text{-}SynGFP}$ (2 mg tamoxifen treatment at P21-P23) mice. dPVs receive more input from cutaneous afferents, Mann Whitney test, **p = 0.0038. **(G)** Input from Aβ-field LTMR to dPVs shown using the cross *PTGFR*^{CreER};*R26*$^{LSL\text{-}SynTomato\ (Ai34)}$ (2 mg tamoxifen treatment at p21-p22), **(H)** Input from Aβ-RA LTMR to dPVs shown using the cross *Ret*^{CreER};*R26*$^{LSL\text{-}SynTomato\ (Ai34)}$ (2 mg tamoxifen treatment at E10-E11). **(I-M)** Photostimulation of proprioceptive (n = 28, 4 mice), Aβ-field (n = 31, 5 mice), Aβ-RA (n = 30, 4 mice), A - (n = 25, 3 mice), and C-LTMRs (n = 18, 2 mice) while recording from dPV neurons in *PV*^{2aCreER};*Advillin*^{FlpO};*R26*$^{LSL\text{-}FSF\text{-}ChR2\ (Ai80)}$;PV^{TdTomato} (2 mg tamoxifen at P21-P23), *PTGFR*^{CreER};*Advillin*^{FlpO};*R26*$^{LSL\text{-}FSF\text{-}ChR2\ (Ai80)}$;PV^{TdTomato} (2 mg tamoxifen at P21-P23), *Split*^{Cre};*R26*$^{LSL\text{-}ChR2\ (Ai32)}$;PV^{TdTomato}, *TrkB*^{CreER};*Advillin*^{FlpO};*R26*$^{LSL\text{-}FSF\text{-}ChR2\ (Ai80)}$;PV^{TdTomato} (2 mg tamoxifen at P21-P23), and *vGlut3*^{iresCre};*Advillin*^{FlpO};R26$^{LSL\text{-}FSF\text{-}ChR2\ (Ai80);}$PV^{TdTomato}, respectively. **(N)** Recordings were performed in 29 dPV neurons from 3 *CCK*^{iresCre};Lbx1^{FlpO};*R26*$^{LSL\text{-}FSF\text{-}ChR2\ (Ai80)}$;PV^{TdTomato} mice. 17/29 (59%) responded to optic stimulation of CCK interneurons. **(O)** oIPSCs recorded in a subset of proprioceptors (n= 18), Aβ-field (n = 15), Aβ-RA (n = 13), A - (n = 9), and C-LTMRs (n = 2) photostimulation experiments **(P)** Recordings performed in 25 dPV neurons from 2 *Rorβ*^{CreER};Lbx1^{FlpO};*R26*$^{LSL\text{-}FSF\text{-}ChR2\ (Ai80)}$;PV^{TdTomato} (2 mg tamoxifen treatment at P18-P19, mostly labeling LTMR-RZ Rorβ interneurons) mice. 6/25 (24%) showed a current response to optic stimulation of Rorβ interneurons.

Genetic crosses and statistical methods related to Figure 4: (A) For quantification of cfos expressing-dPVs (as percentage of rest), 14-19 images from 4-5 *vGAT*^{iresCre};*Rosa*$^{LSL\text{-}Tomato}$ were used. Percent cfos+dPVs increased in walk vs rest, Mann Whitney test, *p = 0.0286. **(B)** Cell-attached voltage-clamp recording of sAP discharge before and after application of a cocktail containing 20μM NMDA, 50 μM dopamine (DA) and 20μM serotonin (5-HT), previously used to induce fictive locomotion (Anderson et al. 2012; Wilson et al. 2005). **(C)** sAP instantaneous frequency (sAP-IF) recorded in 7 dPVs from 4 PV^{TdTomato} mice increased following cocktail application, paired t-test, * p = 0.0142. **(D)** Plot showing instantaneous sAP discharge following NMDA, 5-HT, and DA application. dPVs occasionally (3/7) respond with rhythmic AP bursting. **(E)** Whole-cell voltage clamp recording (-70 mV) showing dPV response to bath-application of NMDA, 5-HT, and DA. **(F)** Holding current recorded in 9 dPVs from 3 PV^{TdTomato} animals increased following cocktail application, paired t-test, ***p = 0.0004. **(G)** Whole-cell current clamp recording showing dPV response to bath-application of NMDA, 5-HT, and

DA. **(H)** Resting membrane potential (RMP) recorded in 19 dPVs from 4 $PV^{TdTomato}$ animals becomes more depolarized following cocktail application, paired t-test, ****p < 0.0001. **(I)** Cell-attached voltage clamp recording from dPV showing sAP discharge under control conditions (black), following bath-application of Bicuculline, Strychnine, CNQX (blue), and TTX (red). Right: sAP instantaneous frequency (sAP-IF) recorded in 11 dPVs from 2 $PV^{TdTomato}$ mice increased following Bicuculline, Strychnine, CNQX application, Wilcoxin matched-pairs signed rank test, **p = 0.0098. **(J-L)** The influence of primary afferent activity on dPV AP discharge was assessed following proprioceptive (n = 33, 4 mice), Aβ-field (n = 34, 5 mice), Aβ-RA (n = 43, 4 mice), A - (n = 22, 3 mice), and C-LTMR (n = 21, 2 mice) photostimulation. **(J)** Representative traces showing 10 consecutive sweeps of sAPs during sensory afferent stimulation (blue bar). Inset shows optically evoked AP. **(K)** Histogram of AP probability with an overlaid piecewise polynomial computed from p = 0.9 in MATLAB. **(L)** Grouped data showing oAP incidence following photostimulation of sensory afferent populations.

Genetic crosses and statistical methods related to Figure 5: (C-D) 9 dPV^{abl} (PV^{FlpO};$Lbx1^{Cre}$;$Tau^{LDL-FSF-DTR}$) and 6 dPV^{norm} (PV^{FlpO};$Tau^{LDL-FSF-DTR}$) mice, were intrathecally injected with 50 ng DTx. Mice were perfused following behavioral testing, and the spinal cord was sliced at the level of C6-8, T6-8 and L4-6. **(C)** Quantification of sPVs and dPVs throughout the cervical (dPV^{norm}: 15 images from 5 animals; dPV^{abl}: 26 images from 9 animals), thoracic (dPV^{norm}: 18 images from 6 animals; dPV^{abl}: 27 images from 9 animals) and lumbar segments (dPV^{norm}: 18 images from 6 animals; 26 images from 9 animals). For each image, the number of sPVs was normalized to total NeuN in LI-III, and the number of dPVs was calculated as a percentage of the number of superficial PVs to account for differences in PV staining success, which is tricky at this age. dPV^{abl} showed a decrease in dPVs in the lumbar segment, Mann Whitney test, *p = 0.0255**.** **(F-H)** For statistical analysis we used a linear mixed effects regression model with mouse ID as a random effect. The Holm-Bonferroni method was used to correct for multiple comparisons. Hindlimb swing time, stance time and step frequency were calculated from 6 dPV^{norm} and 9 dPV^{abl} mice. The following number of steps were used for dPV^{norm} and dPV^{abl}, respectively, at each speed: 20 cm/s- 154 and 214; 40 cm/s- 123 and 227; 60 cm/s- 71 and 151; 80 cm/s- 30 and 69. **(F)** dPV^{abl} vs dPV^{abl} at 20 cm/s, p = 0.4212; 40 cm/s, *p = 0.0488; 60 cm/s, *p = 0.0159, and 80 cm/s *p = 0.0488. **(G)** dPV^{abl} vs dPV^{abl} at 20 cm/s p = 1; 40 cm/s, p = 1; 60 cm/s, p = 1, and 80 cm/s, p = 1. **(H)** dPV^{abl} vs dPV^{abl} at 20 cm/s p = 0.8242; 40 cm/s, *p = 0.0224; 60 cm/s, ****p < 0.0001, and 80 cm/s, *p = 0.01. **(I)** For statistical analysis we used a linear mixed effects regression model with mouse ID as a random effect. The Holm- Bonferroni method was used to correct for multiple comparisons. Transition phase was calculated for the right hindlimb from 6 dPV^{norm} and 9 dPV^{abl} mice. The following number of steps were used for dPV^{norm} and dPV^{abl} , respectively, at each speed: 20 cm/s- 72 and 102; 40 cm/s- 59 and 111; 60 cm/s- 32 and 74; 80 cm/s-14 and 33. dPV^{abl} vs dPV^{abl} at 20 cm/s p = 0.7193; 40 cm/s, *p = 0.0416; 60 cm/s, *p = 0.0197; 80 cm/s p = 0.0891. **(J-N)** EMG recordings were obtained from 9 dPV^{norm} (6 PV^{FlpO};$Tau^{LSL-FSF-DTR}$ and 2 $Lbx1^{Cre}$;$Tau^{LSL-FSF-DTR}$) and 6 dPV^{abl} (PV^{FlpO};$Lbx1^{Cre}$;$Tau^{LSL-FSF-DTR}$). All mice were intrathecally injected with 50 ng DTx. **(L)** Statistical analysis was done using Mann Whitney tests with Holm-Sidak correction for multiple comparisons, dPV^{abl} flexors vs dPV^{norm} flexors, ****p < 0.0001; dPV^{abl} extensors vs dPV^{norm} extensors, *p = 0.0086. **(N)** Statistical analysis was done using Unpaired t- tests with Holm-Sidak correction for multiple comparisons, dPV^{abl} flexors vs dPV^{norm} flexors, *p = 0.0298; dPV^{abl} extensors vs dPV^{norm} extensors, ***p = 0.00016.

Genetic crosses and statistical methods related to Figure 6: (C-E) Plots were generated using 93 steps of 3 dPV^{norm} and 82 steps of 4 dPV^{abl} mice. For statistical analysis we used a linear mixed effects regression model with mouse ID as a random effect. The Holm- Bonferroni method was used to correct for multiple comparisons. **(D)** dPV^{abl} vs dPV^{norm} hip PEP, p = 0.1808; knee PEP, p = 0.0031; ankle PEP, p = 0.0079; MTP PEP, p < 0.0001. **(E)** dPV^{abl} vs dPV^{norm} hip PEP, p = 0.2789 ; knee PEP, p = 0.8105; ankle PEP, p = 0.2787; MTP PEP, p = 0.6482. **(F-J)** EMG recordings were obtained from 9 dPV^{norm} (6 PV^{FlpO};$Tau^{LSL-FSF-DTR}$ and 2 $Lbx1^{Cre}$;$Tau^{LSL-FSF-DTR}$) and 6 dPV^{abl} (PV^{FlpO};$Lbx1^{Cre}$;$Tau^{LSL-FSF-DTR}$). All mice were intrathecally injected with 50 ng

DTx. **(H)** Statistical analysis was done using Mann Whitney tests with Holm-Sidak correction for multiple comparisons, dPV^{abl} flexors vs dPV^{norm} flexors, **p = 0.0022; dPV^{abl} extensors vs dPV^{norm} extensors, **p = 0.0022. **J)** Statistical analysis was done using Mann Whitney tests with Holm-Sidak correction for multiple comparisons, dPV^{abl} flexors vs dPV^{norm} flexors, **p = 0.06; dPV^{abl} extensors vs dPV^{norm} extensors, **p = 0.2654.

Genetic crosses and statistical methods related to Figure 7: (A) Contour density plot was generated using 5 images from 2 PV^{FlpO};$Lbx1^{Cre}$;$Rosa26^{LSL\text{-}FSF\text{-}SynaptophysinGFP}$ mice. **(B)** PV^{FlpO};Lbx^{1Cre};$Rosa^{LSL\text{-}FSF\text{-}SynGFP}$;$Rosa^{LSL\text{-}FSF\text{-}TdTomato}$ was used to demonstrate dPVs' mutual connections. PV^{FlpO};Lbx^{1Cre};$Rosa^{LSL\text{-}FSF\text{-}SynGFP}$ stained with mouse- anti calbindin was used to demonstrate dPVs' connections to Renshaw cells. PV^{FlpO};Lbx^{1Cre};$Rosa^{LSL\text{-}FSF\text{-}SynGFP}$ stained with goat- anti ChAT was used to demonstrate dPVs' connections to V0c and MNs. V0c neurons were identified in lamina X, around the central canal, while MNs were identified by their location in lamina 9 and big soma. **(C)** Injections of the retrograde tracer Alexa fluor 555- conjugated CTb were made into muscles of PV^{FlpO};Lbx^{1Cre};$Rosa^{LSL\text{-}FSF\text{-}SynGFP}$ mice. The following muscles and number of animals were injected: VL (knee extensor)- 2 animals, biceps femoris (BFP, knee flexor)- 2 animals, lateral gastrocnemius (LG, ankle extensor)- 1 animal, and TA (ankle flexor)- 1 animal. The following number of MNs were used for synaptic analysis: 11 VL-MNs, 10 BFP- MNs, 9 TA- MNs, and 14 LG- MNs. Statistical analysis was performed using Mann Whitney test with the Holm-Sidak method for correction for multiple comparisons. dPVs showed preferred innervation onto extensor muscles, knee extensor vs knee flexor, *p = 0.029; ankle extensor vs ankle flexor, p = 0.0592. **(D-F)** Responses in dPVs to photostimulation of dPVs (mutual connections; n = 23, 3 mice) were recorded in PV^{FlpO};$Lbx1^{Cre}$;$Rosa26^{LSL\text{-}FSF\text{-}ChR2}$;$PV^{TdTomato}$ mice. Responses in V0c (n = 10, 4 mice), lateral MNs (n = 30, 4 mice), medial MNs (n = 8, 3 mice), and putative foot MNs (n = 14, 4 mice) to photostimulation of dPVs which were recorded in PV^{FlpO};$Lbx1^{Cre}$;$Rosa26^{LSL\text{-}FSF\text{-}ChR2}$;$ChATe^{GFP}$. Neurons were differentiated by their size, dorsoventral, and mediolateral positioning.

Tamoxifen treatment

Tamoxifen was dissolved in ethanol (20 mg/ml), mixed with an equal volume of sunflower seed oil (Sigma), vortexed for 5-10 min and centrifuged under vacuum for 20-30 min to remove the ethanol. The solution was kept at −80°C and delivered via oral gavage to pregnant females for embryonic or postnatal treatment. For all analyses, the morning after coitus was designated as E0.5 and the day of birth as P0.

Immunohistochemistry and free- floating sections

Male and female P30-P37 mice were anesthetized with isoflurane and perfused transcardially (using an in-house gravity driven- perfusion system) with heparinized- saline (~30 sec) followed by 15-20 minutes of 4% paraformaldehyde (PFA) in PBS at room temperature (RT). Vertebral columns were dissected and post-fixed in 4% PFA at 4°C for 2-24 hr. Sections were collected using a vibrating microtome (Leica VT1200S) and processed for immunohistochemistry (IHC) as described previously (Hughes et al., 2012). Unless otherwise mentioned, transverse sections (50-60 µm thick) were taken from limb level lumbar spinal cord (L4-6). Free floating sections were rinsed in 50% ethanol (30 min) to increase antibody penetration, followed by three washes in a high salt PBS buffer (HS-PBS), each lasting 10 min. The tissue was then incubated in a cocktail of primary antibodies made in HS- PBS containing 0.3% Triton X-100 (HS-PBSt) for 48 at 4°C. Next, tissue was washed 3 times (10 minutes each) with HS-PBSt, then incubated in a secondary antibody solution made in HS-PBSt for 24 hr at 4°C. Immunostained tissue was mounted on positively charged glass slides (41351253, Worldwide Medical Products) and coverslipped (48393-195, VWR) with Fluoromount-G mounting medium (100241-874, VWR).

Image acquisition and analysis

Images were captured with a Zeiss LSM 800 confocal or a Zeiss axiovert 200M fluorescence microscope. Images for cell counts were taken with 10x or 20x air objectives, and images of synaptic contacts were taken using a 40x oil objective. ImageJ (cell count plug-in) was used for colocalization analysis of cell bodies. Imaris (spot detection plug-in) was used for synaptic analysis, quantification of synaptic terminals (Figure 1C), and generation of contour density plots. For synaptic analysis of proprioceptive and cutaneous input onto dPVs, the fraction of each input was calculated relative to their sum. For synaptic analysis of dPVs output to target neurons, input was normalized to cell body area or dendrite length. Only puncta apposing a postsynaptic marker (Homer1 and Gephyrin for excitatory and inhibitory synapses, respectively) were included for analysis. Synaptic analysis was performed separately for somas and proximal dendrites (up to 50 µm from the cell body). For quantification of proprioceptive and cutaneous synaptic terminals across the dorsoventral axis, synaptophysin GFP (all sensory) was used to mask the tomato (proprioceptive fibers) channel to generate a separate channel of red and green proprioceptive puncta. Counts of all cutaneous (GFP+), and proprioceptive (GFP+ Tomato+) were performed separately for LI-III,LIV_{medial},$LIV_{lateral}$, LV_{medial}, $LV_{lateral}$, LVI,LVII,LVIII, LIX, and LX. The number of cutaneous puncta in each lamina was then calculated from the subtraction of proprioceptive from sensory puncta. To generate contour density plots, Imaris spot detection plug-in was used to detect the spatial coordinates of cell bodies/synaptic terminals. Following detection, coordinate values were corrected and expressed relative to common reference points (central canal, dorsal, lateral and ventral edges of the gray matter). Corrected coordinates were used to obtain two dimensional kernel density estimation utilizing the MATLAB ‘ksdensity’ function. Kernel density estimations were graphically displayed as contour plots, using the MATLAB ‘contourf’ function.

c-Fos induction

Mice were transferred to a holding area adjacent to the testing room at least 7 days prior the experiment, to decrease stress during the task. 6-8 weeks old mice were randomly placed in one of three groups: control , swim and walk. All mice were habituated to the testing room for 30 minutes. Control mice were kept in their homecage for 60 minutes. “Walk” group walked on a treadmill (Mouse Specifics, Inc, Boston, MA, USA) at 20 cm/s for 2 x 20 minutes with a 5 minute break. “Swim” group were kept in a swim tank for 4 x 10 minutes with 5 minutes breaks. 60 minutes following the completion of the task, mice were anesthetized with isoflurane and perfused for immunohistochemistry. Sections stained with chicken-β-galactosidase (ab9361, Abcam), mouse-NeuN (MAB377, Millipore), and rabbit- c-fos (226003, Synaptic systems) were used to acquire 20x images of the entire hemisection, stitches with zen. Images were then used for quantification of c-fos expressing neurons (normalized to total NeuN) by lamina (figure 1) and cfos expressing inhibitory (vGAT+cfos+NeuN+) and excitatory (vGAT-cfos+NeuN-) neurons in the medial portion of laminas 4-5 (Figure 2). Alternate sections from the same animals stained with Guinea pig-PV (PV-GP-Af1000, Frontier institute) and c-fos, were used to acquire 20x images of the medial deep dorsal horn to quantify the fraction of dPVs that express cfos in each of the 3 conditions (Figure 3). All images were acquired with the Zeiss LSM 800 confocal microscope.

CTb muscle injection

$PV^{FlpO};Lbx1^{Cre};R26^{LSL\text{-}FSF\text{-}SynaptophysinGFP}$ mice were anesthetized (5% induction, 2-3% maintenance), and the hair above one of their hindlimbs was shaved. The skin was wiped with 70% ethanol and cut to expose the hindlimb muscles. Injections of 0.125% Alexa fluor 555- conjugated CTb (2-3 sites along each muscle) were made into the knee extensor vastus lateralis(VL), knee flexor biceps femoris (BFP), ankle extensor lateral gastrocnemius (Gs), and ankle flexor tibialis anterior (TA). Animals were perfused 5 days after CTb injection and tissue was processed for IHC as described above. Free floating sections were immunostained with chicken-GFP (GFP-1010, Aves) and mouse- Gephyrin (147 021, Synaptic systems) primary antibodies, and appropriate

secondary antibodies. 40x images of CTb- labeled motor neurons were taken at the Zeiss LSM 800 confocal microscope and ImageJ was used for synaptic analysis.

Timing of dPV neurogenesis

Pregnant $PV^{TdTomato}$ females were intraperitoneally (i.p) injected with 50 mg/kg EdU (Fisher Scientific, C10337) at E10.5, E11.5 and E12.5. $PV^{TdTomato}$ F1 progeny (identified with PCR genotyping) were perfused at P30-P37 and L4-L6 spinal cord sections were collected using a vibrating microtome (Leica VT1200S). EdU was revealed as previously described using a click reaction (Chehrehasa et al. 2009). After EdU staining, slices were additionally stained with rabbit-DsRed (632496, Takara) and appropriate secondary antibodies as described above, for amplification of PV fluorescence. Following, 20x confocal images of the medial deep dorsal horn were taken and used to quantify EdU expressing-dPVs at each embryonic day.

Neuronal reconstructions and morphometric analysis

Sagittal sections of PV^{FlpO};$Lbx1^{Cre}$;$R26^{LSL\text{-}FSF\text{-}TdTomato}$ lumbar spinal cords were immunostained with Guinea-pig PV, and 20x, z stack images were taken on a Zeiss LSM 800 confocal microscope. Stacks were manually reconstructed using the Neuromantic software. Reconstructions were then opened with ImageJ to measure somatic area and neurite length. Spine counts were performed with the cell counter plug-in to calculate spine density for each neuron (number of spines/ total neurite length). Sholl regression plug-in was used to perform sholl regression, to characterize neuronal arbors, as described as previously described (Sholl 1953). Briefly, the plug -in creates a series of concentric spheres around the soma, and counts the number of intersections with each sphere. A linear regression is fitted to the sampled data (number of intersections vs distance from the soma) and sholl regression coefficient (the slope of the linear regression) is calculated. The Regression coefficient represents the decay in the number of branches with distance from the cell body where higher values denote faster decay.

Electrophysiology

Recordings were made from male (n = 33) and female (n = 32) mice (5.1 +/- 0.2 wks). Mice were anesthetized with ketamine (100 mg/kg i.p), decapitated, and the lumbar enlargement of the spinal cord rapidly removed in ice-cold sucrose substituted artificial cerebrospinal fluid (sACSF) containing (in mM): 250 sucrose, 25 $NaHCO_3$, 10 glucose, 2.5 KCl, 1 NaH_2PO_4, 6 $MgCl_2$, and 1 $CaCl_2$. Sagittal or transverse slices (200µm thick) were prepared using a vibrating microtome (Leica VT1200S). Slices were incubated for at least 1 hour at 22-24°C in an interface chamber holding oxygenated ACSF containing (in mM): 118 NaCl, 25 $NaHCO_3$, 10 glucose, 2.5 KCl, 1 NaH_2PO_4, 1 $MgCl_2$, and 2.5 $CaCl_2$.

Following incubation, slices were transferred to a recording chamber and continually superfused with ACSF bubbled with Carbogen (95% O_2 and 5% CO_2) to achieve a pH of 7.3-7.4. All recordings were made at room temperature (22-24°C) and neurons visualized using a Zeiss Axiocam 506 color camera. Recordings were acquired in cell-attached (holding current = 0mV), voltage-clamp (holding potential -70mV), or current-clamp (maintained at −60mV). Patch pipettes (3-7 MΩ) were filled with a potassium gluconate-based internal solution containing (in mM): 135 $C_6H_{11}KO_7$, 8 NaCl, 10 HEPES, 2 Mg_2ATP, 0.3 Na_3GTP, and 0.1 EGTA, (pH 7.3, adjusted with KOH, and 300 mOsm) to examine AP discharge and excitatory synaptic transmission. A cesium chloride-based internal solution containing (in mM): 130 CsCl, 10 HEPES, 10 EGTA, 1 $MgCl_2$, 2 Na-ATP, 2 Na-GTP, and 5 QX-314 bromide (pH 7.3, adjusted with CsOH, and 280 mOsm) was used to record inhibitory synaptic transmission. No liquid junction potential correction was made, although this value was calculated at 14.7 mV (22°C). Slices were illuminated using an X-CITE 120LED Boost High-Power LED Illumination System

that allowed visualization of Td-Tomato expressing dPVs with TRITC filters, and visualization of GFP fluorescence and ChR2 photostimulation using FITC filter set.

AP discharge patterns were assessed in the current clamp from a membrane potential of −60 mV by delivering a series of depolarizing current steps (1 s duration, 20 pA increments, 0.1 Hz), with rheobase defined as the first current step that induced AP discharge. Spontaneous action potential discharge was assessed using cell-attached voltage clamp recordings, with minimal holding current (< 20 mV). For optogenetic circuit mapping, photostimulation intensity was suprathreshold (24 mW), duration 1 ms (controlled by transistor-transistor logic pulses), 0.1 Hz. This ensured generation of action potential discharge in presynaptic populations and allowed confident assessment of postsynaptic currents in recorded neurons.

All data were amplified using a MultiClamp 700B amplifier, digitized online (sampled at 20 kHz, filtered at 5 kHz) using an Axon Digidata 1550B, acquired and stored using Clampex software. After obtaining the whole-cell recording configuration, series resistance, input resistance, and membrane capacitance were calculated (averaged response to -5mV step, 20 trials, holding potential -70mV).

Electrophysiology Analysis

All data were analyzed offline using AxoGraph X software.

AP discharge was classified according to previously published criteria (Browne et al. 2020). Briefly, tonic firing (TF) neurons exhibited continuous repetitive AP discharge for the duration of the current injection; initial bursting (IB) neurons were characterized by a burst of AP discharge at the onset of current injection; delayed firing (DF) neurons exhibited a clear interval between current injection and the first AP; and single spiking (SS) neurons that discharge one or two APs at depolarization step onset. In addition, we also divided the TF population into two subpopulations; TF non-accommodating (TF_{Na}) neurons maintained the TF profile with incremental current injection; TF accommodating (TF_{Ac}) neurons could not maintain the TF profile with incremental current injection, and AP duration dropped below 900 ms or reduced by more than 10%. In the analysis of AP discharge, individual APs elicited by step-current injection were captured using a derivative threshold method (dV/dt > 15 V/second) with the inflection point during spike initiation defined as the AP threshold. Individual AP properties for each neuron were assessed from the first spike generated at the rheobase. AP latency was measured as the time difference between the stimulus onset and AP threshold. The difference between the AP threshold and its maximum positive peak was defined as the AP peak. AP half-width was measured at 50% of AP peak. AP rise and decay time were measured from 10-90% of peak. AP afterhyperpolarization (AHP) amplitude was taken as the difference between the AP threshold and the maximum negative peak following the AP. AHP half-width was measured at 50% of AHP peak. AP threshold adaptation was determined by dividing the AP threshold of the last AP by the AP Threshold of the first AP evoked by a step-current. AP number was the number of spikes discharged in the entire response. Instantaneous frequency is the average instantaneous frequency across a step-current.

Optogenetically-evoked excitatory postsynaptic currents (oEPSCs) and inhibitory postsynaptic currents (oIPSCs) were measured from baseline, just before photostimulation. The peak amplitude of responses was calculated from the average of 10 successive trials. A number of parameters were considered for determining whether a photostimulation-evoked synaptic input was monosynaptic or polysynaptic. The latency of oPSCs was measured as the time from photostimulation to the onset of the evoked current. The “jitter” in latency was measured as the standard deviation in latency of 10 successive trials. Importantly, the latency of monosynaptic inputs was much shorter, there was minimal jitter in the onset of responses between trials, and reliability (percentage of photostimulation trials to evoke a response) was higher than those deemed polysynaptic inputs. To assess the contribution of different neurotransmitter systems to photostimulation responses, various

synaptic blockers were sequentially applied.

Diphtheria Toxin preparation and delivery

DTx was dissolved in 1xPBS to 100 ug/ml and kept at −20°C. On the day of injection, DTx was diluted 1:10 in a hyperbaric solution (filtered 0.9% NaCl, 8% dextrose) as previously described (Albisetti et al. 2019). P21-P28 mice carrying the *PV*^{FlpO};*Lbx1*^{Cre};*Tau*$^{LSL\text{-}FSF\text{-}DTR}$ (dPVs^{abl}) or *PV*^{FlpO}/*Lbx1*^{Cre};*Tau*$^{LSL\text{-}FSF\text{-}DTR}$ (dPVs^{norm}) alleles, received Diphtheria Toxin (DTx, D0564-1MG, Sigma) on day 1 and 3 (5 ul of 10 ug/ml DTx, overall 50 ng) through intrathecal (I.T.) injection to the L5-L6 intervertebral space. DTx was delivered with a 25 ul Hamilton syringe (72310-388) with a 30G needle and performed as previously described (Li et al. 2019). Briefly, mice were anesthetized with isoflurane and the hair above their lower back was removed. Under anesthesia, exposed skin was wiped with 70% ethanol. Next, mice were held firmly by the pelvic girdle with their skin taut in one hand, while the other hand was used to gently rotate the base of the tail to find the midline of the spine. Needle was inserted through the skin along the midline, between the pelvic girdles to the L5-L6 intervertebral space. An occurrence of a sudden tail indicated successful entry into the intradural space.

Quantification of DTx mediated ablation

Following behavioral testing, dPV^{norm} (*PV*^{FlpO}/Lbx^{1Cre};*Tau*$^{LSL\text{-}FSF\text{-}DTR}$) and dPV^{abl} (*PV*^{FlpO};Lbx^{1Cre};*Tau*$^{LSL\text{-}FSF\text{-}DTR}$) mice were perfused, their spinal cord and cerebellum were dissected, and sectioned using a vibrating microtome (Leica VT1200S). For consistency, sections were collected at the levels of the mid cervical enlargement, mid thoracic, mid lumbar enlargement, and the midline of the cerebellum. Sections were immunostained with Guinea pig-PV and mouse- NeuN, and 20x images were taken using the Zeiss axiovert 200M fluorescence microscope. 3 spinal cord (at each level) and 2 cerebellum images from each animal were used for quantification. PV neurons were counted in the superficial dorsal horn (sPVs), deep dorsal horn (dPVs) and molecular layer of the cerebellum. sPVs were normalized to NeuN, dPVs were normalized to sPVs (to account for difference in staining success), and PV neurons in the molecular layer were normalized to area.

Behavioral testing

7-12 weeks old male and female dPV^{norm} (*PV*^{FlpO}/Lbx^{1Cre};*Tau*$^{LSL\text{-}FSF\text{-}DTR}$) and dPV^{abl} (*PV*^{FlpO};Lbx^{1Cre};*Tau*$^{LSL\text{-}FSF\text{-}DTR}$) mice injected with DTx (at P21-P28) were used for behavior testing .The experimenter was blind to the genotype of the animals. For all behavior assays, at least 7 days prior testing mice were transferred to the holding area adjacent to the behavior rooms. On the day of training/testing, mice were transferred to the behavior room for a 30 minute habituation.

Balance beam

Mice were trained for 2 days to cross an elevated, 1m long, 10 mm wide rectangular beam. On test day, mice were allowed to cross wide and narrow (10 mm and 5 mm, respectively) rectangular and circular beams. Individual trials were video-recorded at 30 frames per second (fps) using GoPro camera, capturing mouse performance from one side. A slightly angled mirror, positioned on the other side of the mouse, was used to capture the performance of the limbs that did not face the camera. Each mouse performed 3 consecutive trials on each beam and the total number of slips and time to cross the beam were measured. All beams were custom made.

Horizontal ladder

Mice were trained for 2 days to cross a 60 cm long, horizontal ladder (Maze Engineers, Skokie, USA). The ladder was elevated from the ground with two cages, a neutral cage at the start and homecage at the end, to motivate mice to cross the ladder. The ladder consisted of 2 transparent side walls, with drilled holes in regularly spaced, 1 cm intervals, allowing for the insertion of metal bars (0.3 cm wide) at different spacing. During training days, ladder rungs were spaced 1 cm apart (regular pattern ladder) and mice performed 3-5 consecutive trials of ladder crossing. On the test day, mice performed 3-5 trials on a regular pattern ladder. Mice were allowed to rest for 2-3 hours, then performed 3 trials on an irregular pattern ladder where some rungs were spaced 2 cm apart. 3 different irregular patterns were used for each mouse which were consistent across mice. A camera (PROMON U1000, AOS Technologies, AG, Switzerland)) located to the side of the mouse and positioned in an angle to capture the performance of all 4 paws was used to videotype mouse performance at 30 fps. Videos were analyzed frame by frame to quantify the number of slips.

Rotarod test

The rotarod assay lasted for 5 days. On the first day, mice were habituated to the apparatus and placed on the rotarod (rotating at 4 rpm) for a maximum of 3 minutes. On following days, mice were put on the accelerating rotarod (4-40 rpm, maximum of 3 minutes), and their latency to fall and speed at fall were measured. Mice performed 4 trials each day, with a break of 15-20 minutes between trials.

Analysis of step cycle parameters

Mice were allowed to walk on a motorized treadmill (Mouse specifics, inc.) with a transparent belt at speeds 10-100 cm/s for 2 days. Each mouse had to exhibit a minimum of 3 second walk at a certain speed, for it to be included in the analysis. The second day was used to allow mice to walk at speeds they failed at on the first day. A high speed camera (165 fps) located underneath the belt, recorded mice' paw placement. A custom-developed software was used to extract the area of the paw that was in contact with the belt for each paw, and in each video frame, as described in (Hampton et al. 2004). These data were analyzed in MATLAB, to calculate stance duration (when paw area > 0), swing duration (paw area = 0), stride duration (stance duration + swing duration) and stride frequency (number of strides per second) of each limb. To calculate stance-to-swing phase transition, or interlimb coordination, each step cycle was normalized to values of 0 (beginning of stance) to 1 (end of swing). Phase transition between stance to swing was considered as the time in which the paw area (normalized to maximal paw area) changed from values greater than 0 to 0. Limb coupling phase values were calculated as the time difference between stance onset of the tested limb and the reference limb (left hindlimb for ipsilateral, diagonal, and hindlimb coupling and left forelimb for forelimb coupling) divided by the duration of the step cycle of the reference limb (Figure S6A). Phase values of 0/1 ($\pm$0.25), 0.5($\pm$0.25), and 0.25/0.75 ($\pm$0.25), indicated in phase (synchronization), anti-phase (alternation), or out-of phase limb coupling, respectively. Gaits were classified as walk, trot, gallop or bound and their occurrence, persistence, and attractiveness were calculated as described previously (Lemieux et al. 2016). For a given gait, occurrence was calculated as its percentage out of all gaits. Persistence was calculated as the percentage of two consecutive steps using that gait out of all consecutive steps. Attractiveness was the likelihood of other gaits transferring to the gait in question.

Estimation of joint angles

One day before the test, the hair above the right hindlimb of mice was removed. On test day, mice were habituated to the test room for 30 minutes, and under brief anesthesia 5 marker dots (oil-based white marker, 208423, Office Depot) were placed on the following joints of their right hindlimb: iliac crest, hip, ankle, metatarsophalangeal (MTP) and toe. Due to excess skin above the knee, knee joint location was estimated post-hoc using measurements of tibia and femur length. 6 calibration points with a known distance (5 mm apart) were put on the upper right side of the transparent wall of a motorized treadmill (Mouse specifics, inc.). Mice were placed on the treadmill to recover from anesthesia (~5 minutes), and then let to walk at 20 cm/s. A high speed camera (PROMON U1000, AOS Technologies, AG, Switzerland) recorded mice performance from the side, at 415 fps. Videos were analyzed with DeepLabCut for 2D estimation of joint marker location in each video frame as described in (Mathis et al. 2018). Briefly, 2 separate models were created for the calibration points and joint markers. Each model was trained with a random subset of videos. An average of 125 frames were extracted and labeled by clustering based on similarities in visual appearance (k-means). The models were trained with a ResNet-50-based neural network for an average of 300,000 training iterations. Using a p-cutoff of 0.9, the training datasets were shuffled with the default 95/5 split for training and testing, and evaluated with an average train error: 2.16 pixels, test: 2.38 pixels. Incorrectly labeled or missing labels were detected and corrected via extraction of outlier frames, refinement of label errors, and subsequent retraining of the model. With minimal retraining, models were able to estimate and yield 2D pixel coordinates. We used the estimated pixel coordinates of the calibration points to calculate a pixel- to- mm conversion value, then estimated the location of the knee joint in each frame using the lengths of the femur and tibia. A custom semi-automatic matlab script was used to identify the beginning of stance (the first frame on which the toe touches the ground) and swing (the first frame of paw lift-off) in each step cycle (defined from the beginning of stance to the end of swing). The complete data set of the estimated location of all 6 joints was used to generate stick diagrams of hindlimb pose and calculate the instantaneous joint angle between every three consecutive markers, throughout the step cycle.

Statistical analysis of step cycle and kinematic parameters

For the analyses of step cycles and joint angles (**Figure 4E-F,H**; **Figure S6B-E**), all cycles/joint angles from all mice were used and statistical analysis was performed with a linear mixed effects regression model with mouse ID as a random effect. Analysis was performed using the ‘fitlme’ MATLAB function.Interlimb coordination data were analyzed using Watson’s non-parametric two-sample U test (Orlovsky, Deliagina, and Grillner 1999) .

Construction of EMG electrodes

EMG electrodes were made using multi-stranded, teflon coated annealed stainless-steel wire (A-M systems, 793200). The construction of the EMG electrode and nerve cuff was previously described in detail (Pearson, Acharya, and Fouad 2005; Akay et al. 2006; 2014). Two nerve cuff electrodes and six EMG recording electrodes were attached to the headpiece pin connector (female, SAM1153-12; DigiKey Electronics Thief River Falls, MN) and covered with 3D printed cap.

EMG electrode implantation surgeries

Experiments were conducted on 4-5 month-old males and females dPVs^{norm} (*PV*^{FlpO}/Lbx^{1Cre};*Tau*$^{LSL\text{-}FSF\text{-}DTR}$) and dPVs^{abl} (*PV*^{FlpO};Lbx^{1Cre};*Tau*$^{LSL\text{-}FSF\text{-}DTR}$) mice.

All surgeries were performed in aseptic conditions and on a warm water-circulated heating pad, maintained at 42°C. Each mouse underwent an electrode implantation surgery as previously described (Laflamme and Akay 2018; Laflamme, Ibrahim, and Akay 2022). Briefly, animals were anesthetized with isoflurane (5% for

inductions, 2% for maintenance of anesthesia), ophthalmic eye ointment was applied to the eyes, and the skin of the mice was sterilized with three-part skin scrub using hibitane, alcohol and povidone-iodine. Prior to each surgery, buprenorphine (0.03 mg/kg) and meloxicam (5 mg/kg) were injected subcutaneously as analgesics while the animals were still under anesthesia. Additional buprenorphine injections were performed in 12-hour intervals for 48 hours.

A set of six bipolar EMG electrodes and two nerve stimulation cuffs were implanted into each mouse as the following: small incisions were made on the shaved areas (neck and both hind legs), and each bipolar EMG electrode and the nerve cuff electrodes were led under the skin from the neck incisions to the leg incisions, and the headpiece connector was stitched to the skin around the neck incision. EMG recording electrodes were implanted into the left knee flexor (semitendinosus, St_l), ankle flexor (tibialis anterior, TA_l) and extensor (gastrocnemius, Gs_l) as well as the right knee flexor (semitendinosus, St_r) and extensor (Vastus Lateralis, VL_r) and the left ankle extensor (gastrocnemius, Gs_r). Nerve stimulation electrodes were implanted in the left saphenous nerve and right sural nerve to evoke cutaneous feedback. After surgery, the anesthetic was discontinued, and mice were placed in a heated cage for three days before returning to a regular mouse rack. Food mash and hydrogel were provided for the first three days after the surgery. Any mouse handling was avoided until mice were fully recovered, and the first recording session started at least ten days after electrode implantation surgeries.

EMG recording sessions

After animals fully recovered (~10 days) from electrode implantation surgeries, recording session went as follows: Under brief anesthesia with isoflurane, a wire to connect the headpiece connector with the amplifier and the stimulation insulation units (ISO-FLEX -AMPI, Jerusalem, Israel or the DS4 -Digitimer, Hertfordshire, United Kingdom) were attached to the mouse. Anesthesia was discontinued, and the mouse was placed on a mouse treadmill (model 802; custom built in the workshop of the Zoological Institute, University of Cologne, Germany). The electrodes were connected to an amplifier (model 102; custom built in the workshop of the Zoological Institute, University of Cologne, Germany) and a stimulus isolation unit. After the animal fully recovered from anesthesia (at least 5 minutes), the minimal (threshold) current necessary to elicit local reflex responses in the ipsilateral leg was determined by injecting a double impulse of 0.2 ms duration into the saphenous nerve (average ±SD threshold current: 436.4 μA ±396; range: 120-1300 μA) and the sural nerve (average ±SD threshold current: 117.6 μA ±83.4; range: 28-230 μA) of $dPVs^{norm}$, and the saphenous nerve (average ±SD threshold current: 215 μA ±157.9; range: 64-450 μA) and the sural nerve (average ±SD threshold current: 253.3 μA ±127.5; range: 130-500 μA) of $dPVs^{abl}$. Following the determination of threshold currents, the current injected into the sural and saphenous nerve was set as either 1.2 times the local reflex threshold current (1.2 X threshold) or five times the local reflex threshold current (5 X threshold).

EMG signals from six muscles of the right and left leg were simultaneously recorded (sampling rate: 10 kHz). Nerve stimulations (five 0.2ms impulses at 500 Hz) were applied using the ISO-FLEX (AMPI, Jerusalem, Israel) and DS4 (Digitimer, Hertfordshire, United Kingdom) stimulation insulation units. Stimulation protocols were recorded while the mice were resting on the treadmill. EMG signals were amplified (gain 100), band-pass filtered from 400 Hz to 5 kHz, and stored on the computer using Power1410 interface and Spike2 software (Cambridge Electronic Design, Cambridge, United Kingdom). For the single nerve assay, saphenous or sural nerve were electrically stimulated, while for the paired nerves assay, both nerves were stimulated at varying delays (0,5,15,15,20,25,30,35,40,45, or 50 ms). Paired stimulation of both legs at varying delays provided evidence of an inhibitory period if there was a suppression of the motor responses from one leg following stimulation of the other leg. Varying delays were used to account for differences in response latencies to the 2 nerves within muscles and within animals.

Analysis of EMG responses

EMG analysis response was done using Spike2 software (Cambridge Electronic Design, Cambridge, United Kingdom). For the single nerve assay, latency to response was measured for each mouse and each muscle. For the paired nerve assay, responses (single trials) were compared to the averaged response to stimulation of a single nerve (averaged over 20 trials), termed “expected response”. Responses (expected response and response to paired nerve assay) were aligned using the onset of the stimulation artifact, or the time when it was expected to occur, when the artifact was not visible. When “expected response” possessed higher amplitude than the paired stimulation response, the trial was considered to include an inhibitory component (originating from the nerve that was not used to evoke the expected response). Next, percent inhibition, the percentage of trials on which inhibition occurred was calculated for each muscle, and each mouse. For quantification of percent inhibition, a single delay (used in the paired nerve assay) was chosen, which could vary between muscle and mice. Delay at which the peak amplitude of the expected response was located 10-20 ms after the second nerve stimulation was chosen for further analysis, as this latency was shown to involve an inhibitory pathway (Laflamme and Akay, 2018; Laflamme et al. 2022).

Quantification and statistical analysis

All data are reported as mean values ± s.e.m. Behavioral assays were repeated several times (3 to 5 times depending on the experiment) and averaged per animal. Statistical analysis was performed in GraphPad Prism (USA) or Matlab, using two-sided paired or unpaired Student's t-tests, one-way ANOVA for neuromorphological evaluations with more than two groups, and one- or two-way repeated-measures ANOVA for functional assessments, when data were distributed normally. Post hoc holm-Sidak or Holm- Bonferroni tests were applied when appropriate. The significance level was set as $p < 0.05$. The nonparametric Mann-Whitney or Wilcoxon signed-rank tests were used in comparisons of <5 mice. Statistics were performed over the mean of animals. For the analyses of step cycles and joint angles, all cycles/joint angles from all mice were used and statistical analysis was performed with a linear mixed effects regression model with mouse ID as a random effect.

DATA AND CODE AVAILABILITY

Data are available upon request from the Lead Contact, Victoria E. Abraira (victoria.abraira@rutgers.edu).

SUPPLEMENTARY FIGURES AND TABLES

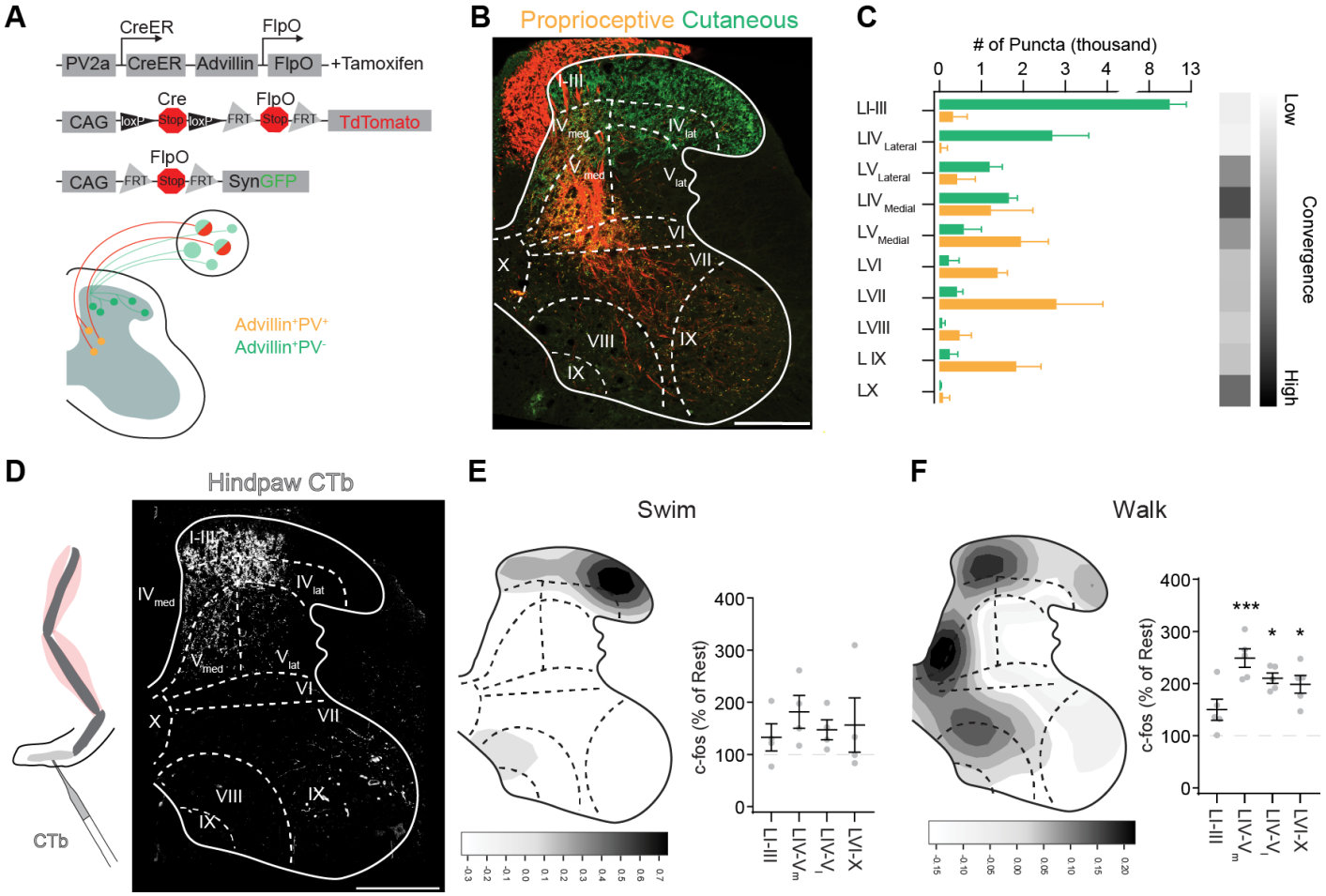

Figure 1. The medial deep dorsal horn, a region for convergence proprioceptive and cutaneous input, is recruited in walking. A) Top- quadruple transgenic *PV*^{2aCreER};*Advillin*^{FlpO};*Rosa*$^{LSL\text{-}FSF\text{-}Tomato}$/*Rosa*$^{FSF\text{-}SynGFP}$ mice are used to label cutaneous and proprioceptive terminals. Bottom- schematic showing expected expression. Synaptic terminals (Advillin+) of all sensory fibers are labeled in green, while proprioceptors (PV+Advillin+) fibers are labeled in red. Consequently, in the spinal cord, proprioceptors terminals are identified by both green and red fluorescence (yellow), while cutaneous terminals are identified by green fluorescence alone. **B)** Representative transverse section of limb level lumbar spinal cord from the genetic intersection in B, showing convergence of cutaneous and proprioceptive input in LIV_{medial}-LV_{medial}. **C)** Quantification of proprioceptive (red +green) and cutaneous (green only) by rexed laminae shows most convergence occurs in LIV_{medial}-LV_{medial}. **D)** Left- schematic of CTb injection into the ventral paw of a WT mouse. Right- representative transverse section of limb level lumbar spinal cord from the experiment to the left. Anterogradly labeled CTb+ primary sensory afferents innervating the ventral paw are shown to terminate in the dorsomedial spinal cord. **E-F)** C-fos expression is increased LIV_{medial}-LV_{medial} during walking. **E-left, F-left)** Contour heat maps depicting the change in the density of c-fos expression in swim (E-left), and walk (F-left) relative to rest . **E-right, F-right)** Quantification of c-fos as percentage of rest across lamina groups (LI-III, LIV-V_{Medial}, LIV-$V_{Lateral}$, and LVI-X). Graphs show average +S.E.M. Scale bar: 200 µm. Statistical analysis was done using Kruskal Wallis test with Dunn's correction for multiple comparisons, , with *$p < 0.05$, **$p < 0.005$, and ***$p < 0.0005$. For further details on genetic crosses, see Methods.

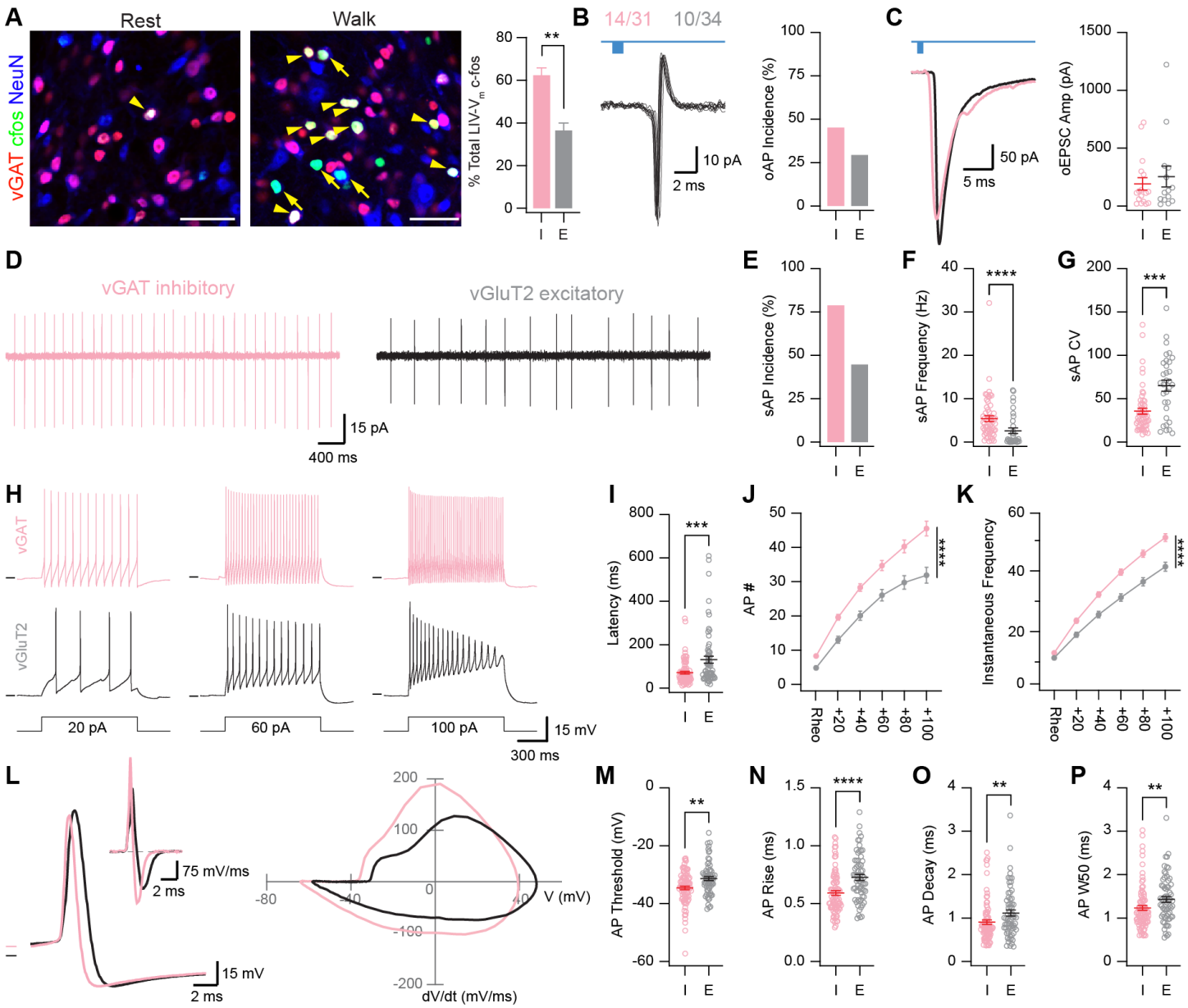

Figure 2. **DDH inhibitory interneurons are preferentially recruited during walking due to their excitable electrophysiological properties**. **A)** Left, middle- representative confocal images, zoomed-in on LIV_{Medial}-V_{Medial}, show c-fos expressing inhibitory (cfos+vGAT+NeuN+, yellow arrowheads) and excitatory (cfos+vGAT-NeuN+, yellow arrows) neurons from mice that performed rest (left) or walk (middle). Scale bars: 40 µm. Right- quantification of the percentage of inhibitory (I) and excitatory (E) c-fos expressing neurons in LIV_{Medial}-V_{Medial} shows preferential recruitment of inhibitory neurons. **B)** Cell-attached voltage clamp recording from putative DDH inhibitory (GAD67+, pink) and excitatory (GAD67-, gray) neurons following optic stimulation of sensory input, showing 10 consecutive traces of optically evoked action potential (oAP) discharge (left) and oAP incidence (right). **C)** Whole-cell voltage-clamp recording showing average of 10 consecutive traces following sensory afferent stimulation (left) and group data for oEPSC amplitude (right). **D)** Cell-attached voltage clamp recording showing spontaneous AP discharge in DDH inhibitory (pink) and excitatory (black) neurons. **E)** Inhibitory neurons exhibited higher sAP incidence; **F)** higher sAP frequency; **G)** and lower sAP coefficient of variation. **H)** Representative responses of inhibitory (pink, top) and excitatory (black, bottom) DDH neurons to depolarizing current injection. **I)** Inhibitory interneurons exhibited lower latency to 1st AP; **J)** increased number of APs; and **K)** increased instantaneous AP frequency in response to current injections. **L)** Representative threshold AP elicited by depolarizing current injection (left) and plot of the first derivatives as a

function of time (top right). **M)** phase plot from inhibitory (pink) and excitatory (black) neurons. **N-Q)** Threshold AP analysis; **N)** AP threshold, **O)** AP 10-90% Rise time, **P)** AP 90-10% Decay time, **Q)** AP half width. Graphs show average +S.E.M. Statistical analysis was done using Mann Whitney test (A, F-G, N-Q) or Unpaired T-test (I), or two-way ANOVA (J-K), with *p < 0.05, **p < 0.005, ****p < 0.0005 and ****p < 0.0001. For further details on genetic crosses and statistical tests see Methods.

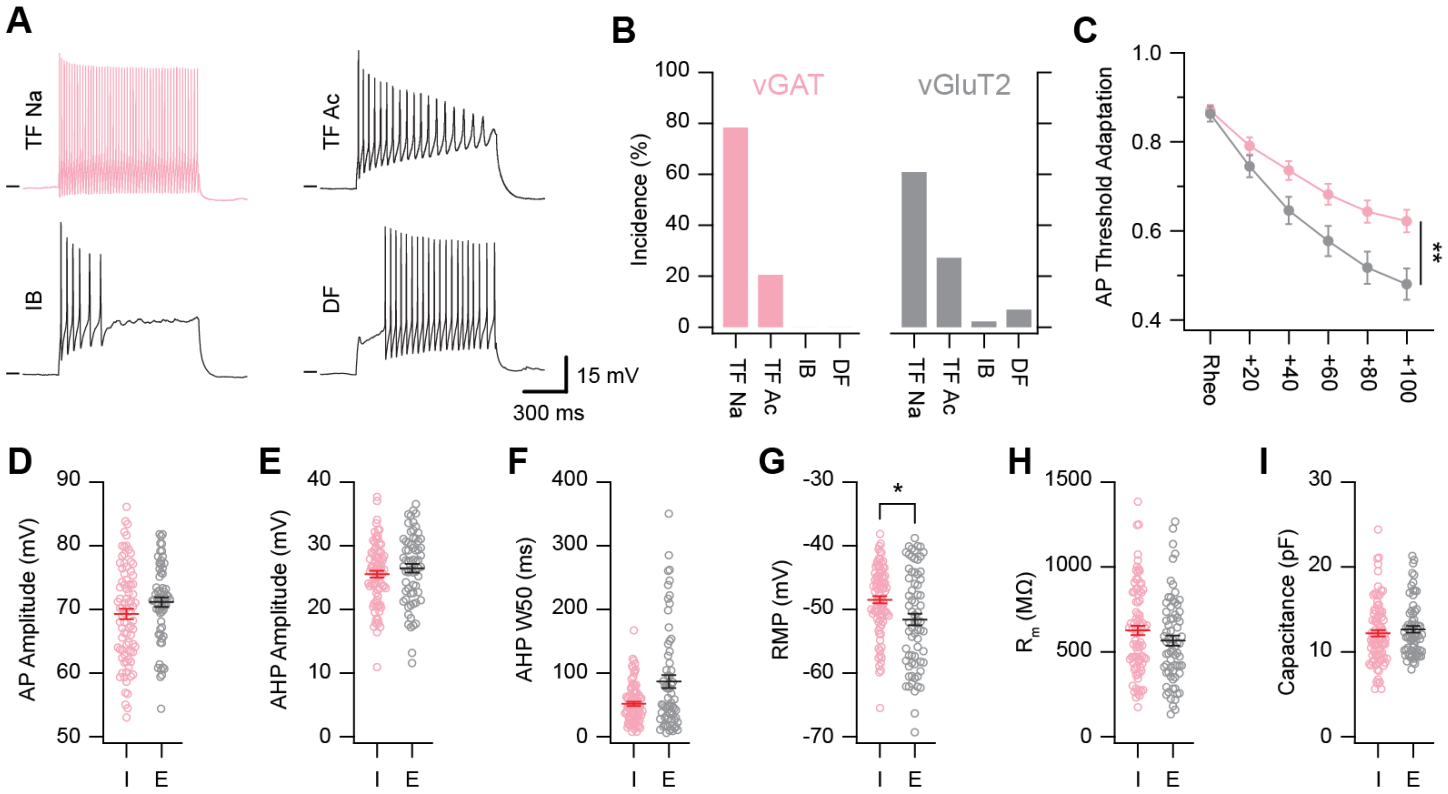

Figure S1 - related to Figure 2. **Electrophysiological characterization of deep dorsal horn inhibitory and excitatory neurons**. **A)** Representative traces of the four discharge patterns observed within the deep dorsal horn: Tonic firing non-accommodating (TF_{Na}), TF accommodating (TF_{Ac}), Initial bursting (IB), and Delayed firing (DF). **B)** Incidence of each discharge pattern in inhibitory (vGAT$^+$, pink) and excitatory (vGluT2$^+$, gray) neurons. **C)** Inhibitory neurons show less AP threshold adaptation. Two-way ANOVA, **p = 0052 **D)** AP amplitude. **E-F)** Threshold Afterhyperpolarization (AHP) analysis; **E)** AHP amplitude, and **F)** AHP half width. **G-I)** Passive membrane properties; **G)** Resting membrane potential (RMP), Mann Whitney test; *p = 0.0102 **H)** Membrane resistance (Rm), and **I)** Capacitance. Graphs show average +S.E.M. Red and black denote inhibitory and excitatory DDH INs, respectively.

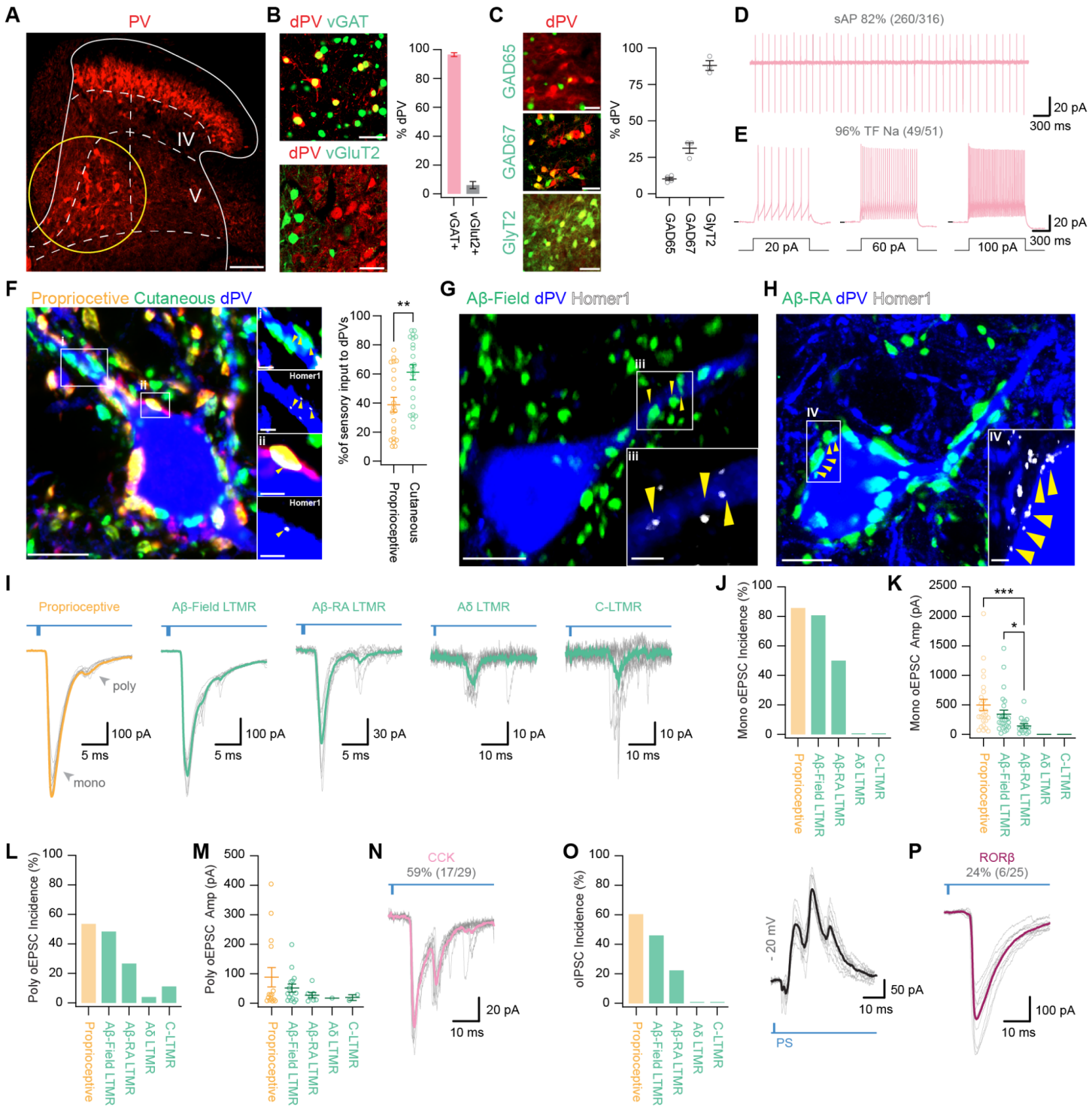

Figure 3. Inhibitory dPVs process convergent proprioceptive and cutaneous sensory inputs. A) Transverse, lumbar section of PV^{TdTomato} BAC transgenic shows the presence of PV expressing interneurons in the deep dorsal horn (dPVs, in yellow circle). Scale bar: 100 µm. **B)** dPVs are inhibitory neurons. Representative images (left) and quantification (right) of dPVs (red) that coexpress the inhibitory marker vGAT (green, top left) and excitatory marker vGluT2+ (green, top left). Scale bar: 40 µm. **C)** dPVs are predominantly Glycinergic. Representative images (left) and quantification (right) of percenta dPVs (red) that coexpress the inhibitory marker GAD65 (green, top left), GAD65 (green, middle left) and GlyT2 (green, bottom left). Scale bar: 40 µm. **D)** Cell-attached voltage clamp recording showing dPVs (82%) exhibit spontaneous AP discharge. **E)** Representative traces of dPV response to depolarizing current injection highlighting their TF discharge

pattern. **F)** Left- high resolution confocal image demonstrates a single dPV neuron surrounded and in contact with cutaneous (green) and proprioceptive (yellow) puncta. Scale bar: 10µm. i,ii) cutaneous (i) and proprioceptive (ii) puncta that are in contact with dPV soma and dendrite are shown to be in apposition to the postsynaptic marker Homer1 (yellow arrows). Scale bars: 2µm. Right- quantification of percent cutaneous (green) and proprioceptive (yellow) input to dPVs. Cutaneous input shows higher innervation of dPVs. Mann-Whitney test, *p < 0.05. **G-H)** High resolution confocal images show that dPVs are directly contacted by Aβ-field (G) and Aβ-RA (H) LTMRs. Scale bars: 10 µm. iii,iv) puncta are shown to be in apposition to Homer1 (yellow arrows). Scale bars: 2µm. **I)** Representative traces from dPVs showing 10 consecutive sweeps (gray) with average overlaid of oEPSCs (bold color) following activation of proprioceptors, Aβ-Field LTMRs, Aβ-RA LTMRs, Aδ-LTMRs, and C-LTMRs. **J-M)** Grouped data of monosynaptic oEPSC incidence (J); monosynaptic oEPSC amplitude (K); polysynaptic oEPSC incidence (L); and polysynaptic oEPSC amplitude (M). **N)** Representative trace from dPV showing 10 consecutive sweeps (gray) with average overlaid of oEPSCs (bold pink) following activation of CCK+INs. **O)** Grouped data showing oIPSC incidence (left) and representative oIPSC recorded at -20 mV (right). **P)** Representative trace from dPV showing 10 consecutive sweeps (gray) with average overlaid of oIPSC (bold black) following activation of RORβ+INs. Graphs show average +S.E.M. For further details on genetic crosses and statistical tests see Methods.

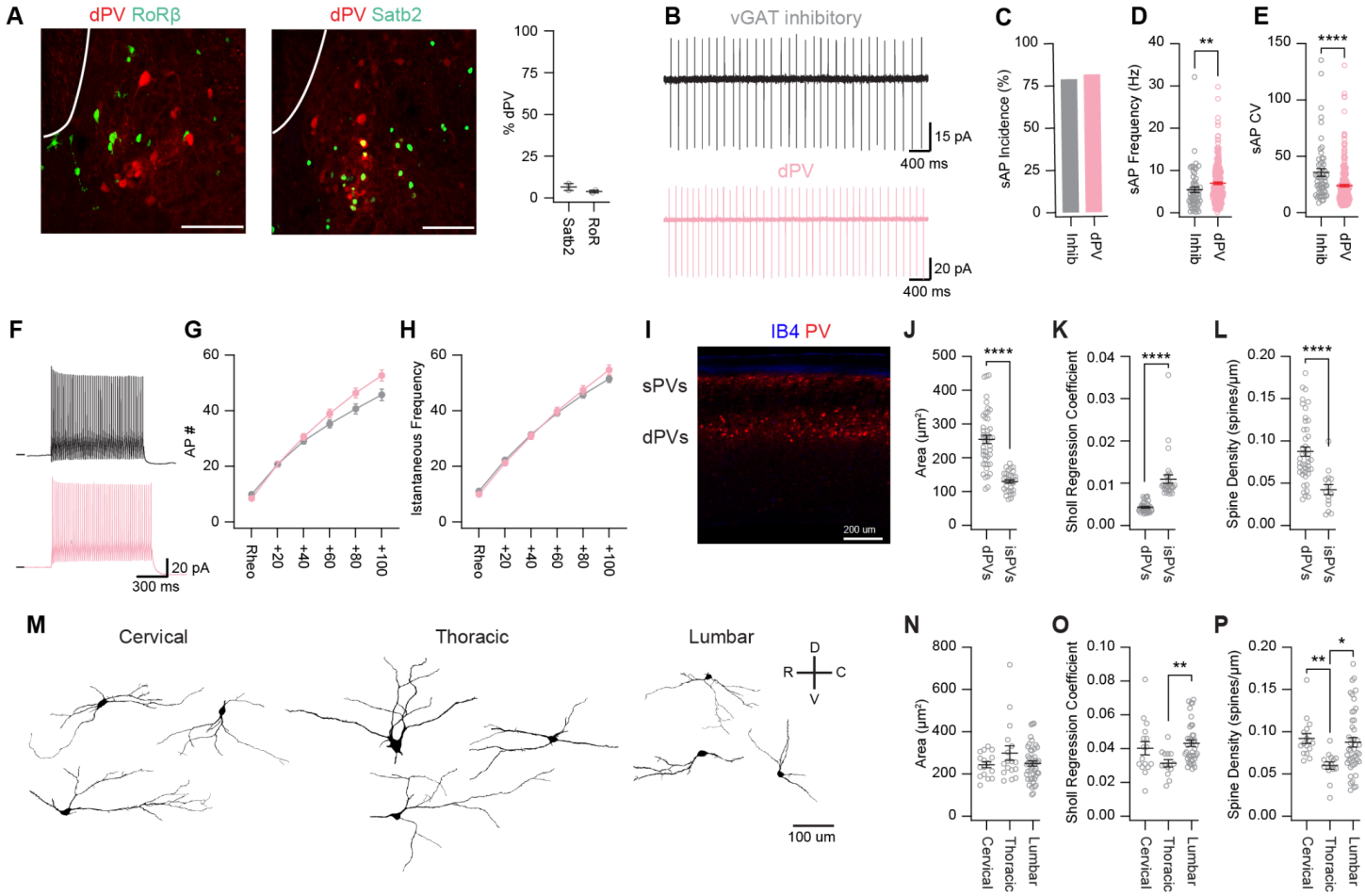

Figure S2- related to Figure 3. Previously uncharacterized, dPVs electrophysiology and morphology suggest a role in input integration. A) Left, middle- representative confocal images showing dPVs (red) and RoRβ (green, left, intersection: Rorb^{FlpO};*Rosa*$^{LSL\text{-}Tomato}$, stained with Guinea-pig-PV) or Satb2 (green, middle,

intersection: *Satb2*^{Cre};*Tau*$^{LSL\text{-}LacZ}$;PV^{TdTomato}**).** Scale bar: 100 µm. Right- quantification of percent dPVs expressing SatB2 or RoRβ shows dPVs are largely a distinct population. Analysis was performed using 6 images from 2 Rorb^{FlpO};*R26*$^{LSL\text{-}Tomato}$ mice; and 12 images from 2 *Satb2*^{CreER};*R26*$^{LSL\text{-}TdTomato}$ (stained with Guinea-pig-PV) mice. **B)** Representative cell-attached voltage clamp recording showing spontaneous action potential discharge (sAP) of DDH inhibitory neuron (gray, recorded using *vGAT*^{Cre};*R26*$^{LSL\text{-}Tomato(Ai14)}$) and dPV (red, recorded using PV^{TdTomato}). **C)** sAP incidence, **D)** frequency; Mann-Whitney test, **p = 0.0033, **E)** and coefficient of variation in inhibitory (gray) and dPV (red) neurons; Mann-Whitney test, ****p < 0.0001. **F-H)** dPVs and inhibitory neurons discharge a similar number and frequency of APs in response to current injection. **I)** Sagittal section from PV^{TdTomato} shows superficial PVs (sPVs) and dPVs. These sections were used for z-stack confocal imaging and neuronal reconstructions. inhibitory sPVs (isPVs) were targeted using the cross PV^{FlpO};vGAT^{iresCre}; R26$^{LSL\text{-}FSF\text{-}TdTom(Ai65)}$. Scale bar: 200 µm. **J)** Soma size. dPVs vs isPVs, Unpaired T-test, ****p < 0.0001. **K)** Sholl regression coefficient. dPVs vs isPVs, Mann Whitney test, ****p < 0.0001. **L)** Spine density dPVs vs isPVs, Mann Whitney test, ****p < 0.0001. **M)** Representative reconstructions of dPVs at cervical, thoracic, and lumbar segments. **N)** Soma size. **O)** Sholl regression coefficient, Krusal Wallis test with Dunn's correction for multiple comparisons, lumbar dPVs vs thoracic dPVs, ** p = 0.0073). **P)** Spine density, Krusal Wallis test, cervical dPVs vs thoracic dPVs, ** p = 0.0012; lumbar dPVs vs thoracic dPVs, * p = 0.0105) between cervical, thoracic and lumbar dPVs. Graphs show average +S.E.M.

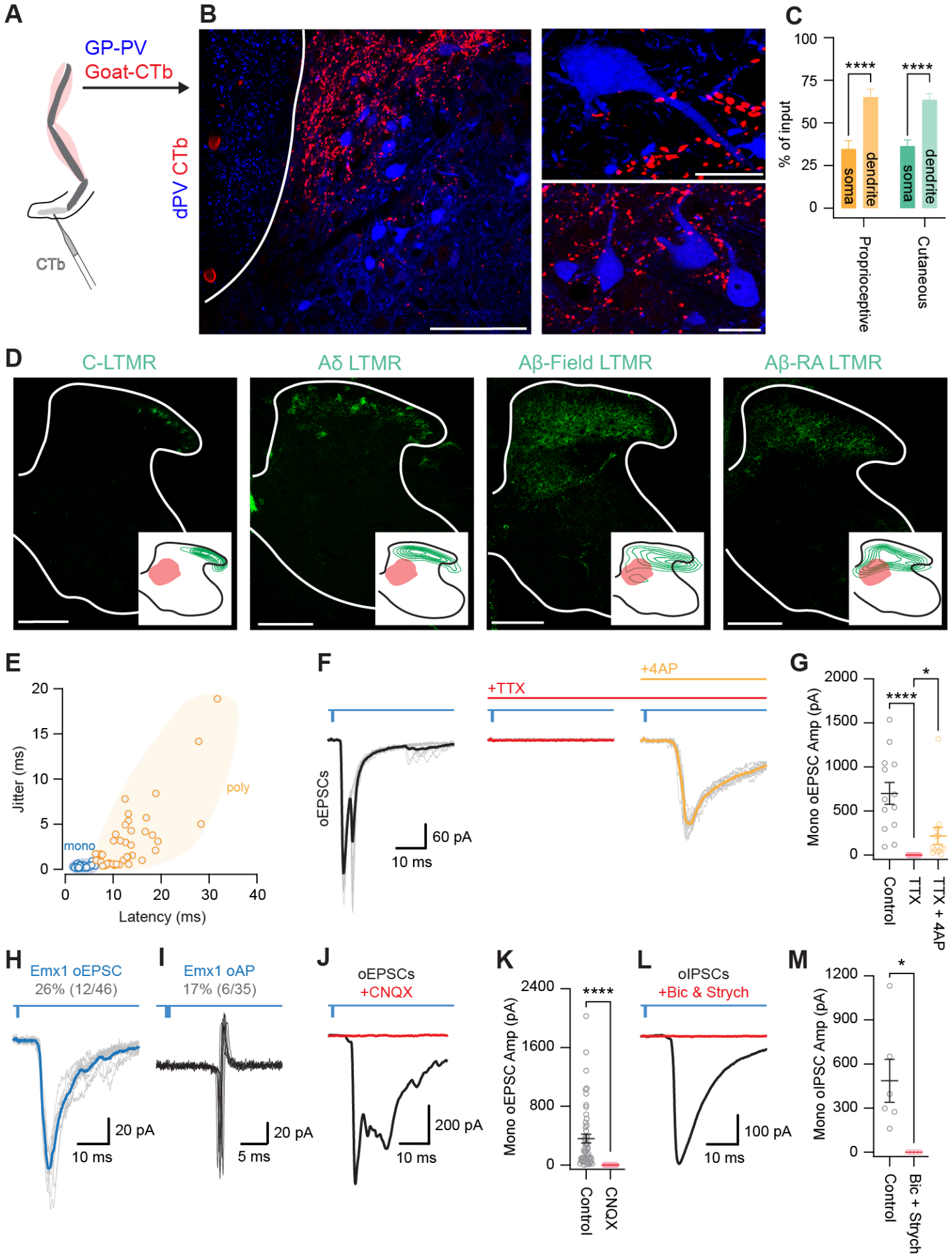
A
GP-PV
Goat-CTb
CTb
B
dPV CTb
C
% of input
100
75
50
25
0
****
****
soma
dendrite
soma
dendrite
Proprioceptive
Cutaneous
D
C-LTMR
Aδ LTMR
Aβ-Field LTMR
Aβ-RA LTMR
E
Jitter (ms)
Latency (ms)
mono
poly
F
oEPSCs
60 pA
10 ms
+TTX
+4AP
G
Mono oEPSC Amp (pA)
****
*
Control
TTX
TTX + 4AP
H
Emx1 oEPSC
26% (12/46)
20 pA
10 ms
I
Emx1 oAP
17% (6/35)
20 pA
5 ms
J
oEPSCs
+CNQX
200 pA
10 ms
K
Mono oEPSC Amp (pA)
****
Control
CNQX
L
oIPSCs
+Bic & Strych
100 pA
10 ms
M
Mono oIPSC Amp (pA)
*
Control
Bic + Strych

Figure S3- related to figure3. dPVs integrate diverse inputs through direct paw sensory afferents, local interneurons and cortical efferents. A) Experimental diagram to label paw input to dPVs. CTb was injected to the ventral paw of a WT animal to label paw sensory input. and tissue was immunostained with the primary antibodies Goat-CTb (red), and Guinea pig -PV (blue) and appropriate secondary antibodies. **B)** Low (left, scale bar: 100 µm) and high (right, scale bar: 20 µm) resolution images show that CTb labeled-paw afferents contact dPVs. **C)** Percent proprioceptive and cutaneous input on dPVs' soma and dendrites. For analysis, 21 neurons from 2 *PV*^{2aCreER}*;Advillin*^{FlpO}*;Rosa*$^{LSL\text{-}FSF\text{-}Tomato}$*/Rosa*$^{FSF\text{-}SynGFP}$ (2 mg tamoxifen treatment at P21-P23) mice were used. Proprioceptive input higher onto dendrites vs somas, Mann Withney test with Holm- Sidak correction for multiple comparisons,****$p < 0.0001$. cutaneous input higher onto dendrites vs somas, Mann Withney test with Holm- Sidak correction for multiple comparisons, ****$p < 0.0001$. **D)** Left to right- representative confocal (top) and contour density plots (inset) showing the termination pattern of axon terminals of C-LTMRs (TH^{2aCreER};Advillin^{FlpO};R26$^{FSF\text{-}LSL\text{-}SynaptophysinGFP}$, 2 mg tamoxifen treatment at P21-P23) , Aδ-LTMRs (TrKB^{CreER};R26$^{LSL\text{-}SynaptophysinTomato}$, 2 mg tamoxifen treatment at P21), Aβ-Field LTMRs (PTGFR^{CreER};R26$^{LSL\text{-}SynaptophysinTomato}$, 2 mg tamoxifen treatment at P21-P22), and Aβ-RA LTMRs (Ret^{CreER};R26$^{LSL\text{-}SynaptophysinTomato}$, 2 mg tamoxifen treatment at E10-E11) relative to the location of dPVs (PV^{FlpO};Lbx1^{Cre};R26$^{LSL\text{-}FSF\text{-}TdTomato}$) in the lumbar spinal cord. Scale bars: 200 µm. 3 images of each genotype were used to generate each contour plot. **E)** Quantification of light induced currents with latency and jitter used to determine mono- or poly-synaptic transmission. **F)** Representative traces (gray) with average overlaid of oEPSCs (bold) with subsequent addition of TTX (red) and 4-AP (orange). Grouped data **G)** summarize the effect of pharmacology on monosynaptic oEPSC. Addition of 4-AP in the presence of TTX isolates monosynaptic oEPSCs. Control *vs*. TTX, ****$p < 0.0001$ and TTX *vs*. 4AP, *$p = 0.0181$; Friedmans test with Dunn's multiple comparisons. **H)** Representative traces (gray) from dPV showing 10 consecutive sweeps with average overlaid of oEPSCs (bold) following activation of Emx1^{+} neurons. **I)** These inputs occasionally (17%) evoked AP discharge. **J)** Representative oEPSC trace showing the impact bath applied CNQX. Group data **K)** shows oEPSCs are completely blocked following addition of CNQX; ****$p < 0.0001$, Mann-Whitney test. **L)** Representative oIPSC trace showing the impact bath applied Bicuculline and Strychnine. Group data **M)** shows oIPSCs are completely blocked following addition of bicuculline and strychnine; *$p = 0.0488$, paired t-test. Graphs show average +S.E.M.

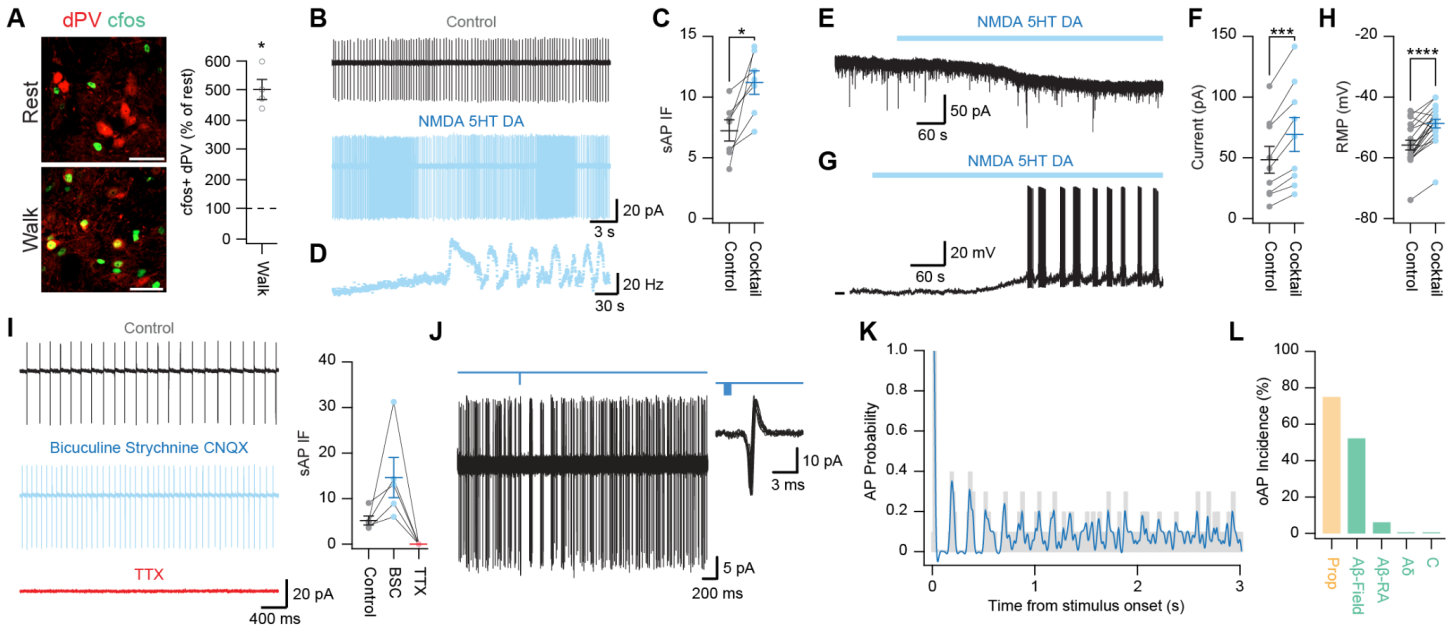

Figure 4. The timing of dPVs activity, recruited during locomotion, is reset by sensory input. A) Left- representative images of c-fos expression (green) in dPVs (red) following rest (top) and walk (bottom). Scale bar: 40 µm. Right- quantification of cfos+dPVs following walk, as percentage of rest. **B)** Representative traces of dPV responses in cell-attached voltage clamp before and after bath application of a cocktail containing NMDA, 5HT, and DA. **C)** Group data shows sAP instantaneous frequency (sAP IF) is increased following cocktail application. **D)** Plot showing instantaneous sAP frequency following cocktail application. dPVs occasionally (3/7) respond with rhythmic AP bursting. **E-F)** Representative traces (E) and grouped data (F) of dPV responses in whole-cell voltage-clamp before and after cocktail application shows increased inward current. **G-H)** Representative traces (G) and grouped data (H) of dPV responses in whole-cell current-clamp before and after cocktail application shows increased resting membrane potential (RMP). **(I)** Left- cell-attached voltage clamp recording showing dPV sAP under control conditions (black), following bath-application of channel blockers (Bicuculline, Strychnine and CNQX, blue), and TTX (red). Right- grouped data showing the effect of blocking synaptic transmission of sAP frequency. **J)** Representative traces showing 10 consecutive sweeps of sAPs during sensory afferent stimulation (blue bar). Inset shows optically evoked AP. **K)** Histogram of AP probability with an overlaid piecewise polynomial computed from p = 0.9 in MATLAB. **L)** Grouped data showing oAP incidence following photostimulation of sensory afferent populations. Graphs show average +S.E.M. Statistical analysis was done using Mann Whitney test (A), paired t-test (D,F), or Wilcoxon matched-pairs signed rank test (I), with *p<0.05, **p<0.005, ****p < 0.0005 and ****p < 0.0001. For further details on genetic crosses and statistical tests see Methods.

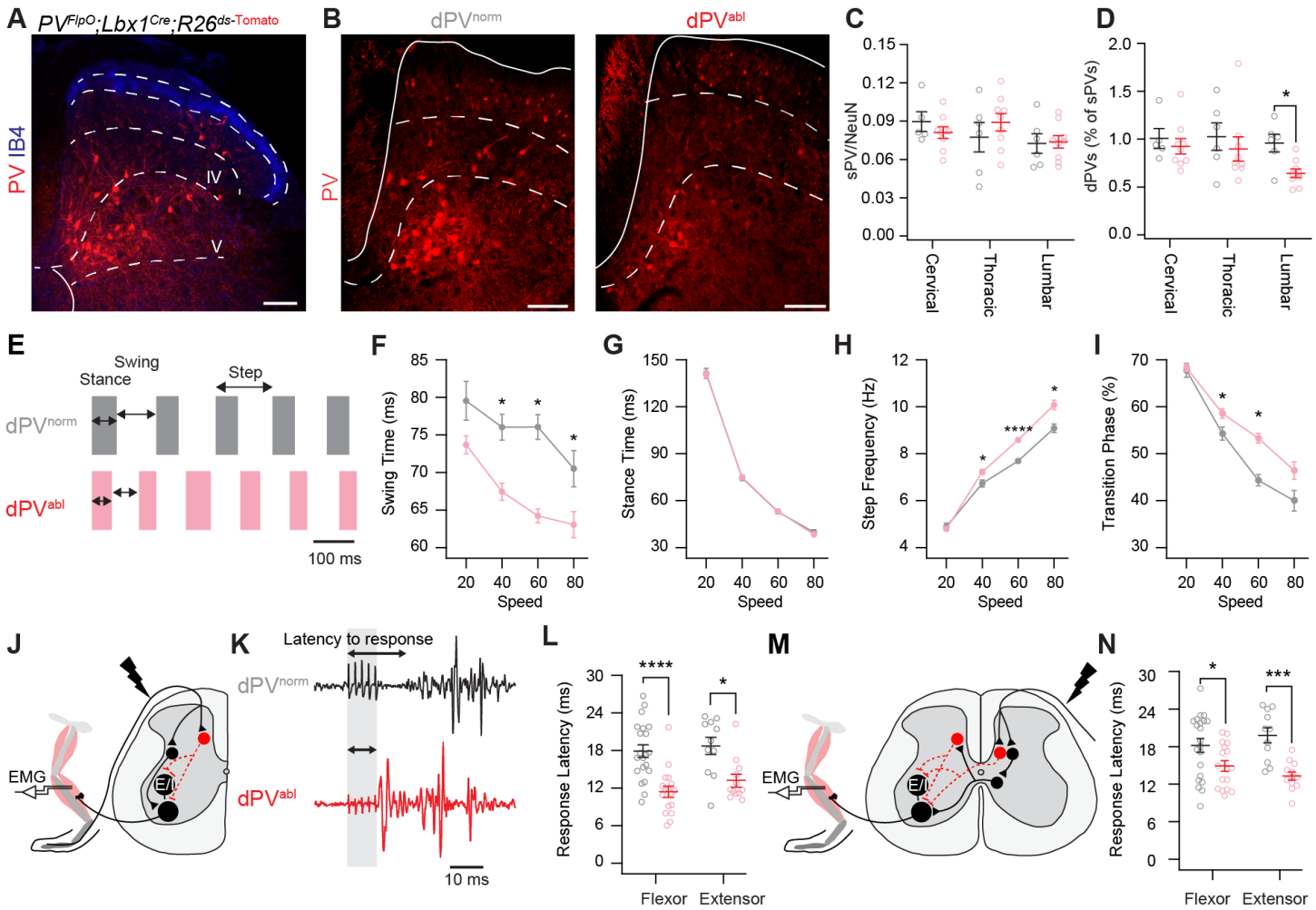

Figure 5. Ablation of dPVs alters the timing of sensory evoked muscle activity to modulate stride dynamics. A) Representative lumbar section from *PV*^{FlpO};Lbx1^{Cre};R26$^{LSL\text{-}FSF\text{-}TdTomato}$ shows that the intersection targets deep dorsal horn PV INs (dPVs) mainly located in lamina IV-V. Scale bar: 100 µm. **B)** Transverse sections demonstrating PV neurons (red) in the L4 spinal cord of dPV^{norm} (left) and dPV^{abl} (right). Scale bar: 100 µm. **C)** Quantification of superficial PVs (sPVs), normalized to NeuN in laminae I-III, throughout the cervical, thoracic and lumbar segments. **D)** Quantification of dPVs, normalized to sPVs, throughout the cervical, thoracic and lumbar segments. dPV^{abl} show a decrease in lumbar dPVs. **E)** Example stepping (left hindlimb, 60 cm/s) shows a shorter swing and increased step frequency in dPV^{abl}. **F-I)** Grouped data showing swing duration (F), stance duration (G), step frequency (H), and transition phase from stance to swing (I) at increasing speeds. **J)** Experimental setup designed to reveal the contribution of dPVs to flexor/extensor motor activity evoked by stimulation of an ipsilateral cutaneous (sural or saphenous) nerve. **K)** Example EMG response of the right knee flexor semitendinosus to stimulation of the right saphenous nerve in dPV^{norm} (top) and dPV^{abl} (bottom). **L)** Group data from experiment in F shows decreased response latency in ipsilateral flexors and extensors of dPV^{abl}. **M)** Experimental setup designed to reveal the contribution dPVs to flexor/extensor motor activity evoked by stimulation of a contralateral cutaneous (sural or saphenous) nerve. **N)** Group data from experiment in M shows decreased response latency in contralateral flexors and extensors of dPV^{abl}. Graphs show average +S.E.M. Black and red denote dPV^{norm} and dPV^{abl}, respectively. Statistical analysis was performed with Mann Whitney test (C,D,L), linear mixed effects regression model with mouse ID as a random effect (F,I), or unpaired t-test (N), with *p<0.05, **p<0.005, ****p < 0.0005 and ****p < 0.0001. For further details on genetic crosses and statistical tests see Methods.

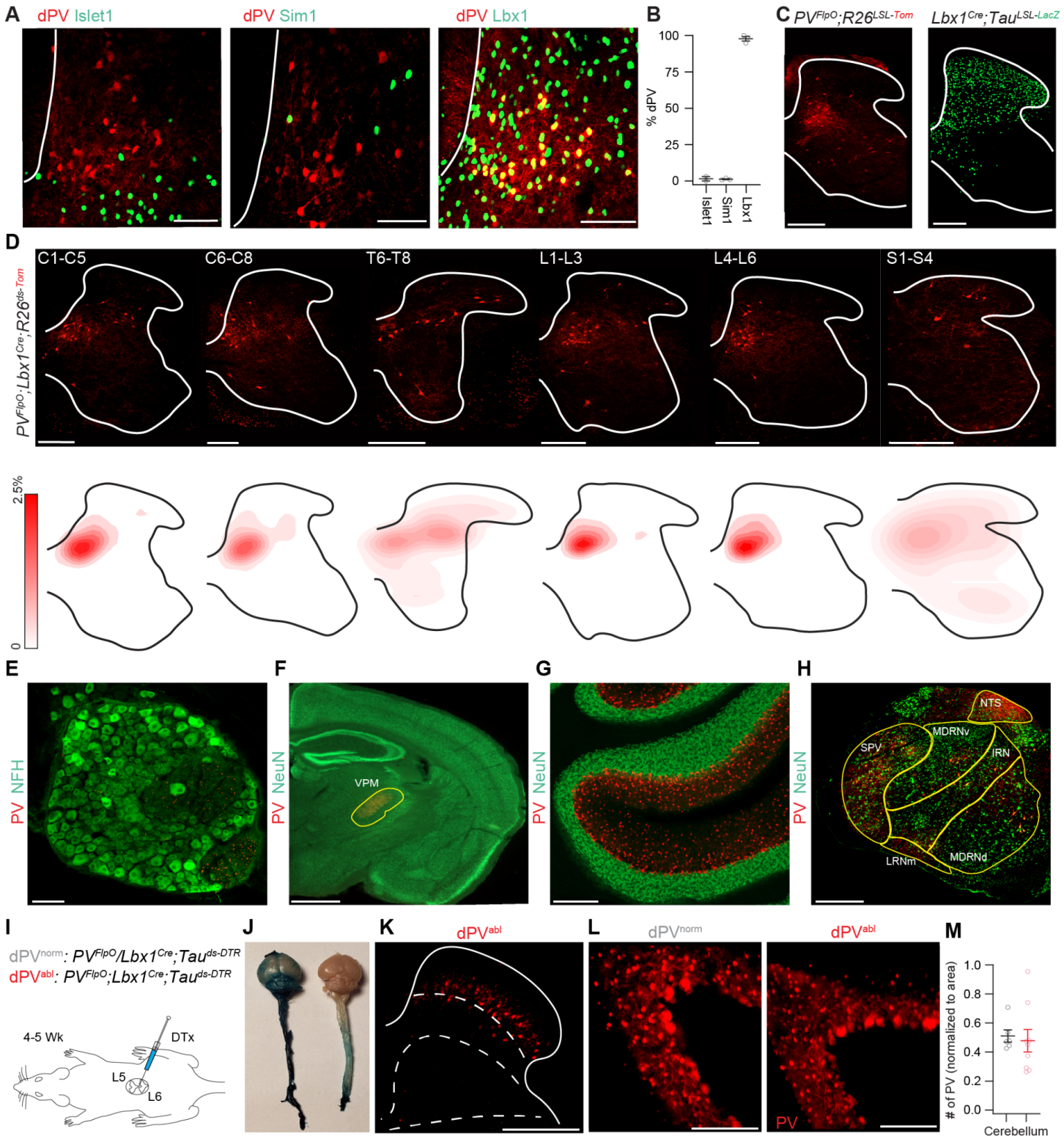

Figure S4- related to Figure 5. *PV^{FlpO};Lbx1^{Cre}* allows specific ablation of spinal cord dPVs. A) Representative images demonstrating colocalization of dPVs (red) with genetic lineages identified by transcription factor expression (green). Colocalization is shown with islet1 (left, *islet1^{Cre};Tau$^{LSL\text{-}LacZ}$*;PV^{TdTomato}), Sim1 (middle, *sim1^{Cre};Tau$^{LSL\text{-}LacZ}$*;PV^{TdTomato}), and Lbx1 (right, *Lbx1^{Cre};Tau$^{LSL\text{-}LacZ}$*;PV^{TdTomato}). Scale bar: 100 µm. **B)** Quantification of percent dPVs expressing islet1, Sim1, or Lbx1 shows that dPVs originate from the Lbx1 lineage. Analysis was performed using 15 images from 2 *islet1^{Cre};Tau$^{LSL\text{-}LacZ}$*;PV^{TdTomato}mice; 9 images from 3 *sim1^{Cre};Tau$^{LSL\text{-}LacZ}$*;PV^{TdTomato} mice; and 9 images from 3 *Lbx1^{Cre};Tau$^{LSL\text{-}LacZ}$*;PV^{TdTomato} mice. **C)** Representative

images of *PV*^{FlpO} (left, *PV*^{FlpO};*Rosa*$^{LSL\text{-}Tomato}$) and *Lbx1*^{Cre} (right, *Lbx1*^{Cre};*Tau*$^{LSL\text{-}LacZ}$) mouse lines show a bias toward deep and ventral, or superficial and deep populations, respectively. **D)** Tomato expression (top) and contour density plots (bottom) using the intersection *PV*^{FlpO};*Lbx1*^{Cre};*R26*$^{LSL\text{-}FSF\text{-}TdTomato}$ throughout the rostrocaudal axis of the spinal cord. Scale bar: 200 µm. Contour plots were generated using 10-15 images (for each spinal cord level) from 2 *PV*^{FlpO};*Lbx1*^{Cre};*R26*$^{LSL\text{-}FSF\text{-}TdTomato}$ mice. Increased red intensity indicates higher density (in percentage). **E)** Representative DRG section shows that DRGs are not targeted by the intersection. Scale bar: 100 µm **F)** Representative coronal section of the brain shows no cell body expression. Red labeling in the ventral posteromedial nucleus (VPM) of the thalamus represents fibers that originate from outside the brain. Scale bar: 1000µm. **G)** Representative section of the cerebellum shows that the intersection targets the molecular layer. Scale bar: 200 µm. **H)** Transverse section of the hindbrain shows that the intersection targets hindbrain nuclei like the spinal nucleus of the trigeminal (SPV), nucleus of solitary tracts (NTS), and subdivisions of the reticular nucleus (RN) such as the ventral part of the medullary reticular nucleus (MDRNv), dorsal part of the medullary reticular nucleus (MDRNd), and the intermediate reticular nucleus (IRN). Scale bar: 500 µm. **I)** Strategy for dPVs ablation. *PV*^{FlpO};Lbx1^{Cre};*Tau*$^{LSL\text{-}FSF\text{-}DTR}$ and PV^{FlpO};Tau$^{LSL\text{-}FSF\text{-}DTR}$ or Lbx1^{Cre};Tau$^{LSL\text{-}FSF\text{-}DTR}$ were injected with 50 ng Diphtheria toxin (DTx), delivered intrathecally (I.T.) into the L5-L6 intervertebral space to generate animals with ablated dPVs (dPV^{abl}) and non-ablated dPVs (dPV^{norm}). **J)** Intrathecal injection (I.T.) of 20% fast green made in PBS (left) or hyperbaric solution (right) to a WT mouse, demonstrates that the latter restricts spread to the spinal cord. **K)** 10x confocal image showing lumbar spinal cord of a *PV*^{FlpO};*Lbx1*^{Cre};*Tau*$^{LSL\text{-}FSF\text{-}DTR}$ mouse following I.T. injection of 1µg DTx, a larger dose than used for behavior experiments (Figure 5, Figure 6). While more dPVs (red) are ablated (compared to Figure 5B), superficial PVs are intact, demonstrating the specificity of our ablation method. Scale bar: 200 µm. **L)** 20x images of cerebellum PV neurons (red) showing no obvious ablation in dPV^{norm} (left) and dPV^{abl} (right). Scale bar: 200 µm **M)** Quantification of PV neurons in the molecular layer of the cerebellum shows no significant difference between dPV^{norm} (24 images of 6 animals used) and dPV^{abl} (4 images of 10 animals used). Mann Whitney test, $p = 0.5287$. Graphs show average +S.E.M. Black and red denote dPV^{norm} and dPV^{abl}, respectively.

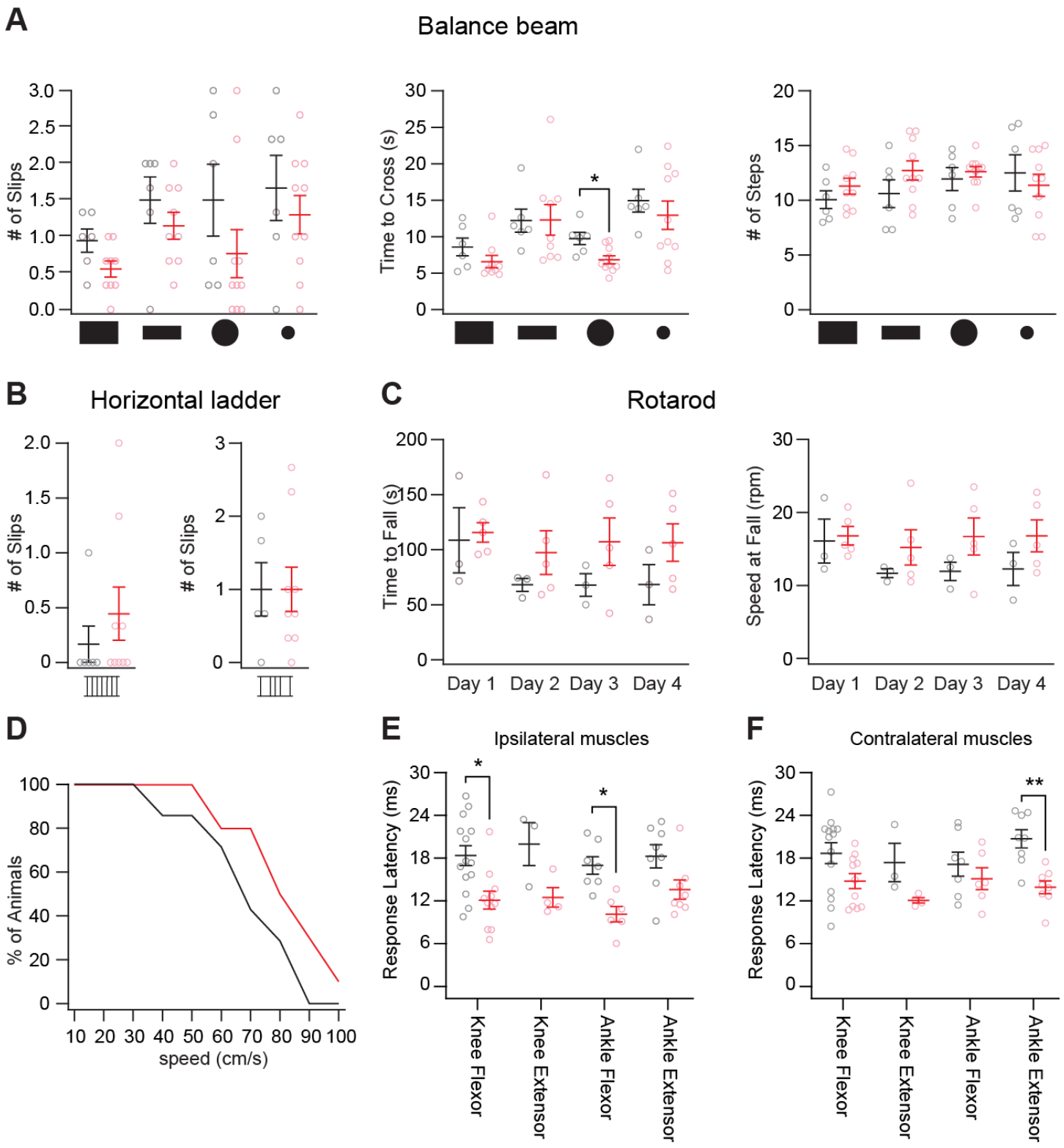
A
Balance beam
# of Slips
Time to Cross (s)
# of Steps
B
Horizontal ladder
# of Slips
# of Slips
C
Rotarod
Time to Fall (s)
Speed at Fall (rpm)
Day 1
Day 2
Day 3
Day 4
D
% of Animals
speed (cm/s)
E
Ipsilateral muscles
Response Latency (ms)
Knee Flexor
Knee Extensor
Ankle Flexor
Ankle Extensor
F
Contralateral muscles
Response Latency (ms)
Knee Flexor
Knee Extensor
Ankle Flexor
Ankle Extensor

Figure S5- related to figure 4. Ablation of dPVs does not alter corrective motor reflexes but may promote faster walking by shortening muscle response latency. A) Number of slips (left), time to cross the beam (middle) and number of steps (right) on rectangular 10 mm, rectangular 5 mm, circular 10 mm and circular 5 mm balance beams. Significant difference is shown for time to cross the 10 mm circular beam, Mann Withney test, *p = 0.043 **B)** Quantification of the number of slips on a horizontal ladder with rungs in a regular pattern (left) or irregular pattern (right). **C)** Quantification of time to fall and speed at fall from the rotarod for 4 consecutive days. **D)** Percentage of animals successfully walking at each speed (10-100 cm/s) shows dPVabl mice reach higher speeds. **E)** dPV^{abl} showed decreased response latency of semitendinosus (St, knee flexor), Mann Whitney test with Holm-Sidak correction, *p = 0.0152; and tibialis anterior (TA, ankle flexor) following stimulation of ipsilateral cutaneous nerves, Mann Whitney test with Holm-Sidak correction, *p = 0.0092. **F)** dPV^{abl} showed decreased response latency of gastrocnemius (Gs, ankle extensor) following stimulation of contralateral cutaneous nerves, Mann Whitney test with Holm-Sidak correction, **p = 0.0043. Graphs show average ±S.E.M. Black and red denote dPV^{norm} and dPV^{abl} , respectively.

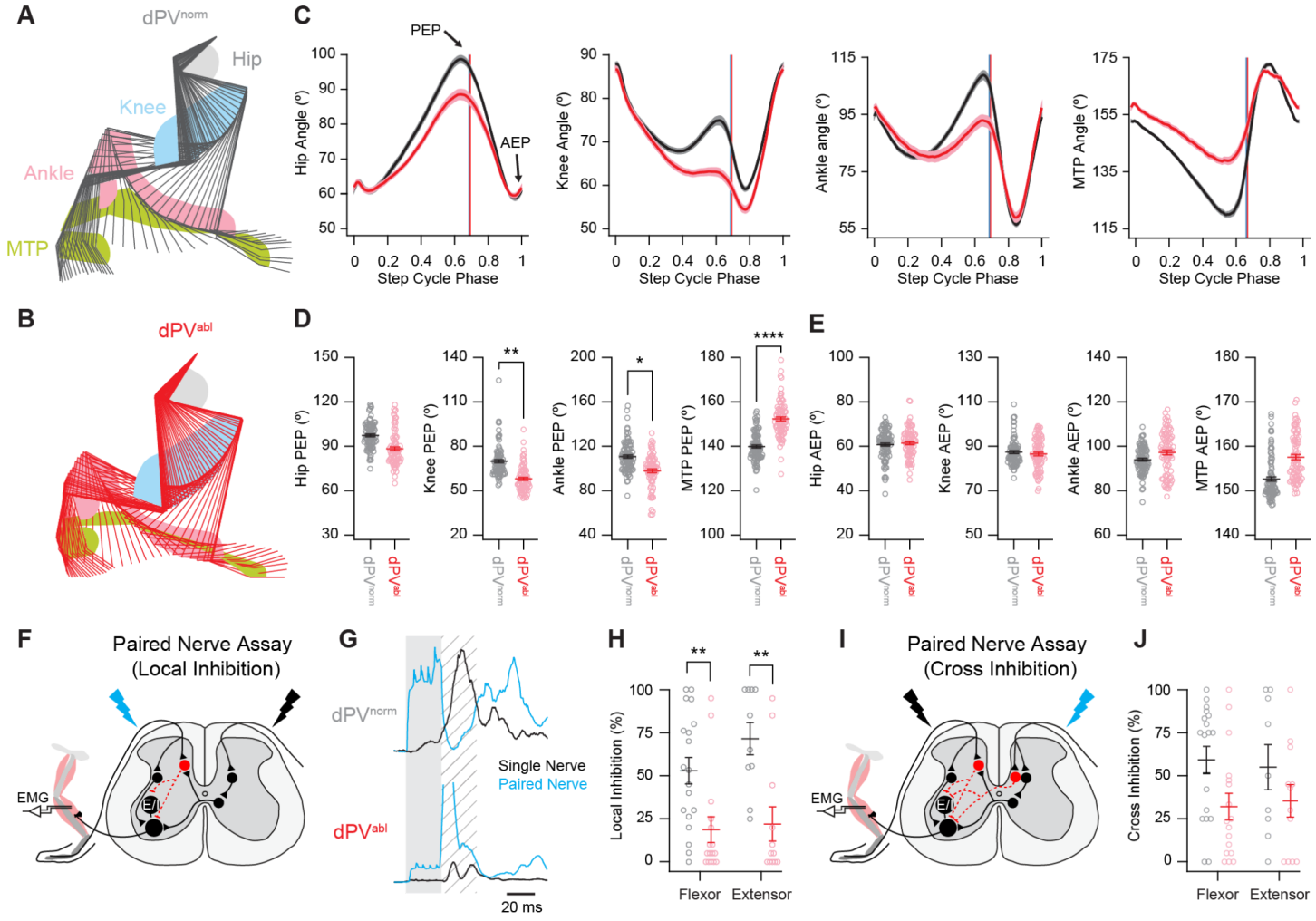

Figure 6. Reduced sensory-evoked inhibition following dPV ablation alters limb kinematics. A-B) Example stick diagrams of a step performed by dPV^{norm} (A) and dPV^{abl} (B) suggest changed joint angles during surface contact (stance). **C)** Estimation of hip, knee, ankle and MTP joint angles during the normalized step cycle (0 is the beginning of stance and 1is the end of swing). Arrows denote cycle phase where animals were in the posterior extreme position (PEP), and anterior extreme position (AEP). Vertical lines denote transition

from stance to swing. **D-E)** Hip, Knee, Ankle and MTP angles at PEP (D) and AEP (E) show that dPV ablation alters joint angles during the transition from stance to swing (PEP). **F)** Experimental setup of paired nerves assay designed to reveal if dPVs mediate sensory-evoked local inhibition. **G)** Response to paired nerves stimulation (cyan) overlaid on the expected response (black) to the contralateral nerve alone, shows an ipsilateral nerve- mediated inhibitory component in dPV^{norm} (top), which is absent in dPV^{abl} (bottom) **H)** Grouped data showing percent sensory evoked- local inhibition (the percentage of trials where inhibition was detected) in hindlimb flexors and extensors. **I)** Experimental setup of paired nerves assay designed to reveal if dPVs mediate sensory-evoked contralateral inhibition. **J)** Grouped data showing percent sensory evoked-contralateral inhibition in hindlimb flexors and extensors. Graphs show average +S.E.M. Black and red denote dPV^{norm} and dPV^{abl}, respectively. Statistical analysis was performed with a linear mixed effects regression model with mouse ID as a random effect (D,E) or Mann Whitney (H,J), with *p<0.05, **p<0.005, ****p < 0.0005 and ****p < 0.0001. For further details on genetic crosses and statistical tests see Methods.

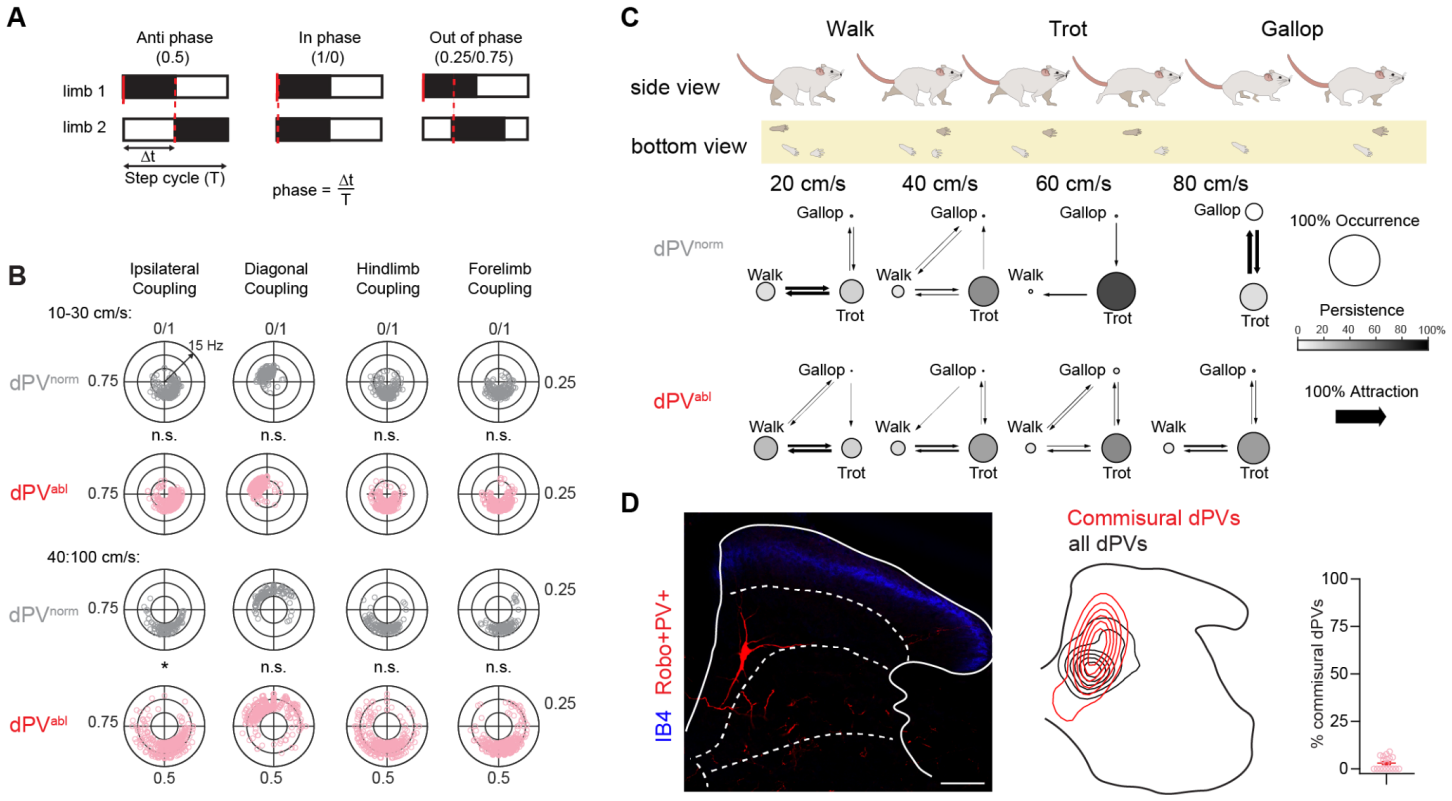

Figure S6- related to figure 6. Ablation of dPVs alters ipsilateral limb coupling and gait transition, as expected from non midline crossing interneurons. A) Diagram depicting phase coupling calculation. Δt, the time between the initial contact of a limb (limb 2) and a reference limb (limb 1), is divided by the duration of the step cycle (T). Step cycle duration is calculated for the reference limb from initial contact (beginning of stance) to lift-off (end of swing). Phase values of 0.5 (±0.25), 1/0(±0.25), and 0.25/0.75 (±0.25) indicate that limbs are in anti-phase, in-phase or out-of-phase, respectively. **B)** Comparison of phase-frequency plot of dPV^{norm} and dPV^{abl} at 10-30 cm/s (top) and 40-100 cm/s (bottom), for (from left to right) ipsilateral coupling, diagonal coupling, hindlimb coupling and forelimb coupling. **C)** Top- diagram depicting side view and bottom view of walk, trot, and gallop gaits. Bottom- gait transitions at 20, 40, 60 and, 80 cm/s of dPV^{norm} (top) and dPV^{abl} (bottom). Circle size, circle color and arrow width represent gait occurrence, persistence, and attractiveness (see methods). **D)** A small percentage of dPVs are commissural interneurons (CINs). Left- representative

confocal image from the intersection *PV*^{FlpO};*Robo3*^{CreER};*R26*$^{LSL\text{-}FSF\text{-}Tomato\ (Ai65)}$ (2 mg/kg tamoxifen at E10.5-E12.5) used to target commissural dPVs (red). Middle- contour density plot showing the distribution of commissural dPVs (red) relative to all dPVs (black). commissural dPVs spread throughout the region of dPVs. Contour map was generated using 18 images from a Robo3^{FlpO};PV^{Cre};*R26*$^{LSL\text{-}FSF\text{-}Tomato\ (Ai65)}$ animal and 13 images from 2 PV^{FlpO};*Lbx1*^{Cre};*R26*$^{LSL\text{-}FSF\text{-}Tomato\ (Ai65)}$. Right- quantification of the percentage of commissural dPVs relative to all dPVs show they represent 3.05% ± 0.79 percent. Analysis performed using 18 images from a Robo3^{FlpO};PV^{Cre};*R26*$^{LSL\text{-}FSF\text{-}Tomato\ (Ai65)}$.

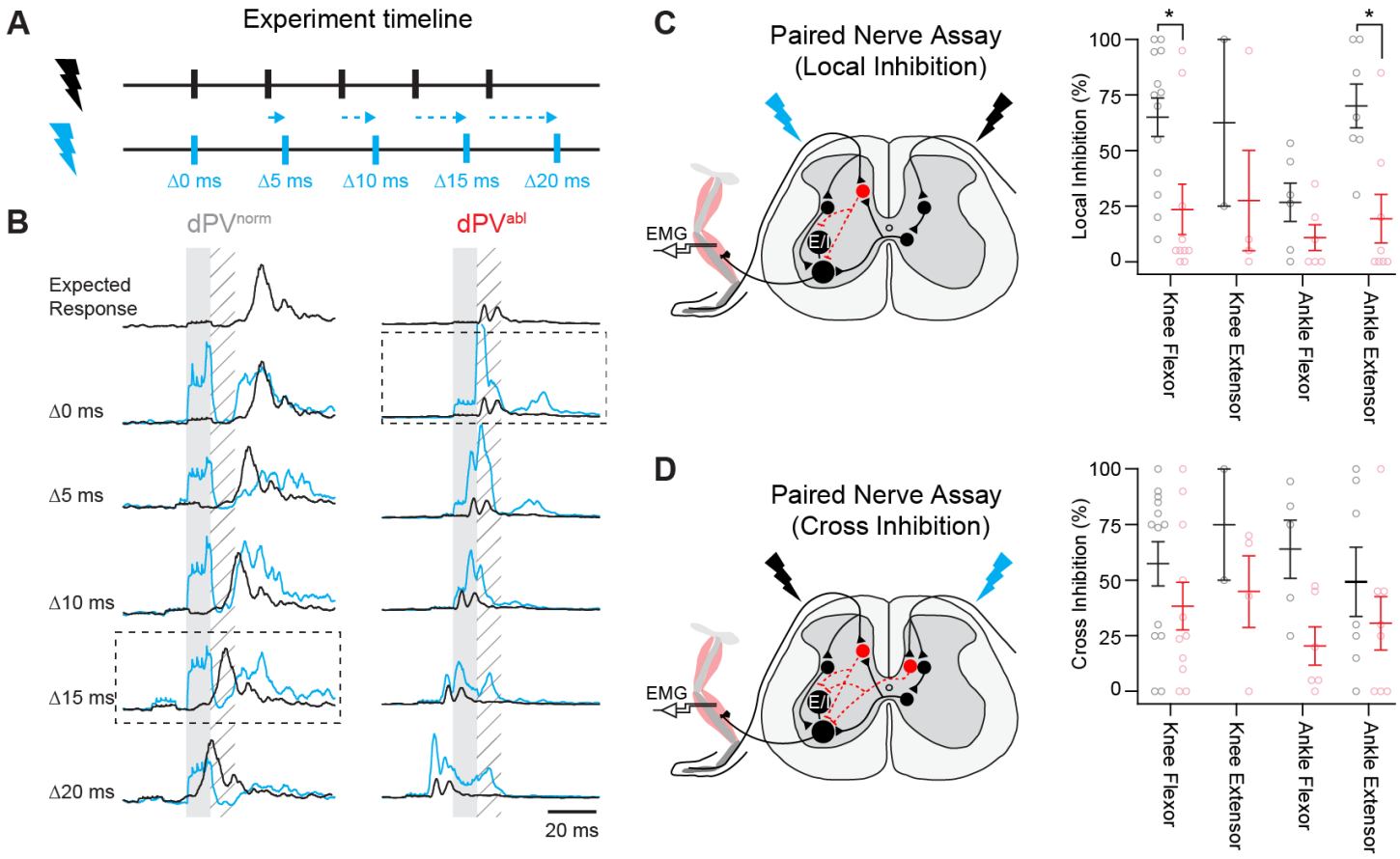

Figure S7- related to figure 6. Paired- nerves assay is used to reveal sensory mediated- dPV inhibition of motor output. A) Experiment timeline. First, stimulation of a single nerve is performed (black lightning) to calculate the "expected response". Next, both cutaneous nerves are stimulated at varying delays (cyan lightning). **B)** Example EMG responses recorded in the right gastrocnemius (Gs) of dPV^{norm} (left) and dPV^{abl} (right).Top row shows the "expected response" to stimulation of the left saphenous nerve (black), averaged over 20 trials. Rows 2-5 show responses to paired stimulation of the left saphenous nerve and right sural nerves (cyan), at delay of 0, 5, 10, 15, and 20 ms, respectively, overlaid on the expected response. Different delays are applied to account for differences in response latencies within muscles and within animals. The two responses are aligned using the initiation time of the stimulation (second stimulation for response to paired stimulation). For each animal, and each muscle a single delay is chosen for quantification of percent inhibition. Delay on which the peak of the expected response occurs 10-20 ms following the stimulation of the second nerve is chosen for analysis of percent inhibition (dotted boxes). 10-20 ms window was chosen as it was shown to be the approximate latency for cutaneous-motor response. **C)** Left- experimental diagram depicting paired nerves assay designed to reveal if dPVs mediate sensory-evoked local inhibition. Right- dPV^{abl} show a decrease in percent of local inhibition in semitendinosus (St, knee flexor), Mann Whitney test with Holm-Sidak correction, *p = 0.0239; and in gastrocnemius (Gs, ankle extensor), Mann Whitney test with Holm-Sidak correction, *p = 0.0239. **D)** Left- experimental diagram depicting paired nerves assay designed to reveal if

dPVs mediate sensory-evoked contralateral inhibition. Right- dPV^{abl} showed no change in contralateral percent inhibition.

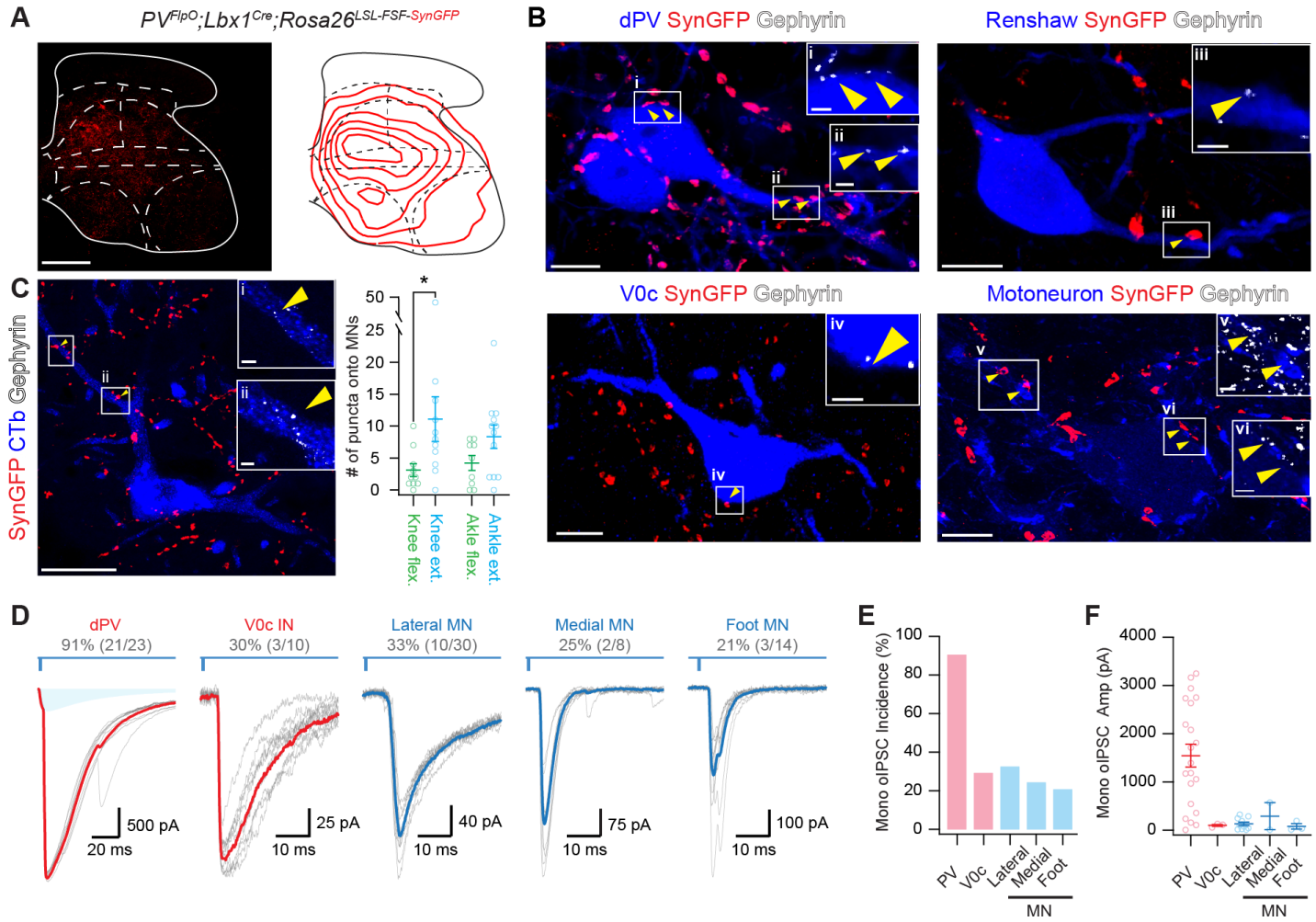

Figure 7. dPVs have diffuse postsynaptic targets throughout the deep dorsal and ventral horns. A) Representative image (left) and density map depicting distribution of dPVs axon terminals in the limb level lumbar cord of *PV^{FlpO}*;Lbx^{1Cre};*Rosa$^{LSL-FSF-SynGFP\ (FPSit)}$*. Scale bar: 200 µm. **B)** High resolution confocal images demonstrating direct contact between dPVs terminals (SynGFP, red) and deep dorsal horn and ventral horn interneurons (blue). dPVs are shown to contact other dPVs (top left), Renshaw cells (top right), V0c interneurons (bottom left) and motor neurons (MNs, bottom right). Scale bar: 10 µm. i,ii,iii,iv,v) dPVs' terminals are shown to be in apposition to the inhibitory postsynaptic marker Gephyrin (white, yellow arrows). Scale bar: 2 µm. **C)** Left- high resolution confocal image of CTb labeled vastus lateralis MN. Scale bar: 40 µm. i,ii) dPVs' terminals that are in contact with the MN, are shown to be in apposition to the inhibitory postsynaptic marker Gephyrin (white, yellow arrows). Scale bar: 2µm. Right- quantification of gephryin apposed dPV puncta onto flexor and extensor MNs show bias toward extensor MNs. Multiple Mann Whitney tests, knee flexor vs knee extensor *p<0.05. **D)** Representative traces showing 10 consecutive sweeps (gray) with average overlaid of oIPSC (bold color), recorded from dPV V0c interneurons, Lateral, Medial, and Foot motoneurons following dPV photostimulation. **E)** Grouped data of monosynaptic oEPSC incidence. **G)** Grouped data of monosynaptic oEPSC amplitude. Graphs show average +S.E.M. For further details on genetic crosses and statistical tests see Methods.

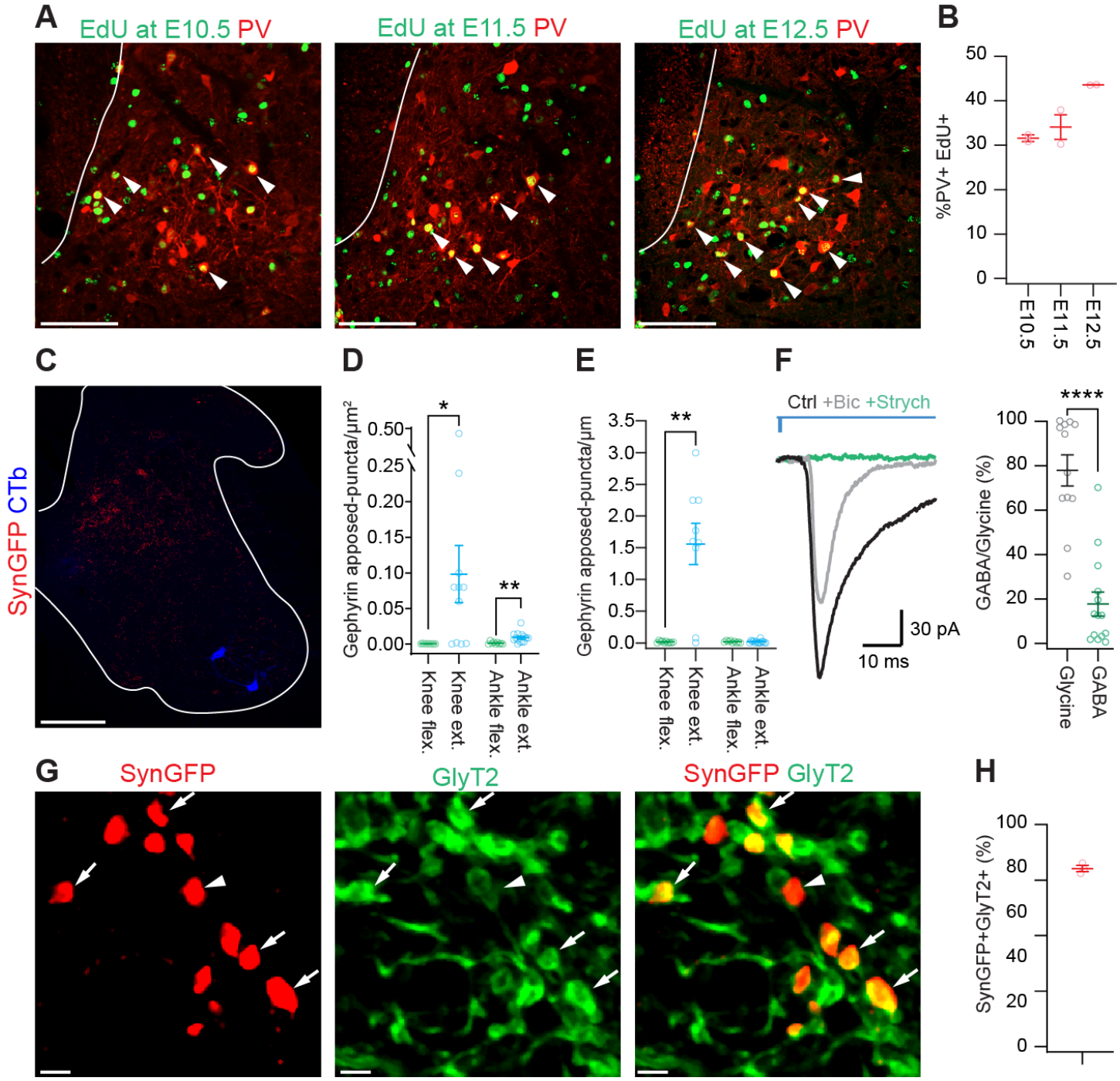

Figure S8- related to figure 7. dPVs neurogenesis is consistent with preferred inhibition of extensor motor neurons. A) Representative images of dPVs (red) from $PV^{TdTomato}$ mice injected with EdU (green) at E10.5 (left), E11.5 (middle) and E12.5 (right). Colocalization of dPVs with EdU (white arrows) on a specific day denote their neurogenesis. Scale bar: 100 µm. **B)** Quantification of EdU expressing-dPVs (using 5-7 images from 2 animals for each day) as percentage of total dPVs on each day. **C)** 10x confocal image taken from PV^{FlpO};$Lbx1^{Cre}$;$R26^{LSL\text{-}FSF\text{-}SynGFP}$ injected with Alexa fluor 555- conjugated CTb to the vastus lateralis (VL). CTb labeled- VL MNs (blue) are shown in the vicinity of dPVs' terminals (red). Scale bar: 200 µm. **D)** Quantification of Gephyrin apposed- dPVs puncta on motor neurons soma (normalized to soma area) shows preferred innervation of extensor MNs. Knee extensor vs knee flexor, Mann whitney test, with Holm-Sidak correction for

multiple comparisons, *p = 0.0093; Ankle extensor vs ankle flexor, Mann whitney test, with Holm-Sidak correction for multiple comparisons, *p = 0.0006 **E)** Quantification of Gephyrin apposed- dPVs puncta on motor neurons neurites (normalized to total neurite length) shows preferred innervation of extensor MNs. Knee extensor vs knee flexor, Mann whitney test, with Holm-Sidak correction for multiple comparisons, *p = 0.0012; Ankle extensor vs ankle flexor, Mann whitney test, with Holm-Sidak correction for multiple comparisons, p = 0.6871. **F)** Left- representative response of oIPSCs following application of bicuculline (gray) and strychnine (green). Right- grouped data showing the GABA/glycine contribution to oIPSCs. ****p < 0.0001, Mann Whitney test. **G)** 40x confocal images from $PV^{FlpO};Lbx1^{Cre};R26^{LSL\text{-}FSF\text{-}SynGFP}$ show dPVs' (red) and GlyT2+ (green, stained with Guinea Pig- GlyT2) terminals. White arrows show dPVs' terminals in colocalization with GlyT2; white arrowheads denote no colocalization. Scale bar: 2 µm. **H)** Quantification of percent dPV terminals that express GlyT2 relative to total dPV terminals, performed with 3, 40x, z-stacks images from a $PV^{FlpO};Lbx1^{Cre};R26^{LSL\text{-}FSF\text{-}SynGFP}$ animal (stained with Guinea Pig- GlyT2)